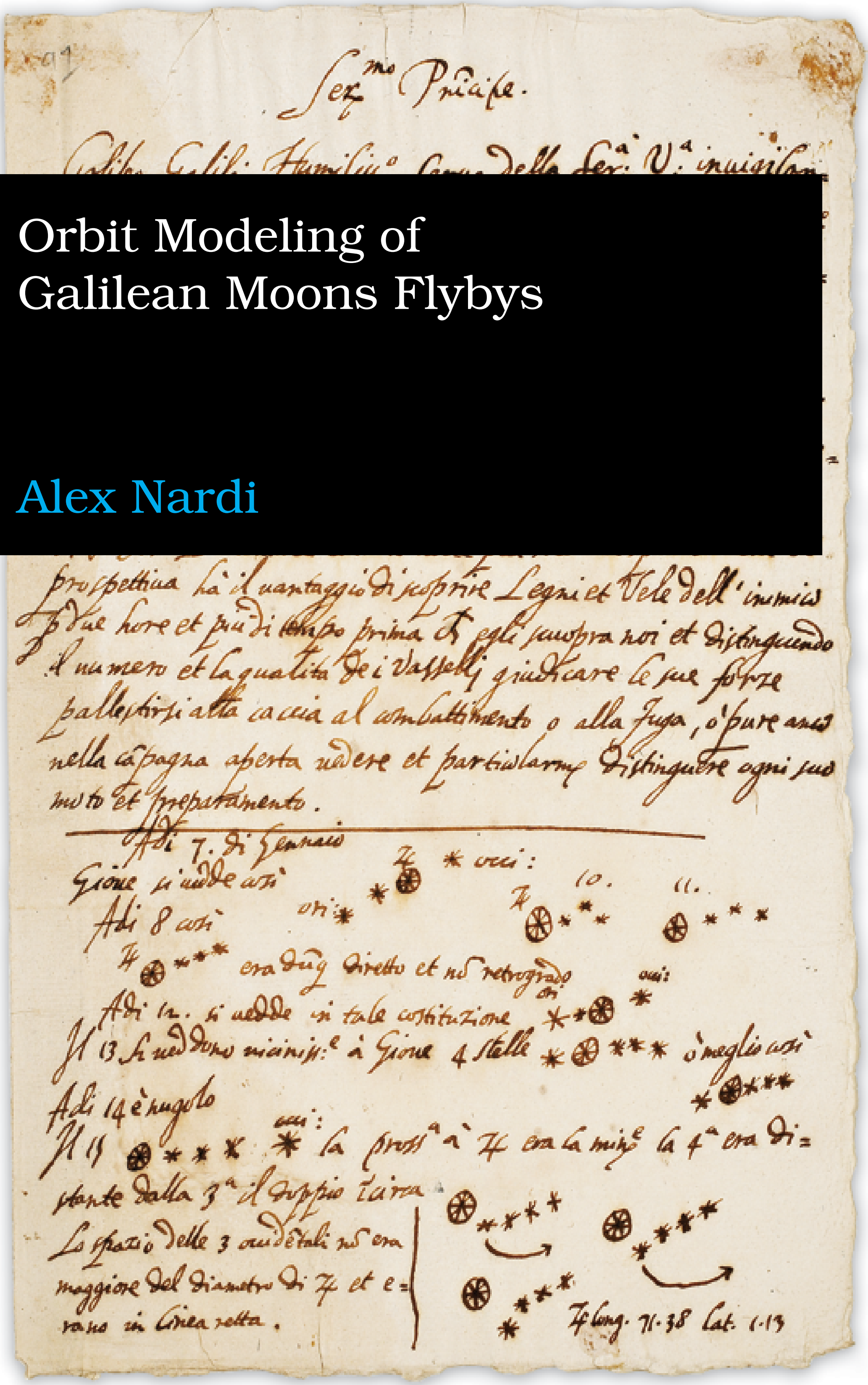

Orbit Modeling of Galilean Moons Flybys

Alex Nardi

Master of Science Thesis

Delft University of Technology

Faculty of Aerospace Engineering

Illustration front page: page 1 of Galilei [1610], in which the Italian scientist Galileo Galilei announced the discovery of four satellites of Jupiter: the Medicea Sidera, now known as Galilean moons.

Orbit Modeling of Galilean Moons Flybys

Master of Science Thesis

For the degree of Master of Science in Space Exploration at Delft University of Technology

Alex Nardi

June 29, 2017

Faculty of Aerospace Engineering · Delft University of Technology

The work in this thesis was supported by Astos Solutions GmbH. Their cooperation is hereby gratefully acknowledged.

“All truths are easy to understand once they are discovered. The point is to discover them.”

— *Galileo Galilei*

Abstract

This research aims at modeling the trajectory followed by the Galileo spacecraft during a variety of flybys about the Galilean moons. The chosen flybys have good Earth's elevation angles and either low or high closest-approach altitudes, so that the comparison of the two can give relevant insight into the accuracy of the corresponding trajectories. By propagating the state of the spacecraft during these flybys, optimizing the nominal initial state of the spacecraft (obtained through the SPICE program) and the spherical harmonics of the moons, and estimating new harmonics, the minimum root mean square error between the resulting trajectory and the Jet Propulsion Laboratory (JPL) ephemerides is found. The analysis of its components along the Local Orbital axes gives insight into the existing relation between them and the Earth's elevation and azimuth angles. In particular, a low-altitude flyby implies in general a higher error, but when two flybys have similar altitudes, then the Earth's elevation plays a relevant role and the flyby with the largest one is more likely to have a larger error too. The root mean square error of the fitted trajectories can vary from 15 cm to 7 m, so always less than the 9 m declared by NASA [2004] as the maximum error of the moons ephemerides. Furthermore, the flybys about Ganymede and Callisto show a high error in the along-track and cross-track directions, since the radius of their sphere of influence is quite larger than that of the inner moons' ones, hence there is more time for the perturbations to influence the orbit. A by-product of this research is the estimate of the Galilean moons' gravity field, in particular the new values for their J_2 and $C_{2,2}$ coefficients led to the conclusion that Io is less hydrostatic, while Europa and Callisto are more hydrostatic than previously thought.

Contents

Preface XI

Acknowledgements XIII

Glossary XV

Symbols . . . XV

Abbreviations . . . XVIII

1 Introduction 1

1.1 Background . . . 1

1.2 Research question . . . 1

1.3 Structure . . . 2

2 Heritage 3

2.1 The Galilean moons . . . 3

2.2 Missions in the Jovian system . . . 4

2.3 Synopsis: Missions towards the Galilean moons . . . 6

3 Astrodynamics 7

3.1 Approach . . . 7

3.2 JPL ephemerides characteristics . . . 7

3.3 Reference frame . . . 8

3.4 Coordinate system . . . 9

3.5 Equation of motion . . . 9

3.6 Perturbations . . . 10

3.6.1 Third-body perturbation . . . 10

3.6.2 Atmospheric drag . . . 14

3.6.3 Radiation pressure . . . 15

3.6.4 Electromagnetic perturbation . . . 17

3.6.5 Non-symmetric mass distribution . . . 19

3.6.6 Relativistic effects . . . 24

3.7 Synopsis: Perturbations relevance . . . 24

4 Integration 25

4.1 Integration type . . . 25

4.2 Integrator choice . . . 25

4.2.1 Integrators comparison . . . 25

4.2.2 Coordinates comparison . . . 29

4.3 Expressions for the chosen integrator . . . 30

4.4 Synopsis: Integrator . . . 31

5 Selection test cases and tuning integrator **33**
5.1 Orbit geometry . . . 33
5.2 Tuning of relative tolerance . . . 37
5.3 Tuning of data acquisition step-size . . . 39
5.4 Synopsis: Galileo's flybys selection . . . 42

6 Optimization **43**
6.1 State of the art optimization options . . . 43
6.2 First Initial State Grid Search . . . 45
6.3 First Spherical Harmonics Grid Search . . . 47
6.3.1 Sensitivity Considerations . . . 47
6.3.2 First spherical harmonics estimates . . . 47
6.4 Second Initial State Grid Search . . . 49
6.5 Second Spherical Harmonics Grid Search . . . 50
6.6 Synopsis: Optimization outcomes . . . 50

7 Further results **51**
7.1 Physical considerations . . . 51
7.2 Verification of the spherical harmonics coefficients . . . 53
7.3 Interpretation of the obtained RMSE . . . 55
7.4 Synopsis: Analysis of the results . . . 61

8 Validation **63**
8.1 Validation of the MATLAB script with ASTOS . . . 63
8.2 Synopsis: Validation of the script . . . 65

9 Conclusions and recommendations **67**
9.1 Final considerations . . . 67
9.2 Recommendations . . . 68

A Transformation between J2000 and PCPF **69**

B Transformation between J2000 and LO **71**

C Zonal Harmonics **73**

D Tesseral Harmonics **75**

E Variation of Galileo's distance from Earth **77**

F Spherical Harmonics **83**

G RMSE in LO components **87**

Bibliography **105**

Preface

The idea of doing my thesis project on this subject came after a combination of two events. Almost one year ago, I managed to find a library which lent a copy of the "Sidereus Nuncius", in which Galileo Galilei wrote in Latin, the scientific language of the time, to the future Grand Duke of Tuscany, Cosimo II de' Medici, to announce him his discovery of four satellites of Jupiter, now known as the Galilean moons, but at that time named Medicea Sidera (de' Medici's stars) in his honor. So I borrowed this astronomical treatise. I was still at the first page, when I received an e-mail from the managing director of Astos Solutions GmbH (in Stuttgart, Germany) telling me that I had been accepted for both an internship and the thesis project, and that he was interested in the analysis of the accuracy of the perturbed two-body problem about the Galilean moons. What I was supposed to do was clear to me. So we decided to plan the internship from August to November 2016, and the thesis project from November 2016 to June 2017.

Acknowledgements

I would first like to thank my supervisor ir. Ron Noomen for his assistance during the writing of this thesis. He has been constantly present and fundamental throughout the entire period. His friendly behavior has made this research pleasant and stimulating.

I would then like to acknowledge my supervisor at Astos Solutions GmbH, ir. Sven Schäff, who has been of precious help through his lessons about how to use ASTOS and his suggestions regarding how to proceed with the thesis project.

I would also like to thank ir. Valentino Zuccarelli, again from Astos Solutions GmbH, who has contributed to this work by proposing to me always different perspectives from which a problem can be seen.

Finally, I am grateful to my family, girlfriend and friends for their invaluable support throughout the last years.

This would not have been possible without all of them. Thank you.

Delft University of Technology — Alex Nardi
June 29, 2017

Glossary

Symbols

The list of Latin symbols present in this paper is shown in Table 1, with description and unit of measure, followed by the list of Greek symbols in Table 2.

Latin Symbols

Table 1: List of Latin symbols present in this paper, with description and unit of measure.

Symbol	Description	Unit
a	Acceleration	m s^{-2}
a	Semi-major axis	m
A	Area	m^2
az	Azimuth angle	rad
B	Spacecraft's ballistic coefficient	kg m^{-2}
B	Magnetic field strength	T
c	Speed of light (value: 299792458 (Wakker [2015]))	m s^{-1}
C	Corrected error constant of the Adams-Moulton integration method	various
C^*	Predicted error constant of the Adams-Bashforth integration method	various
C_D	Drag coefficient	-
$C_{n,m}$	Gravity field model parameter of degree n and order m	-
C_R	Satellite's reflectivity	-
D	Drag	N
$\vec{e}$	Unit vector	-
e	Eccentricity of an orbit	-
el	Elevation angle	rad
f	Propulsive acceleration	m s^{-2}
f	Derivative function in the PECE integration method	various
F	Force	N
F	Second equinoctial element	-
$g_{n,m}$	Gauss geomagnetic coefficient of degree n and order m	T
G	Universal gravitational constant (value: $6.67428 \cdot 10^{-11}$ (Wakker [2015]))	m^3 kg^{-1} s^{-2}
G	Third equinoctial element	-
h	Integration step-size	s
h	Altitude	m
h	Specific angular momentum	m^2 s^{-1}
H	Fourth equinoctial element	-
$h_{n,m}$	Gauss geomagnetic coefficient of degree n and order m	T

Symbol	Description	Unit
i	Inclination	rad
$J_{n,m}$	Gravity field parameter of degree n and order m	-
k	Number of steps in the PECE integration method	-
K	Fifth equinoctial element	-
L	Libration point	-
L	Sixth equinoctial element	rad
m	Order of a coefficient in a series	-
m	Mass of spacecraft	kg
M	Mass of celestial body	kg
n	Degree of a coefficient in a series	-
O	Origin of a reference frame	-
P	Point (identifying a body)	-
P	First equinoctial element	m
P	Power	W
$P_{n,m}$	Schmidt semi-normalized associated Legendre function of degree n and order m	-
q	Satellite's electric charge	C
$\vec{r}$	Position vector of a body	m
R	Rotation matrix	-
R	Radius of a body	m
$S_{n,m}$	Gravity field model parameter of degree n and order m	-
t	Time	s
T_{eq}	Equilibrium temperature	K
u	Argument of latitude	rad
u	Inverse of radius	m^{-1}
U	Specific gravitational potential	$m^2\ s^{-2}$
U	Magnetic potential	$V\ s\ m^{-1}$
U^*	Electrical potential difference	V
v	Spacecraft's relative velocity with respect to the atmosphere or the magnetic field	$m\ s^{-1}$
V	Velocity	$m\ s^{-1}$
W	Energy flux of the solar radiation	$W\ m^{-2}$
x	First component of a reference frame	m
y	Second component of a reference frame	m
y	Corrected solution of the PECE integration method	various
y^*	Predicted solution of the PECE integration method	various
z	Third component of a reference frame	m

Greek Symbols

Table 2: List of Greek symbols present in this paper, with description and unit of measure.

Symbol	Description	Unit
α	Constant in the PECE integration method	-
α	Right ascension of a body (spin state)	rad
β	Constant in the relativistic effect	-
β	Constant in the PECE integration method	-
β^*	Constant in the PECE integration method	-
δ	Declination of a body (spin state)	rad
Δ	Difference	various
ϵ	Emissivity	-
ϵ	Local truncation error of the PECE integration method	various
ϵ_0	Permittivity of free space	F m^{-1}
θ	True anomaly	rad
λ_{nh}	Nonhydrostatic parameter	-
λ	Longitude	rad
$\Lambda_{n,m}$	Gravity field parameter of degree n and order m	rad
μ	Gravitational parameter	m^3 s^{-2}
ρ	Density	kg m^{-3}
σ	Stefan-Boltzmann constant (value: $5.6704 \cdot 10^{-8}$ (Stam [2016]))	$\frac{W}{m^2 K^4}$
τ	Sidereal time angle of a body (spin state)	rad
ϕ	Latitude	rad
ω	Argument of pericenter	rad
Ω	Right ascension of the ascending node	rad

ABBREVIATIONS

The list of abbreviations present in this paper is shown in Table 3, with the description of their meaning.

Table 3: List of abbreviations present in this paper, with the description of their meaning.

Abbreviation	**Description**
AB	Adams-Bashforth integrator
ABM	Adams-Bashforth-Moulton integrator
AM	Adams-Moulton integrator
ASTOS	AeroSpace Trajectory Optimization Software
AU	Astronomical Unit (value: 149597870700 m (Wakker [2015]))
BBC	British Broadcasting Company
CB	Central Body
CBRP	Central Body's Radiation Pressure
EJSM	Europa-Jupiter System Mission
EM	ElectroMagnetic
EMFM	Europa Multiple-Flyby Mission
ESA	European Space Agency
JEO	Jupiter-Europa Orbiter
JGO	Jupiter-Ganymede Orbiter
JPL	Jet Propulsion Laboratory
JRP	Jovian Radiation Pressure
JUICE	JUpiter ICy moon Explorer
LO	Local Orbital frame
MATLAB	MATrix LABoratory
MD	Mass Distribution
NASA	National Aeronautics and Space Administration
PCPF	Planet-Centered Planet-Fixed frame
PECE	Predictor-Evaluator-Corrector-Evaluator integration method
PLATO	PLAnetary Transits and Oscillations of stars
REL	Relativistic effects
RKF	Runge-Kutta-Fehlberg integrator
RMSE	Root Mean Square Error
S/C	Spacecraft
s.o.i.	Sphere of influence
SPICE	Spacecraft and Planet ephemerides, Instruments description, C-matrix pointing and Events kernels
SRP	Solar Radiation Pressure
TB	Third Body
TBP	Third Body Perturbation

1
Introduction

In this chapter, the background of the topic will be presented, alongside with the definition of the research question and the structure of this paper.

1.1. Background

The Jovian system constitutes a scaled version of the Solar System: it has a central body with a significant mass, has a number of smaller bodies orbiting around (moons), smaller objects (rings) and magnetic field. As such, it can give insight into the origin of the universe and its own moons, which possess some of the characteristics needed for habitable environments; in particular Europa is very likely to possess all of them (Szondy [2013a]) and may thus be considered as a small Earth. This makes Jupiter and its environment an extremely interesting target for space missions. By virtue of the large number of moons, the Jovian system has been and will be always more attractive: Galileo (National Aeronautics and Space Administration, i.e. NASA) is its most important mission (it has performed from 1989 to 2003) in terms of number of flybys and scientific outcomes, but three other great missions are planned to go to this system in the next decade, i.e. Jupiter Icy Moons Explorer (JUICE), by the European Space Agency (ESA), Europa Multiple-Flyby Mission (EMFM) and Europa-Jupiter System Mission (EJSM) by NASA, where the latter will be composed of two orbiters, one for Europa (for the Jupiter-Europa Orbiter (JEO) sub-mission) and one for Ganymede (for the Jupiter-Ganymede Orbiter (JGO) sub-mission); these two moons are suspected to have subsurface oceans (NASA [2009]). The relevance of the Galilean moons is hence evident.

1.2. Research question

In order to have an idea of the reliability and accuracy of the information known about these moons, it is necessary to have the nominal trajectory of the spacecraft, which can be obtained through the SPICE program. From these considerations, the following research question of this project has hence arisen:

What is the quality of the trajectory followed by the Galileo spacecraft during its flybys about the Galilean moons?

It is clear that the answer to this research question shall identify the relevant elements which play a relevant role in the determination of the accuracy of the trajectory (i.e. model, parameters, measurements and orbit geometry), and also suggest options capable of improving it in future missions.

1.3. STRUCTURE

This research is divided into nine chapters, the first of which is this introduction. The second chapter presents the heritage of the problem, in which past missions towards the Jovian system are presented to the reader, and the most important characteristics of the Galilean moons are described. The third faces the astrodynamics of this research, by defining the frame and coordinates used, presenting the equations of motion and analyzing the major perturbations during these flybys. The fourth chapter deals with the choice of the best integration technique for the propagation of the spacecraft's state, while the Galileo's flybys selection is treated in the fifth one. Chapter 6 presents the optimization part of the problem, in which the initial state of the spacecraft and the spherical harmonics of the moons are optimized in such a way that the minimum root mean square error with respect to the JPL ephemerides results. In the seventh chapter, the estimated spherical harmonics are verified by introducing other flybys; furthermore physical considerations related to the new values of the harmonics are shown, and at the end the obtained errors are interpreted. The validation of the script written to accomplish all these tasks is done by means of a comparison with the ASTOS software in chapter 8. The last one describes the conclusions of this study, by presenting the answer to the research question alongside with the recommendations for readers which would like to expand this work in the future.

2
HERITAGE

At the beginning of this chapter, the main peculiarities of the Galilean moons are explained. Then, the spacecraft which have entered the Jovian sphere of influence will be presented. Future missions with this characteristic will be discussed too.

2.1. THE GALILEAN MOONS

The Italian astronomer and physicist Galileo Galilei discovered the Galilean moons (named after him; formerly addressed as Medicea Sidera) in January of 1610, according to page 1 of Galilei [1610].

Missions towards gas giants' moons can turn out to be fundamental in terms of novelties added to the body of knowledge. One of the most important objectives of this kind of missions is the search for a habitable environment in the Solar System. Note that, according to pages 459-460 of Lissauer and de Pater [2013], a celestial body is said to be habitable only when four main characteristics are present: liquid water, a stable environment, the essential elements and chemical energy. The state-of-the-art knowledge about habitability of Solar System celestial bodies is well described in Figure 2.1 (Szondy [2013b]).

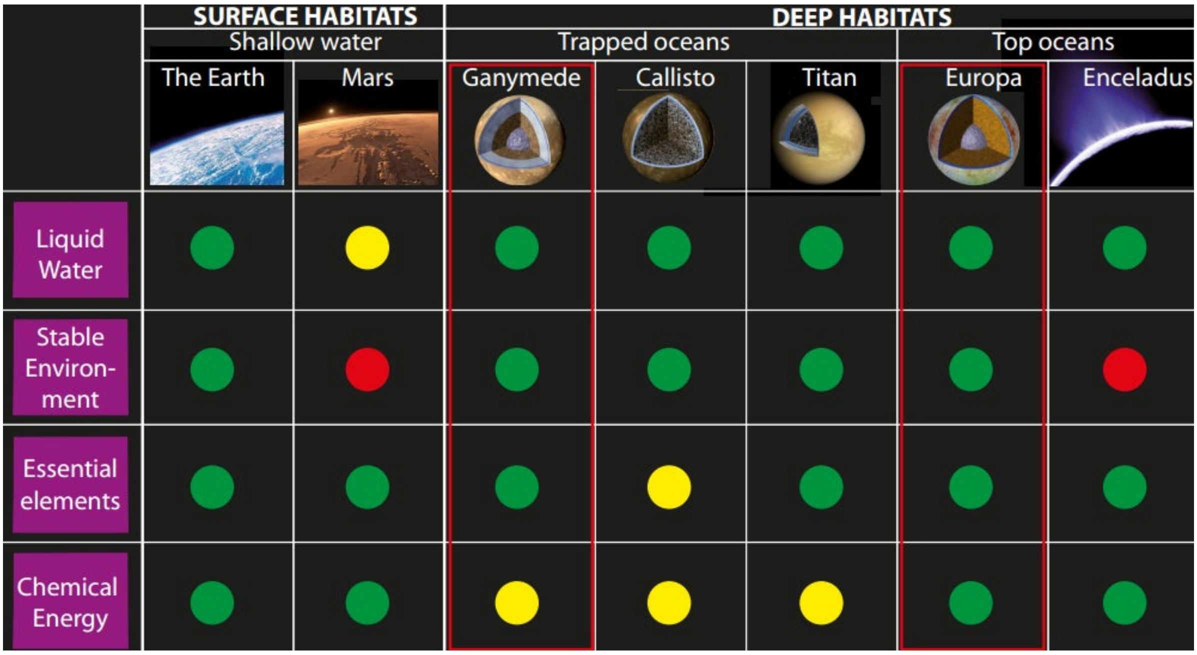

Figure 2.1: Habitability of some environments; all four criteria have to be fulfilled to achieve habitability. A red circle means that a specific criterion is not fulfilled, yellow indicates that it is likely satisfied but not demonstrated, and green that it is very likely or demonstrated (Szondy [2013b]).

According to Figure 2.1 (Szondy [2013b]), Europa seems to satisfy all four criteria, while Ganymede and Callisto are only likely to have enough chemical energy to support life, but it is not demonstrated yet. However, these doubts can be solved through flybys and, in the future, landings. For this reason, the moons treated in this paper are of paramount importance.

2.2. MISSIONS IN THE JOVIAN SYSTEM

The missions in which spacecraft entered the Jovian system are presented in Table 2.1 (Wikipedia [2017a]) in chronological order.

Table 2.1: Missions of spacecraft which entered the Jovian system, with year, name of the spacecraft and kind of mission (Wikipedia [2017a]).

Year	**Spacecraft**	**Mission**
1973	Pioneer 10	Jupiter flyby
1974	Pioneer 11	Jupiter flyby
1979	Voyager 1	Jupiter flyby
1979	Voyager 2	Jupiter flyby
1995-2003	Galileo	moons flybys and orbiter
1992-2004	Ulysses	Jupiter flyby
2000	Cassini-Huygens	Jupiter flyby
2007	New Horizons	Jupiter flyby
2016-present	Juno	Jupiter flybys and orbiter

Among these, the Galileo spacecraft is the only one which has provided a detailed characterization of Jupiter and, overall, its moons as can be realized by reading a piece of NASA [2010], where its scientific contribution to the body of knowledge is presented:

"Galileo plunged into Jupiter's crushing atmosphere on Sept. 21, 2003. The spacecraft was deliberately destroyed to protect one of its own discoveries - a possible ocean beneath the icy crust of the moon Europa. Galileo changed the way we look at our solar system. The spacecraft was the first to fly past an asteroid and the first to discover a moon of an asteroid. It provided the only direct observations of a comet colliding with a planet. Galileo was the first to measure Jupiter's atmosphere with a descent probe and the first to conduct long-term observations of the Jovian system from orbit. It found evidence of subsurface salt-water on Europa, Ganymede and Callisto and revealed the intensity of volcanic activity on Io."

This has been made real thanks to the large number of flybys of Jupiter and its moons, as shown in Figure 2.2 (University of Colorado Boulder [2004]).

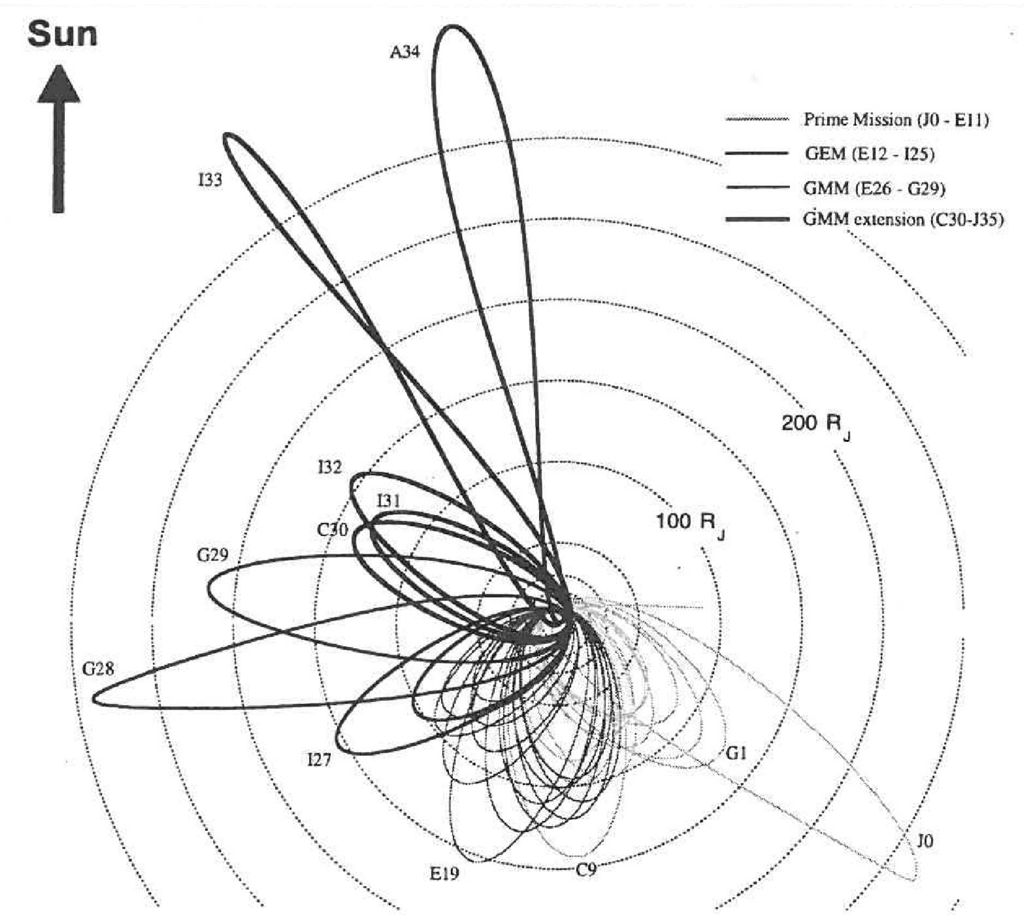

Figure 2.2: Flybys of the Galileo spacecraft in the Jovian system between 1995 and 2003 (University of Colorado Boulder [2004]). The Sun is toward the top of the image, while "A" stands for "Amalthea", "C" for Callisto, "E" for Europa, "G" for Ganymede, "I" for Io, and "J" for Jupiter.

The Galileo mission provides also the latest information about the Galilean moons, which thus dates back to 1989-2003 (Szondy [2013a]).

The Juno mission (launched in 2016 and currently ongoing) has objectives similar to those of Galileo, mostly related to Jupiter's atmosphere, magnetosphere and gravity field (NASA [2016b]); it has entered an orbit about Jupiter on July 4^{th}, 2016 (NASA [2016c]) and it is expected to provide useful information about the above-mentioned Jovian physical characteristics.

Future evidence about the exact state of these moons will hopefully be provided by the JUICE mission (ESA and partners), whose launch is expected to be in June 2022. Its overall mission profile is presented in Table 2.2 (ESA [2014]).

Table 2.2: Overall mission profile of the JUICE mission (ESA [2014]).

06/2022 - Launch by Ariane-5 ECA + EVEE Cruise		
01/2030 - Jupiter orbit insertion		
	Jupiter tour	
		Transfer to Callisto (11 months)
		Europa phase: 2 Europa and 3 Callisto flybys (1 month)
		Jupiter High Latitude Phase: 9 Callisto flybys (9 months)
		Transfer to Ganymede (11 months)
09/2032 – Ganymede orbit insertion		
	Ganymede tour	
		Elliptical and high altitude circular phases (5 months)
		Low altitude (500 km) circular orbit (4 months)
06/2033 – End of nominal mission		

From Table 2.2 (ESA [2014]), it can be expected that much more about the gravitational and magnetic field of Europa, Callisto, Ganymede and of course Jupiter will be known after completion of the mission, thanks to the numerous flybys at varying altitudes. This will definitely improve the current knowledge of these fields by means of model parameters and analytical expressions, and thus will lead to the possibility of also taking into account smaller perturbations. In order to have a clear and more complete idea about the Jovian system, also the magnetic and plasma interactions of these moons with Jupiter's magnetosphere will be studied.

Finally, more relevant information about the presence of a subsurface ocean on Europa will be provided by NASA Europa Multiple-Flyby Mission (EMFM; formerly known as Europa Clipper), which should have launched in 2022, but due to budget restrictions, the launch would probably be delayed to mid or even late 2020s (page 734 of NASA [2017]).

2.3. SYNOPSIS: MISSIONS TOWARDS THE GALILEAN MOONS

In the past, only the Galileo spacecraft entered the Galilean moons' sphere of influence and provided detailed information about their gravity field, atmosphere, magnetosphere and possible internal structure. In the future, the EMFM will flyby Europa to investigate about the possibility of a subsurface ocean, while the JUICE mission will focus also on the other three moons by means of many flybys, with pericenter at various altitudes to add relevant information about these moons to our body of knowledge.

3

ASTRODYNAMICS

In this chapter, the choice of the reference frame and the coordinates will be investigated, as well as the equations of motion and the main perturbations.

3.1. APPROACH

The flybys done between 1995 and 2002 by the Galileo spacecraft will be analyzed with a perturbed two-body problem formulation, since Galileo is always inside the Jovian moons' spheres of influence for the selected cases. This lets us consider the influence of other relevant bodies, such as Jupiter, as third-body perturbations without focusing on the modeling of the three-body problem.

In order to have an easy formulation of the problem, the three-body model does force the orbits of the two main bodies to be circular (or elliptical), but, in the case of flybys about moons, they are not concentric, since the two bodies are in general the moon and its planet, which respectively orbit about the planet and the Sun. For this reason, a perturbed two-body approach has been chosen to be implemented for the propagation of the orbit.

3.2. JPL EPHEMERIDES CHARACTERISTICS

The nominal JPL ephemerides are affected by an error: the Chebyshev interpolation error, which, due to the age of the observation data, can reach 9 meters (NASA [2004]). Note that this limitation is caused by the lack of accuracy of the Galilean moons' ephemerides file (the state of the spacecraft with respect to the moon is computed as the vectorial difference between the observed spacecraft's and the moon's one with respect to the Earth), while a new file with a much better accuracy (0.5 m, according to NASA [2013]) has been made available in 2013. It is clear that a more accurate ephemerides data of the moons is not enough to obtain more accurate data of the spacecraft too, because the observed state of Galileo with respect to the Earth is not provided by SPICE. For this goal, new ephemerides of the Galileo state with respect to the moons shall be obtained as difference between those of Galileo and those of the moons, both as observed, i.e. considered with respect to Earth .

3.3. REFERENCE FRAME

For simplicity reasons, the perturbed two-body problem will be described with respect to a (quasi-)inertial reference frame, centered in the central body's center of mass and with the axes directed as the J2000 ones, as illustrated in Figure 3.1 (page 10 of NASA [2017]):

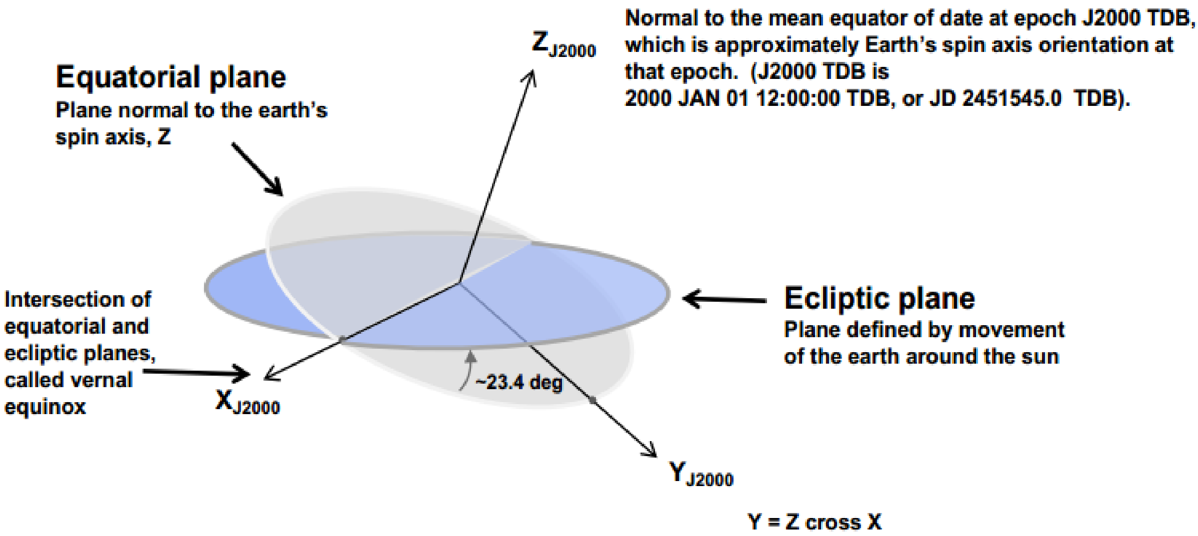

Figure 3.1: Description of the J2000 reference frame (page 10 of NASA [2017]).

Please note that the chosen reference frame is J2000, because it allows an easy formulation of the equations of motion and it is possible to extract the state of celestial bodies and spacecraft in J2000 coordinates with respect to any other body by means of the JPL SPICE software.

This frame can of course be centered in any body without needing rotations, since only the origin of the frame (which corresponds to the body's center of mass) changes, but the directions of the axes remain constant.

Two other frames will be needed: the Planet-Centered Planet-Fixed (PCPF) and the Local Orbital (LO) frames. They are both rotating frames, but the first is centered in the celestial body's center of mass; its X- and Y- axes lie in the equatorial plane. The X-axis points toward the prime meridian, while the Z-axis is perpendicular to the equatorial plane and points toward the geographic north; the Y-axis finally completes the right-handed system. The LO frame is instead centered in the spacecraft's center of mass; the X-axis points radially outwards (i.e. the direction is the one from the celestial body's to the spacecraft's center of mass). The Z-axis is directed as the osculating angular momentum (thus perpendicular to the momentary orbital plane); the Y-axis completes the right-handed system. Note furthermore that the motion of the moons is not an issue, since the barycenter of the system composed by moon (central body) and spacecraft is roughly coincident with the moon's center of mass, due to the fact that the mass of the spacecraft is negligible with respect to that of one moon.

Please note that the transformations in which these two frames are involved are described in Appendices A and B.

3.4. COORDINATE SYSTEM

The state of the spacecraft can in principle be described with many different sets of coordinate systems. Here we highly focus on the most relevant ones: Cartesian, Keplerian and modified equinoctial elements.

The Cartesian coordinates make use of three components (along perpendicular axes) for the position and three for the velocity. The Keplerian ones use six elements which describe the shape, size and orientation of the orbit, but can lead to singularities for null eccentricity or inclination. The six modified equinoctial elements solve these singularities by decomposing the eccentricity vector along two perpendicular axes and introducing two elements (H and K) which directly depend on the inclination.

Since the Keplerian coordinates can lead to singularities, Cartesian coordinates and modified equinoctial elements will only be considered and compared in Subsection 4.2.2. There, it will be proved that modified equinoctial elements show a more accurate and fast propagation than Cartesian coordinates, and will hence be used.

3.5. EQUATION OF MOTION

The equation of motion which describes the spacecraft's acceleration with respect to its central body is presented in Equation (3.1) (page 117 of Wakker [2015]):

$$\frac{d^2\vec{r}}{dt^2} = -\frac{\mu}{r^2}\hat{r} \tag{3.1}$$

where $\vec{r}$ indicates the spacecraft's position with regard to the central body (by means of the x, y, z coordinates described in the reference frame presented in Section 3.3), $\hat{r}$ its normalization, while μ is the central body's gravitational parameter. In particular, $\mu = GM$, with G the universal gravitational constant and M the central body's mass. In view of the mass ratio between the spacecraft and the moons (in the worst case, it is in the order of 10^{-20}, by considering Europa as central body), Equation (3.1) is a valid description.

In order to have a more general form of Equation (3.1), Equation (3.2) is presented:

$$\frac{d^2\vec{r}}{dt^2} = -\frac{\mu}{r^2}\hat{r} + \vec{a}_P \tag{3.2}$$

where $\vec{a}_P$ represents a generic perturbing acceleration vector.

Equations (3.1) and (3.2) are usually in Cartesian coordinates, but the used equations of motion are in equinoctial elements: they are presented in the System of Equations (3.3) (pages 39-40 of Jo et al. [2011b]):

$$
\begin{cases}
\frac{dP}{dt} = \frac{2P}{w}\sqrt{\frac{p}{\mu}}F_T \\
\frac{dF}{dt} = \sqrt{\frac{p}{\mu}}\Big(F_N \cdot sin(L) + \big((w+1)cos(L)+F\big)\frac{F_T}{w} - \big(H\ sin(L) - K\ cos(L)G\big)\frac{F_O}{w}\Big) \\
\frac{dG}{dt} = \sqrt{\frac{p}{\mu}}\Big(-F_N \cdot cos(L) + \big((w+1)sin(L)+G\big)\frac{F_T}{w} + \big(H\ sin(L) - K\ cos(L)F\big)\frac{F_O}{w}\Big) \\
\frac{dH}{dt} = \frac{1}{2}\sqrt{\frac{p}{\mu}}\Big(1+H^2+K^2\Big)\frac{F_O}{w}cos(L) \\
\frac{dK}{dt} = \frac{1}{2}\sqrt{\frac{p}{\mu}}\Big(1+H^2+K^2\Big)\frac{F_O}{w}sin(L) \\
\frac{dL}{dt} = \sqrt{P\mu}\frac{w^2}{P^2} + \frac{\sqrt{\frac{p}{\mu}}}{w}\Big(H\ sin(L) - K\ cos(L)\Big)F_O
\end{cases}
\tag{3.3}
$$

where P, F, G, H, K, L represent the nonsingular elements, F_N, F_T, F_O the three components of the acceleration along the X-, Y- and Z- axes of the LO frame, and w is defined as $w = 1 + F \cdot cos(L) + G \cdot sin(L)$. In case there are no perturbations, all equinoctial elements, except for L, remain constant.

Note also that the equations to transform from Keplerian to equinoctial elements and vice-versa are presented at page 39 of Jo et al. [2011b], while the ones between Cartesian and Keplerian are given on page 135 to 137 of Larson and Wertz [1992].

3.6. PERTURBATIONS

The most relevant perturbations will now be described, and the question about whether they are negligible or necessary for a flyby-case scenario will be addressed.

3.6.1. THIRD-BODY PERTURBATION

The presence of other celestial bodies does influence the orbit of the spacecraft in such a way that, depending on the desired accuracy, they may have to be considered in the dynamical model.

At page 113 of Wakker [2015], a representation of the third-body perturbation is presented; a modified version of it is shown in Figure 3.2:

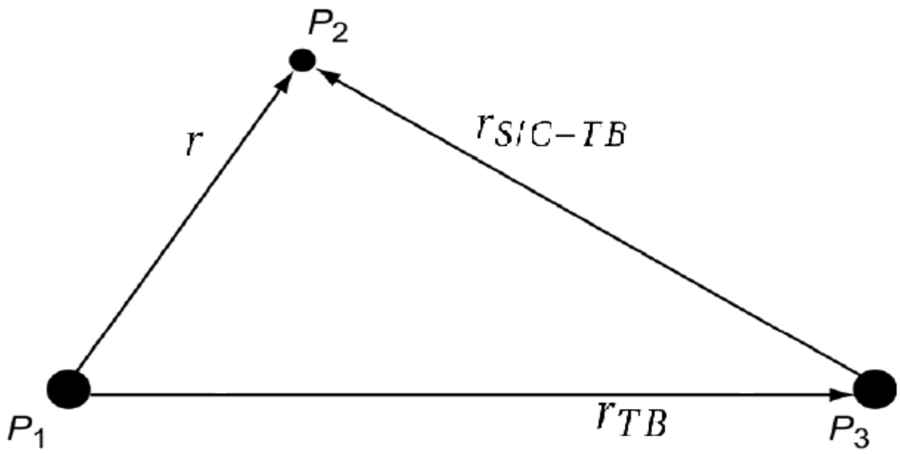

Figure 3.2: Relative positions of the central body P_1, the spacecraft P_2 and the third body P_3 (modified from page 113 of Wakker [2015]).

According to page 112 of Wakker [2015], the disturbing acceleration due to the presence of a third body can be described by Equation (3.4):

$$\vec{a}_{TBP} = -\mu_{TB}\left(\frac{1}{r^2_{S/C-TB}}\hat{r}_{S/C-TB} + \frac{1}{r^2_{TB}}\hat{r}_{TB}\right) \tag{3.4}$$

where $\hat{r}_{TB}$ indicates the unit position vector of the third body with respect to the central body, while $\hat{r}_{S/C-TB}$ is the unit position vector of the spacecraft with respect to the third body; furthermore, μ_{TB} indicates the gravitational parameter of the third body. Note that in general there can be more than one third body: in such a case all the perturbing accelerations will have to be added up.

Since it is desired to study the magnitude of this acceleration with respect to the central one defined in Equation (3.1) (from now onwards addressed as a_{MAIN} for simplicity) in order to assess whether a third body is relevant or not, the ratio of their magnitude should be maximized to consider the worst-case scenario. Since each scenario will only be considered inside the sphere of influence of a moon, the minimum value for a_{MAIN} will be obtained when the distance between spacecraft and main body is maximum, i.e. the radius of the sphere of influence itself. Furthermore, since the acceleration due to a third body decreases with the increase of the distance of the spacecraft from it, it can be assessed that this distance should be minimum, i.e. the third body's center of mass shall be on the line connecting central body and spacecraft and at the minimum distance from the spacecraft. Thus, the perturbing acceleration can be written as in Equation (3.5):

$$\vec{a}_{TBP_{max}} = -\mu_{TB}\left(\frac{1}{(r_{TB}-R_{s.o.i.})^2} - \frac{1}{r^2_{TB}}\right)\hat{r} \tag{3.5}$$

where $R_{s.o.i.}$ indicates the radius of the sphere of influence of the relevant Galilean moon with respect to Jupiter.

For these reasons, the ratio of the norms of the accelerations can be described as in Equation (3.6):

$$\left(\frac{a_{TBP}}{a_{MAIN}}\right)_{max} = \left(\frac{\mu_{TB}\left(\frac{1}{(r_{TB}-R_{s.o.i.})^2}-\frac{1}{r_{TB}^2}\right)}{\frac{\mu}{R_{s.o.i.}^2}}\right)_{max} = \frac{\mu_{TB}}{\mu}R_{s.o.i.}^2\left(\frac{1}{(r_{TB}-R_{s.o.i.})^2}-\frac{1}{r_{TB}^2}\right)_{max} = \\ = \frac{\mu_{TB}}{\mu}R_{s.o.i.}^2\left(\frac{1}{(r_{TB_{min}}-R_{s.o.i.})^2}-\frac{1}{r_{TB_{min}}^2}\right) \tag{3.6}$$

When Jupiter is considered as the third body, then $r_{TB_{min}}$ is simply the pericenter of the Galilean moon's orbit about it. When the third body is another planet instead, Equation (3.7) holds true:

$$r_{TB_{min}} = \left|r_{Jupiter-Sun} - r_{Planet-Sun}\right| - r_{Central\,Body\,Galilean\,moon-Jupiter} \tag{3.7}$$

where in particular $r_{Central\,Body\,Galilean\,moon-Jupiter}$ indicates the apocenter distance of the Galilean moon with regard to Jupiter.

Please note that also the Sun can be considered as a third body, but in this case $r_{Planet-Sun}$ would be zero, and that is why the subscript of this variable refers to planet.

Finally, in order to provide quantitative values to the ratio of the accelerations defined in Equation (3.6), a value for $R_{s.o.i.}$ is needed. According to page 115 of Wakker [2015], Equation (3.8) can be used:

$$R_{s.o.i.} \approx R_{s.o.i._{max}} \approx r_{TB}\left(\frac{M}{M_{Jupiter}}\right)^{\frac{2}{5}} \tag{3.8}$$

where M indicates the mass of the central body and $M_{Jupiter}$ that of Jupiter.

Table 3.1 presents the radii of the spheres of influence of the Galilean moons with respect to Jupiter, as computed by using Equation (3.8), and the main acceleration exerted by them on the spacecraft:

Table 3.1: Radii of the spheres of influence of the Galilean moons with respect to Jupiter, and corresponding two-body gravitational acceleration. The radii of the moons are shown for comparison purposes.

Galilean moon	**Radius of the moon** [km]	**Radius of the sphere of influence** [km]	**Main acceleration at the sphere of influence** [m/s^2]
Io	1822	7834	$9.7\cdot10^{-2}$
Europa	1561	9722	$3.4\cdot10^{-2}$
Ganymede	2634	24350	$1.7\cdot10^{-2}$
Callisto	2410	37681	$5.1\cdot10^{-3}$

Table 3.2 includes the ratio of the accelerations computed for the most relevant celestial bodies, such as the planets, the Sun and the Galilean moons different from the central body.

Table 3.2: Values of third-body accelerations and accelerations ratio for the most relevant celestial bodies, computed at the radii of the spheres of influence specified in Table 3.1.

Galilean moon	**Third body**	**Third-body acceleration value** [m/s^2]	**Accelerations ratio**
Io	Sun	$4.4\cdot10^{-9}$	$4.5\cdot10^{-8}$
	Mercury	$9.3\cdot10^{-16}$	$9.5\cdot10^{-15}$
	Venus	$1.7\cdot10^{-14}$	$1.7\cdot10^{-13}$
	Earth	$2.5\cdot10^{-14}$	$2.6\cdot10^{-13}$
	Mars	$4.0\cdot10^{-15}$	$4.2\cdot10^{-14}$
	Jupiter	$2.7\cdot10^{-2}$	$2.8\cdot10^{-1}$
	Saturn	$2.2\cdot10^{-12}$	$2.2\cdot10^{-11}$
	Uranus	$9.9\cdot10^{-15}$	$1.0\cdot10^{-13}$
	Neptune	$2.1\cdot10^{-15}$	$2.1\cdot10^{-14}$
	Pluto	$1.1\cdot10^{-19}$	$1.2\cdot10^{-18}$
	Amalthea	$3.0\cdot10^{-11}$	$3.1\cdot10^{-10}$
	Europa	$3.4\cdot10^{-6}$	$3.5\cdot10^{-5}$
	Ganymede	$5.8\cdot10^{-7}$	$6.0\cdot10^{-6}$
	Callisto	$3.6\cdot10^{-8}$	$3.7\cdot10^{-7}$
Europa	Sun	$5.5\cdot10^{-9}$	$1.6\cdot10^{-7}$
	Mercury	$1.1\cdot10^{-15}$	$3.4\cdot10^{-14}$
	Venus	$2.1\cdot10^{-14}$	$6.2\cdot10^{-13}$
	Earth	$3.1\cdot10^{-14}$	$9.2\cdot10^{-13}$
	Mars	$5.0\cdot10^{-15}$	$1.5\cdot10^{-13}$
	Jupiter	$8.3\cdot10^{-3}$	$2.5\cdot10^{-1}$
	Saturn	$2.7\cdot10^{-12}$	$7.9\cdot10^{-11}$
	Uranus	$1.2\cdot10^{-14}$	$3.6\cdot10^{-13}$
	Neptune	$2.6\cdot10^{-15}$	$7.6\cdot10^{-14}$
	Pluto	$1.4\cdot10^{-19}$	$4.2\cdot10^{-18}$
	Amalthea	$9.1\cdot10^{-12}$	$2.7\cdot10^{-10}$
	Io	$8.0\cdot10^{-6}$	$2.3\cdot10^{-4}$
	Ganymede	$3.1\cdot10^{-6}$	$9.2\cdot10^{-5}$
	Callisto	$7.9\cdot10^{-8}$	$2.3\cdot10^{-6}$
Ganymede	Sun	$1.4\cdot10^{-8}$	$8.3\cdot10^{-7}$
	Mercury	$2.9\cdot10^{-15}$	$1.7\cdot10^{-13}$
	Venus	$5.3\cdot10^{-14}$	$3.2\cdot10^{-12}$
	Earth	$7.9\cdot10^{-14}$	$4.7\cdot10^{-12}$
	Mars	$1.3\cdot10^{-14}$	$7.5\cdot10^{-13}$
	Jupiter	$5.2\cdot10^{-3}$	$3.1\cdot10^{-1}$
	Saturn	$6.7\cdot10^{-12}$	$4.0\cdot10^{-10}$
	Uranus	$3.1\cdot10^{-14}$	$1.8\cdot10^{-12}$
	Neptune	$6.4\cdot10^{-15}$	$3.9\cdot10^{-13}$
	Pluto	$3.5\cdot10^{-19}$	$2.1\cdot10^{-17}$
	Amalthea	$5.7\cdot10^{-12}$	$3.4\cdot10^{-10}$
	Io	$1.1\cdot10^{-6}$	$6.8\cdot10^{-5}$
	Europa	$2.7\cdot10^{-6}$	$1.6\cdot10^{-4}$
	Callisto	$6.8\cdot10^{-7}$	$4.1\cdot10^{-5}$
Callisto	Sun	$2.1\cdot10^{-8}$	$4.2\cdot10^{-6}$
	Mercury	$4.5\cdot10^{-15}$	$8.9\cdot10^{-13}$
	Venus	$8.2\cdot10^{-14}$	$1.6\cdot10^{-11}$
	Earth	$1.2\cdot10^{-13}$	$2.4\cdot10^{-11}$
	Mars	$2.0\cdot10^{-14}$	$3.9\cdot10^{-12}$
	Jupiter	$1.5\cdot10^{-3}$	$2.9\cdot10^{-1}$
	Saturn	$1.0\cdot10^{-11}$	$2.1\cdot10^{-9}$
	Uranus	$4.8\cdot10^{-14}$	$9.4\cdot10^{-12}$
	Neptune	$1.0\cdot10^{-14}$	$2.0\cdot10^{-12}$

Callisto	Pluto	$5.5{\cdot}10^{-19}$	$1.1{\cdot}10^{-16}$
	Amalthea	$1.6{\cdot}10^{-12}$	$3.2{\cdot}10^{-10}$
	Io	$1.5{\cdot}10^{-7}$	$3.0{\cdot}10^{-5}$
	Europa	$1.4{\cdot}10^{-7}$	$2.8{\cdot}10^{-5}$
	Ganymede	$1.5{\cdot}10^{-6}$	$3.0{\cdot}10^{-4}$

The values of μ of Jupiter and its moons have been taken from NASA [2004] (the ones used for the creation of the ephemerides of the Jovian system), while the others come directly from the Horizons Web Interface.

From Table 3.2, it can be concluded that the relevant celestial bodies to be considered are the Sun, Jupiter and the three Galilean moons different from the central body. In particular, Jupiter has an influence which is much higher than all the other bodies put together.

3.6.2. ATMOSPHERIC DRAG

The Galilean moons have a dust environment, which can be treated similarly to atmospheric drag. Motion in space generates drag, in a direction opposite to motion, and lift, perpendicular to it. Lift can be neglected due to the fact that it is far smaller than drag (page 534 of Wakker [2015]), while drag shall be analyzed deeper, since it can be significant, in particular in lower atmospheres. The equation for the acceleration acting on a satellite due to atmospheric drag is the following (page 534 of Wakker [2015]):

$$\vec{a}_D = -\frac{1}{2}\rho\frac{C_D{\cdot}A}{m}|\vec{v}|\vec{v} = -\frac{1}{2}\rho\frac{1}{B}|\vec{v}|\vec{v} \tag{3.9}$$

where ρ indicates the atmosphere's density, C_D the drag coefficient related to a surface A, m the mass of the satellite, $\vec{v}$ its velocity vector with respect to the atmosphere, and B the satellite's ballistic coefficient (page 64 of Wertz [1978]).

According to page 233 and 234 of Bagenal et al. [2006], the worst-case scenario for the Galilean moons happen at the lowest altitudes, where the number of molecules of dust per unit of volume (called number density) can increase up to $1{\cdot}10^{-3}$ m^{-3}, for an altitude of about 100 km. Each molecule has an average mass of $1{\cdot}10^{-15}$ kg, thus the mean density is about $1{\cdot}10^{-18}\ \frac{\text{kg}}{\text{m}^3}$. By using the open-source Horizons Web Interface, it can be stated that the maximum velocity of the spacecraft with respect to each Galilean moon's atmosphere is obtained at their closest approaches: 8.9 km/s at 102 km from Io's surface on January 17, 2002, 6.3 km/s at 201 km from Europa's surface on December 16, 1997, 8.0 km/s at 261 km from Ganymede's surface on September 6, 1996 and 9.7 km/s at 138 km from Callisto's surface on May 25, 2001. By using these maximum velocities and a satellite's ballistic coefficient equal to 25 $\frac{\text{kg}}{\text{m}^2}$ (for conventional spacecraft, it may range from 25 to 100 $\frac{\text{kg}}{\text{m}^2}$ according to page 64 of Wertz [1978]: 25 $\frac{\text{kg}}{\text{m}^2}$ will be used, as worst case), the ratio between the acceleration acting on the satellite due to the atmospheric drag and the central one (at altitude zero) can finally be computed for each moon. In particular, for Io it has a value of $9.7{\cdot}10^{-13}$, for Europa of $7.7{\cdot}10^{-13}$, for Ganymede of $1.1{\cdot}10^{-12}$, while for Callisto of $1.7{\cdot}10^{-12}$.

These ratios confirm that the moons' atmospheres do not play any relevant role in this analysis, since they are so thin and tenuous that they can definitely be neglected.

3.6.3. RADIATION PRESSURE

The main sources of radiation pressure exerted on the Galileo spacecraft can be three in these scenarios: the Sun, Jupiter and the central body.

SOLAR RADIATION PRESSURE

The acceleration acting on the spacecraft due to Solar radiation is, from pages 541 and 542 of Wakker [2015], given by Equation (3.10):

$$\vec{a}_{SRP} = C_R \frac{W\ A}{m\ c} \hat{r}_{S/C-Sun} \tag{3.10}$$

where C_R is the satellite's reflectivity, W the energy flux (or power density) of the Solar radiation, A the effective satellite's cross-sectional area, m the mass of the satellite, c the speed of light and $\hat{r}_{S/C-Sun}$ the unit vector directed from the satellite to the Sun. The formula from page 90 of Lissauer and de Pater [2013] can be used:

$$W = \frac{W_{1AU}}{\left(\frac{r_{S/C-Sun}}{1AU}\right)^2} \tag{3.11}$$

where $W_{1AU} = 1367.6\ \mathrm{W/m^2}$ (value taken from the Horizons interface) is the Solar constant.

Here we use $c = 2.99792458{\cdot}10^8$ m/s (page 671 of Wakker [2015]) and physical values of the Galileo spacecraft, i.e. $m = 2223$ kg, $A \approx 82.536\ \mathrm{m^2}$ (by considering the worst-case scenario of page 9 of Jouannic et al. [2015] in which all panels are parallel to each other, just for an order of magnitude computation) and $C_R = 1.5$ (page 10 of Jouannic et al. [2015]). Furthermore, since the four moons have approximatively the same distance from the Sun, the maximum ratio between this perturbation and the central acceleration happens when the central acceleration is minimum, i.e. at the sphere of influence of Callisto, according to Table 3.1. It holds true that at the limit of the Callisto's sphere of influence (with $r_{S/C-Sun} \approx 7.8{\cdot}10^{11}$ m), the ratio between the perturbing and the main acceleration is about $1.8{\cdot}10^{-6}$. In the worst-case of the "best" moon instead, i.e. at the Io's sphere of influence, this ratio decreases to $9.6{\cdot}10^{-8}$.

Clearly, the Solar radiation pressure can be neglected for all the four moons, since its ratio with respect to the main gravitational acceleration is smaller than the relative influence of realistic third bodies (Table 3.2).

JOVIAN RADIATION PRESSURE

The acceleration acting on the spacecraft due to the Jovian radiation can be modeled as Equation (3.10) as well, with a slight modification as can be seen in Equation (3.12):

$$\vec{a}_{JRP} = C_R \frac{W_{Jup}\ A}{m\ c} \hat{r}_{S/C-Jup} \tag{3.12}$$

where W_{Jup} indicates the correspondent of the Solar constant for Jupiter, while $\hat{r}_{S/C-Jup}$ the unit vector directed from the satellite to Jupiter.

Stam [2016] states that W_{Jup} can be found as described in Equation (3.13):

$$W_{Jup} = \frac{P_{out_{Jup}}}{4\pi r^2_{S/C-Jup}} \tag{3.13}$$

where $P_{out_{Jup}}$ is the power of the radiation emitted by Jupiter.

In particular, $P_{out_{Jup}}$ can be written (Stam [2016]) as in Equation (3.14):

$$P_{out_{Jup}} = 4\pi R^2_{Jup} \epsilon_{Jup} \sigma T^4_{eq_{Jup}} \tag{3.14}$$

where R_{Jup} represents the radius of Jupiter, ϵ_{Jup} its emissivity, $T_{eq_{Jup}}$ its equilibrium temperature, and σ the Stefan-Boltzmann constant.

According to Stam [2016], the emissivity of the celestial bodies can be approximated to 1, while its equilibrium temperature to roughly 123 K. Furthermore, the Jovian mean radius is $6.9911 \cdot 10^7$ m (Horizons interface) and the Stefan-Boltzmann constant is equal to $5.6704 \cdot 10^{-8}\ \frac{\mathrm{W}}{\mathrm{m^2 K^4}}$ (Stam [2016]). The worst-case scenario happens when the ratio of the acceleration is maximum, i.e. (by neglecting the constant part) when $\frac{1}{\mu}\left(\frac{R_{s.o.i.}}{r_{CB-Jup}-R_{s.o.i.}}\right)^2$ is maximum, that is at Europa's sphere of influence. Note indeed that the values for this ratio are about $6.0 \cdot 10^{-17}\ \mathrm{s^2/m^3}$, $6.8 \cdot 10^{-17}\ \mathrm{s^2/m^3}$, $5.5 \cdot 10^{-17}\ \mathrm{s^2/m^3}$ and $5.8 \cdot 10^{-17}\ \mathrm{s^2/m^3}$ respectively for Io, Europa, Ganymede and Callisto.

At the limit of Europa's sphere of influence, where $r_{S/C-Jup} \approx 6.6 \cdot 10^8$ m, the ratio between this perturbation and the main one has a value of about $8.0 \cdot 10^{-10}$, so it can be neglected for all the moons.

CENTRAL BODY'S RADIATION PRESSURE

For the central body's radiation pressure, the perturbing acceleration model is the same as for Jupiter and the Sun (see Equation (3.12)), but with the parameters now referred to the central body. It holds true that:

$$\vec{a}_{CBRP} = C_R \frac{W_{CB}\ A}{m\ c} \hat{r} \tag{3.15}$$

The ratio between this perturbing acceleration and the main one is proportional to the product of a constant and $\frac{R^2_{moon} \cdot T^4_{eq_{moon}}}{\mu}$. The equilibrium temperature of Ganymede is 130 K (page 731 of Spencer [1983]), while the others have not been found in literature, thus they have to be estimated. According to Stam [2016], it can be stated that the equilibrium temperatures of the other moons can be approximated as in Equation (3.16):

$$T_{eq_{moon}} = T_{eq_{Ganymede}} \sqrt{\frac{R_{Ganymede}}{R_{moon}}} \tag{3.16}$$

where R_{moon} indicates the radius of the moon under consideration.

By using Equation (3.16), Io has an equilibrium temperature of about 184 K, Europa of 169 K and Callisto of 136 K.

Thus, from the most interior to the most exterior moon, $\frac{R_{moon}^2 \cdot T_{eq_{moon}}^4}{\mu}$ has a value of roughly $6.4 \cdot 10^8\ \frac{\mathrm{K}^4 \cdot \mathrm{s}^2}{\mathrm{m}}$, $6.2 \cdot 10^8\ \frac{\mathrm{K}^4 \cdot \mathrm{s}^2}{\mathrm{m}}$, $2.0 \cdot 10^8\ \frac{\mathrm{K}^4 \cdot \mathrm{s}^2}{\mathrm{m}}$ and $2.8 \cdot 10^8\ \frac{\mathrm{K}^4 \cdot \mathrm{s}^2}{\mathrm{m}}$ respectively. It can then be assessed that Io (independently from the altitude) is the worst-case scenario. Then, by considering Io as central body, the equilibrium temperature is about 184 K, while its radius is about $1.822 \cdot 10^6$ m (Horizons interface), thus the ratio between this perturbation and the main acceleration is always about $6.7 \cdot 10^{-9}$ (this is roughly constant since the ratio does not depend on the altitude from the central body's surface). Due to its low value, also this perturbation can be neglected for all the moons in this analysis.

3.6.4. ELECTROMAGNETIC PERTURBATION

JOVIAN ELECTROMAGNETIC PERTURBATION

If the satellite is made of conductive material, it will interact with the magnetic field around it by means of the Lorentz force. According to page 547 of Wakker [2015], the perturbing acceleration caused by this phenomenon is described by Equation (3.17):

$$\vec{a}_{EM} = \frac{q}{m} \vec{v} x \vec{B} \tag{3.17}$$

where q indicates the satellite's electric charge, m its mass, v its velocity relative to the magnetic field, and B the magnetic field itself.

In particular, still according to the same page, q can be written as the product of the electrical potential difference U^* and the satellite's capacitance C. By using the approximations of a spherical conducting satellite, Equation (3.18) can be written (page 548 of Wakker [2015]):

$$C = 4\pi\epsilon_0 R_{S/C} \tag{3.18}$$

where ϵ_0 is the permittivity of free space $\left(8.854 \cdot 10^{-12} \frac{\mathrm{F}}{\mathrm{m}}\right)$, while $R_{S/C}$ is the radius of a satellite approximated (only for this purpose) as spherical.

According to page 547 of Wakker [2015], Equation (3.19) can be written:

$$\vec{B} = g_{1,0} \left(\frac{R}{r}\right)^3 \begin{pmatrix} 2sin(\phi) \\ -cos(\phi) \\ 0 \end{pmatrix} \begin{pmatrix} \hat{r} \\ \hat{\phi} \\ \hat{\lambda} \end{pmatrix} \tag{3.19}$$

where $g_{1,0}$ is the Gauss geomagnetic coefficients of degree 1 and order 0, R the celestial body's radius, r the distance between its center of mass and the satellite's one, while ϕ indicates the latitude of the spacecraft. Note also that $\hat{r}, \hat{\phi}, \hat{\lambda}$ represent the unit vectors in the radial (outwards), latitudinal (northwards) and longitudinal (but westwards) directions.

The following data can be used: $U^* \approx 100$ V (page 548 of Wakker [2015]), $m \approx 2223$ kg (Horizons interface), $R_{S/C} \approx 1$ m (realistic assumption based on NASA [2016a]), $R \approx 6.9911 \cdot 10^7$ m (Horizons interface) and $g_{1,0} = 100$ nT (page 292 of Bagenal et al. [2006]).

It can be assessed that the maximum ratio between this perturbation and the main acceleration is at the limit of the Galilean moons' spheres of influence, where the distance of the spacecraft from their centers of mass is maximum and where the one from Jupiter is minimum.

The worst case happens when the velocity and the magnetic field vectors are perpendicular and where $\phi = \pm 90°$ (since the magnetic field has its maximum magnitude).

Based on the information on the Horizons interface, the value of v is equal to 7.0 km/s at Io's sphere of influence, 18.5 km/s at Europa's, 14.6 km/s at Ganymede's and finally 10.4 km/s for Callisto's sphere of influence.

By using these values, it can be calculated that the ratios of the accelerations are respectively $3.5 \cdot 10^{-16}$ for Io, $6.5 \cdot 10^{-16}$ for Europa, $2.6 \cdot 10^{-16}$ for Ganymede and $1.1 \cdot 10^{-16}$ for Callisto.

JOVIAN INDUCED ELECTROMAGNETIC PERTURBATION ON THE MOONS

Note that this perturbation is related to the electromagnetic field centered in the moon but induced by Jupiter, while the previous one was centered in Jupiter itself. According to page 78 of Showman and Malhotra [1999], for induced magnetic fields, $g_{1,0}$ shall be considered as the ambient Jovian magnetic field, which has a value of 1835 nT at Io, 420 nT for Europa, 120 nT for Ganymede and 35 nT for Callisto.

By using these values and the values of the moons' radii as R, it can be assessed that the the ratio of the accelerations is proportional to $\frac{v \cdot g_{1,0}}{\mu \cdot r}$ (where r is the distance between the spacecraft and the center of mass of the central body), thus it is maximum at the closest approach. Always from the Horizons interface, the value of v is equal to 8.9 km/s at the Io's closest approach, 6.3 km/s at the Europa's one, 8.0 km/s at the Ganymede's one and finally 9.7 km/s for the Callisto's one. By using the altitudes described in Subsection 3.6.2, it can thus be computed that the ratio of the accelerations is respectively equal to $1.1 \cdot 10^{-12}$, $1.6 \cdot 10^{-12}$, $7.9 \cdot 10^{-13}$ and $6.1 \cdot 10^{-13}$ for the Galilean moons, from the most interior to the most exterior. They are so low that the magnetic field induced by Jupiter can be definitely neglected for all the moons in this analysis.

CENTRAL BODY'S ELECTROMAGNETIC PERTURBATION

This perturbation is related to the electromagnetic field possessed by the central body (thus centered in it) and not to that induced by Jupiter. According to page 78 of Showman and Malhotra [1999], $g_{1,0}$ is roughly 1300 nT for Io, 750 nT for Ganymede and 0 nT for Europa and Callisto, since they do not have an own magnetic field, but only the one induced by Jupiter, just described.

The ratio of the accelerations is again proportional to $\frac{v \cdot g_{1,0}}{\mu \cdot r}$, thus it is maximum at closest approach. So, by using the values for v and r just presented, the ratio between this perturbation and the central acceleration is equal to $7.9 \cdot 10^{-13}$ for Io and $5.0 \cdot 10^{-12}$ for Ganymede. Since they are almost irrelevant, the Galilean moons' own magnetic fields can be neglected.

3.6.5. NON-SYMMETRIC MASS DISTRIBUTION

According to page 527 of Wakker [2015], if we assume the presence of a static external potential and negligible effects of solid-Earth, ocean and pole tides, then the gravitational potential of a body at a point outside it can be described as a sum of spherical harmonics terms. In particular, from page 543 of Vallado and McClain [2007], it can be written as in Equation (3.20):

$$U = \frac{\mu}{r}\left[1 - \sum_{n=2}^{\infty} J_n \left(\frac{R}{r}\right)^n P_n(sin\phi) + \sum_{n=2}^{\infty}\sum_{m=1}^{n}\left(\frac{R}{r}\right)^n P_{n,m}(sin\phi)\big(C_{n,m}cos(m\lambda) + S_{n,m}sin(m\lambda)\big)\right] \tag{3.20}$$

where R is the equatorial radius of the celestial body, r the distance of the satellite from the body's center, ϕ the latitude, λ the longitude. Furthermore, $C_{n,m}$ and $S_{n,m}$ are model parameters of degree n and order m. Note that $J_n = J_{n,0} = -C_{n,0}$, since $S_{n,0} = 0$. In particular, $P_n(sin\phi)$ $\big(= P_{n,0}(sin\phi)\big)$ are the so-called Legendre polynomials of degree n and argument $sin\phi$, while $P_{n,m}(sin\phi)$ are the associated Legendre functions of the first kind of degree n, order m and argument $sin\phi$. A table for their main expressions can be found at page 541 of Vallado and McClain [2007].

Always according to page 548 of Vallado and McClain [2007], the perturbing acceleration due to the radially non-symmetric mass distribution is given by Equation (3.21):

$$\vec{a}_{MD} = \vec{\nabla}U^* = \vec{\nabla}\left(U - \frac{\mu}{r}\right) = \begin{pmatrix} \left(\frac{1}{r}\frac{\partial U}{\partial r} - \frac{r_z}{r^2\sqrt{r_x^2+r_y^2}}\frac{\partial U}{\partial \phi}\right) r_x - \frac{1}{r_x^2+r_y^2}\frac{\partial U}{\partial \lambda} r_y \\ \left(\frac{1}{r}\frac{\partial U}{\partial r} - \frac{r_z}{r^2\sqrt{r_x^2+r_y^2}}\frac{\partial U}{\partial \phi}\right) r_y + \frac{1}{r_x^2+r_y^2}\frac{\partial U}{\partial \lambda} r_x \\ \frac{1}{r}\frac{\partial U}{\partial r} r_z + \frac{\sqrt{r_x^2+r_y^2}}{r^2}\frac{\partial U}{\partial \phi} \end{pmatrix} \begin{pmatrix} \hat{i}_{PCPF} \\ \hat{j}_{PCPF} \\ \hat{k}_{PCPF} \end{pmatrix} \tag{3.21}$$

where r_x, r_y, r_z indicate the components of the acceleration in the directions of the PCPF-axes, and where Equation (3.22) holds true:

$$\begin{cases} \frac{\partial U^*}{\partial r} = -\frac{\mu}{r^2}\sum_{n=2}^{\infty}\sum_{m=0}^{n}\left(\frac{R}{r}\right)^n (n+1)P_{n,m}(sin\phi)\big(C_{n,m}cos(m\lambda) + S_{n,m}sin(m\lambda)\big) \\ \frac{\partial U^*}{\partial \phi} = \frac{\mu}{r}\sum_{n=2}^{\infty}\sum_{m=0}^{n}\left(\frac{R}{r}\right)^n \big(P_{n,m+1}(sin\phi) - m\cdot tan(\phi)P_{n,m}(sin\phi)\big)\big(C_{n,m}cos(m\lambda) + S_{n,m}sin(m\lambda)\big) \\ \frac{\partial U^*}{\partial \lambda} = \frac{\mu}{r}\sum_{n=2}^{\infty}\sum_{m=0}^{n}\left(\frac{R}{r}\right)^n mP_{n,m}(sin\phi)\big(S_{n,m}cos(m\lambda) - C_{n,m}sin(m\lambda)\big) \end{cases} \tag{3.22}$$

Note that Equation (3.21) is written in the PCPF reference frame, so the state has to be transformed from J2000 to PCPF to allow this, by means of the transformation presented in Appendix A. After having computed the accelerations in the PCPF frame, they have been transformed back to the J2000 frame, by means of the transformation presented in Appendix A.

Also these equations are written in the PCPF-frame, so the transformations described in Appendix A have been used.

Due to the fact that the zonal harmonics (m=0) do not have any dependency on longitude, while the tesseral ($m\neq$0) do, they will be treated separately. This allows to have an easier formulation for the zonal ones, which are usually more relevant than the others.

In Appendix C, it is proven that the perturbing acceleration acting on the spacecraft due to a zonal harmonic of degree n is maximum at the poles and does not depend on the longitude. The external perturbation due to Jupiter is the difference between the direct and the indirect term, and it is described by Equation (3.23):

$$\begin{aligned} a_{MD_{zonal_{max}}} &= \left(a_{MD_{zonal\ direct}} - a_{MD_{zonal\ indirect}}\right)_{max} = (n+1)\frac{\mu_{PB}R_{PB}^n}{r_{S/C-PB}^{n+2}}|J_n| - (n+1)\frac{\mu_{PB}R_{PB}^n}{r_{PB-CB}^{n+2}}|J_n| = \\ &= (n+1)\mu_{PB}R_{PB}^n\left(\frac{1}{r_{S/C-PB}^{n+2}} - \frac{1}{r_{PB-CB}^{n+2}}\right)|J_n| \end{aligned} \tag{3.23}$$

where μ_{PB} and R_{PB} indicates the gravitational parameter and the radius of the perturbing body, while $r_{S/C-PB}$ represents the distance between that celestial body and the spacecraft, and r_{PB-CB} the one between the former and the central body.

In general, the maximum ratio between this perturbation and the central acceleration has the form presented in Equation (3.24):

$$\left(\frac{a_{MD_{zonal}}}{a_{MAIN}}\right)_{max} = (n+1)\frac{\mu_{PB}}{\mu_{CB}}R_{PB}^n r^2\left(\frac{1}{r_{S/C-PB}^{n+2}} - \frac{1}{r_{PB-CB}^{n+2}}\right)|J_n| \tag{3.24}$$

Note that, in case the body whose zonal harmonics are being used is the central body, the indirect term does not exist and this ratio simplifies into Equation (3.25):

$$\left(\frac{a_{MD_{zonal}}}{a_{MAIN}}\right)_{max} = (n+1)\left(\frac{R}{r}\right)^n|J_n| \tag{3.25}$$

In Appendix D, it is shown instead that the perturbing acceleration due to a tesseral harmonic of degree n and order $m\neq0$ is maximum at a specific longitude (referred to as $\lambda_{a_{max}}$) and at a specific latitude (represented by $\phi_{a_{max}}$, which is the root of the nonlinear function presented in Appendix D, in Equation (D.6)). After having defined $|J_{n,m}| = \sqrt{C_{n,m}^2 + S_{n,m}^2}$, the expression of this external perturbation is presented in Equation (3.26):

$$\begin{aligned} &a_{MD_{tesseral_{max}}} = \left(a_{MD_{tesseral\ direct}} - a_{MD_{tesseral\ indirect}}\right)_{max} = \\ &\sqrt{\left((n+1)P_{n,m}\right)^2 + \left(P_{n,m+1} - m\cdot tan\phi_{a_{max}}\cdot P_{n,m}\right)^2}\,\mu_{PB}R_{PB}^n\left(\frac{1}{r_{S/C-PB}^{n+2}} - \frac{1}{r_{PB-CB}^{n+2}}\right)|J_{n,m}| \end{aligned} \tag{3.26}$$

where $P_{n,m}$ indicates $P_{n,m}(sin\phi_{a_{max}})$. Note that in Equation (3.26), there is no term $\lambda_{a_{max}}$, because the value of $a_{MD_{tesseral_{max}}}$ does not explicitly depend on the value of $\lambda_{a_{max}}$, however, a generic $a_{MD_{tesseral}}$ does depend on the value of the longitude λ.

Notice that m shall always be less than or equal to n, thus Equation (3.26) cannot be used when m=n, due to the presence of $P_{n,m+1}$. According to Wikipedia [2017b], it can be solved by using Equation (3.27):

$$P_{n,m+1}(sin\phi) = \frac{(n-m+1)}{cos\phi} P_{n+1,m}(sin\phi) - (n+m+1)\tan\phi \cdot P_{n,m}(sin\phi) \tag{3.27}$$

The maximum ratio between the perturbation due to a tesseral harmonic and the central acceleration is described in Equation (3.28):

$$\left(\frac{a_{MD_{tesseral}}}{a_{MAIN}}\right)_{max} = \\ = \sqrt{\left((n+1)P_{n,m}\right)^2 + \left(P_{n,m+1} - m \cdot tan\phi_{a_{max}} \cdot P_{n,m}\right)^2} \frac{\mu_{PB}}{\mu_{CB}} R_{PB}^n r^2 \left(\frac{1}{r_{S/C-PB}^{n+2}} - \frac{1}{r_{PB-CB}^{n+2}}\right) |J_{n,m}| \tag{3.28}$$

Note that, if these tesseral harmonics refer to the central body, the indirect term does not exist and this ratio can be simplified and written as in Equation (3.29):

$$\left(\frac{a_{MD_{tesseral}}}{a_{MAIN}}\right)_{max} = \sqrt{\left((n+1)P_{n,m}\right)^2 + \left(P_{n,m+1} - m \cdot tan\phi_{a_{max}} \cdot P_{n,m}\right)^2} \left(\frac{R}{r}\right)^n |J_{n,m}| \tag{3.29}$$

Please note that if these spherical harmonics (either zonal or tesseral) refer to the central body, then the maximum ratio is reached at the minimum distance r from its center of mass, i.e. at the closest approach, otherwise at the limit of the sphere of influence, where r is maximum ($r = R_{s.o.i.}$) and $r_{S/C-PB}$ minimum ($r_{S/C-PB} = r_{PB-CB_{min}} - R_{s.o.i}$). It can be easily realized that, when the perturbing body is Jupiter, $r_{PB-CB_{min}}$ coincides with the pericenter of the central body's orbit about the gas giant.

The main effects of the spherical harmonics of both Jupiter and the central body will now be quantified depending on the flyby altitude and assessed as negligible or relevant.

JOVIAN NON-SYMMETRIC MASS DISTRIBUTION

If the spherical harmonics of Jupiter are considered, the ratio between the two accelerations is maximum at the limit of the sphere of influence (and with the central body at its perijove). Table 3.3 presents the values of this ratio for all the four possible central bodies:

Table 3.3: Values of spherical harmonics perturbing accelerations and accelerations ratio for Jupiter, computed at the radii of the spheres of influence specified in Table 3.1.

Galilean moon	**Jovian spherical harmonic**	**Jovian perturbing acceleration value** [m/s^2]	**Accelerations ratio**
Io	J_2	$7.2 \cdot 10^{-5}$	$7.4 \cdot 10^{-4}$
	J_3	$9.0 \cdot 10^{-10}$	$9.3 \cdot 10^{-9}$
	J_4	$2.1 \cdot 10^{-7}$	$2.2 \cdot 10^{-6}$
	J_6	$6.8 \cdot 10^{-10}$	$7.0 \cdot 10^{-9}$
	$J_{2,2}$	$4.5 \cdot 10^{-10}$	$4.6 \cdot 10^{-9}$
Europa	J_2	$8.9 \cdot 10^{-6}$	$2.6 \cdot 10^{-4}$
	J_3	$7.0 \cdot 10^{-11}$	$2.1 \cdot 10^{-9}$
	J_4	$1.0 \cdot 10^{-8}$	$3.1 \cdot 10^{-7}$
	J_6	$1.3 \cdot 10^{-11}$	$3.9 \cdot 10^{-10}$
	$J_{2,2}$	$5.6 \cdot 10^{-11}$	$1.6 \cdot 10^{-9}$
Ganymede	J_2	$2.1 \cdot 10^{-6}$	$1.3 \cdot 10^{-4}$
	J_3	$1.0 \cdot 10^{-11}$	$6.2 \cdot 10^{-10}$
	J_4	$9.6 \cdot 10^{-10}$	$5.8 \cdot 10^{-8}$
	J_6	$4.8 \cdot 10^{-13}$	$2.9 \cdot 10^{-11}$
	$J_{2,2}$	$1.3 \cdot 10^{-11}$	$7.9 \cdot 10^{-10}$
Callisto	J_2	$2.0 \cdot 10^{-7}$	$3.9 \cdot 10^{-5}$
	J_3	$5.6 \cdot 10^{-13}$	$1.1 \cdot 10^{-10}$
	J_4	$3.0 \cdot 10^{-11}$	$5.9 \cdot 10^{-9}$
	J_6	$4.8 \cdot 10^{-15}$	$9.5 \cdot 10^{-13}$
	$J_{2,2}$	$1.5 \cdot 10^{-12}$	$2.5 \cdot 10^{-10}$

The values for the Jovian zonal harmonics J_2, J_3, J_4 and J_6 have been found at NASA [2004], while the value for $J_{2,2}$ at page 370 of Campbell and Synnott [1985].

Obviously, the Jovian J_2 spherical harmonics will be considered, since it leads to non-negligible ratios with respect to the main acceleration. The effects of the other spherical harmonics appear very small. They have also been tested in preliminary orbit calculations and lead to changes in the root mean square error on position and velocity respectively smaller than $1 \cdot 10^{-3}$ m and $1 \cdot 10^{-6}$ m/s with respect to the JPL ephemerides, the observational data. Clearly they can be neglected.

Central body's non-symmetric mass distribution

According to page 282 of Bagenal et al. [2006], the value of $C_{2,2}$ is definitely higher than $S_{2,2}$ for all the Galilean moons, so that it can be written that $|J_{2,2}| \approx |C_{2,2}|$. Note that a value of $S_{2,2}$ has not been found for Io, thus it has been assumed, just for this purpose, that $|J_{2,2}| = |C_{2,2}|$, i.e. $|S_{2,2}| = 0$.

The values of Io's J_2, J_4 and $J_{2,2}$ have been taken from page 1382 of Zharkov and Gudkova [2010], while $J_{3,1}$, $J_{3,3}$, $J_{4,2}$ and $J_{4,4}$ from page 1387 of the same paper. The J_2, $J_{2,1}$ and $J_{2,2}$ values for Europa come from page 2020 of Anderson et al. [1998], while Callisto's ones from page 157 of Anderson et al. [2001]. Ganymede's J_2, J_3 and J_4, but also the tesseral $J_{2,1}$, $J_{2,2}$, $J_{3,1}$, $J_{3,2}$, $J_{3,3}$, $J_{4,1}$, $J_{4,2}$, $J_{4,3}$ and $J_{4,4}$ have been taken from page 434 of Russell and Brinckerhoff

[2009], while its J_5, J_6, J_7 and J_8 from page 11 of Parisi et al. [2012].

If the spherical harmonics of the central body are considered, then the ratio between the two accelerations is maximum at its closest approach. Table 3.4 presents the values of this ratio for all the four possible central bodies:

Table 3.4: Values of spherical harmonics perturbing accelerations and accelerations ratio for the central bodies, computed at their closest approaches, i.e. at an altitude of 102 km from Io's surface, 201 km from Europa's, 261 km from Ganymede's and 138 km from Callisto's according to the Horizons Web Interface.
* According to page 157 of Anderson et al. [2001], the nominal values of $C_{2,1}$ and $S_{2,1}$ of Callisto are estimated to be $0.0{\cdot}10^{-6}$, that is why a zero value for $J_{2,1}$ is present in this table.

Galilean moon	**Spherical harmonic**	**Central body's perturbing acceleration value** [m/s^2]	**Accelerations ratio**
Io	J_2	$8.1{\cdot}10^{-3}$	$5.0{\cdot}10^{-3}$
	J_4	$6.1{\cdot}10^{-5}$	$3.8{\cdot}10^{-5}$
	$J_{2,2}$	$7.3{\cdot}10^{-3}$	$4.5{\cdot}10^{-3}$
	$J_{3,1}$	$1.5{\cdot}10^{-5}$	$9.4{\cdot}10^{-6}$
	$J_{3,3}$	$1.7{\cdot}10^{-5}$	$1.0{\cdot}10^{-5}$
	$J_{4,2}$	$5.5{\cdot}10^{-5}$	$3.4{\cdot}10^{-5}$
	$J_{4,4}$	$2.8{\cdot}10^{-5}$	$1.7{\cdot}10^{-5}$
Europa	J_2	$1.1{\cdot}10^{-3}$	$1.0{\cdot}10^{-3}$
	$J_{2,1}$	$5.5{\cdot}10^{-5}$	$5.3{\cdot}10^{-5}$
	$J_{2,2}$	$9.6{\cdot}10^{-4}$	$9.3{\cdot}10^{-4}$
Ganymede	J_2	$3.9{\cdot}10^{-4}$	$3.3{\cdot}10^{-4}$
	J_3	$3.7{\cdot}10^{-6}$	$3.1{\cdot}10^{-6}$
	J_4	$2.0{\cdot}10^{-5}$	$1.7{\cdot}10^{-5}$
	J_5	$1.0{\cdot}10^{-5}$	$8.6{\cdot}10^{-6}$
	J_6	$8.3{\cdot}10^{-6}$	$7.1{\cdot}10^{-6}$
	J_7	$4.0{\cdot}10^{-6}$	$3.4{\cdot}10^{-6}$
	J_8	$4.4{\cdot}10^{-6}$	$3.7{\cdot}10^{-6}$
	$J_{2,1}$	$7.2{\cdot}10^{-6}$	$6.1{\cdot}10^{-6}$
	$J_{2,2}$	$3.5{\cdot}10^{-4}$	$3.0{\cdot}10^{-4}$
	$J_{3,1}$	$7.9{\cdot}10^{-5}$	$6.7{\cdot}10^{-5}$
	$J_{3,2}$	$9.0{\cdot}10^{-5}$	$7.6{\cdot}10^{-5}$
	$J_{3,3}$	$5.6{\cdot}10^{-5}$	$4.8{\cdot}10^{-5}$
	$J_{4,1}$	$7.9{\cdot}10^{-5}$	$6.7{\cdot}10^{-5}$
	$J_{4,2}$	$7.5{\cdot}10^{-5}$	$6.3{\cdot}10^{-5}$
	$J_{4,3}$	$3.7{\cdot}10^{-5}$	$3.2{\cdot}10^{-5}$
	$J_{4,4}$	$5.1{\cdot}10^{-5}$	$4.3{\cdot}10^{-5}$
Callisto	J_2	$9.7{\cdot}10^{-5}$	$8.8{\cdot}10^{-5}$
	$J_{2,1}$	0^*	0^*
	$J_{2,2}$	$9.1{\cdot}10^{-5}$	$8.3{\cdot}10^{-5}$

Respecting the results in Table 3.4, all the available central body's spherical harmonics will be considered, since they lead to non-negligible ratios with respect to the main acceleration.

3.6.6. RELATIVISTIC EFFECTS

The equation of motion of the two-body problem, presented as Equation (3.1), considers the speed of light as infinite.

However, there is a perturbing acceleration due to relativistic effects, i.e. the consideration of the finiteness of the light speed according to Einstein's theory of general relativity, which is described by Equation (3.30) (page 121 of Dallas [1977]):

$$\vec{a}_{REL} = \frac{\mu}{r^2 c^2}\left(3v^2 + \sum_{k\neq CB}\frac{\mu_k}{r_k} + 4\sum_{k\neq S/C}\frac{\mu_k}{r_{S/C-k}}\right)\hat{r} \tag{3.30}$$

where μ is the gravitational parameter of the central body, μ_k that of the third body, c the light speed, v the velocity of the spacecraft with respect to the central body, r_k the distance between the third and the central body, while $r_{S/C-k}$ the distance between the spacecraft and the third body. Note also that the subscript CB indicates the central body and S/C the spacecraft.

The maximum ratio of this perturbation with respect to the main gravitational acceleration can be then written as in Equation (3.31):

$$\left(\frac{a_{REL}}{a_{MAIN}}\right)_{max} = \frac{1}{c^2}\left(3v^2 + \sum_{k\neq CB}\frac{\mu_k}{r_k} + 4\sum_{k\neq S/C}\frac{\mu_k}{r_{S/C-k}}\right)_{max} \tag{3.31}$$

It has the highest values at the closest approache, where v is maximum. Note that by considering, for each moon, Jupiter, the Sun, the central body itself and the other three Galilean moons in Equation (3.31), which are the most important bodies for this perturbation, the ratio with respect to the main gravitational acceleration is about $2.9{\cdot}10^{-7}$ for Io, $2.1{\cdot}10^{-7}$ for Europa, $1.8{\cdot}10^{-7}$ for Ganymede and $1.7 \cdot 10^{-7}$ for Callisto.

Due to the small values of these ratios, the relativistic effects will not be taken into account.

3.7. SYNOPSIS: PERTURBATIONS RELEVANCE

Third-body perturbations due to the Sun, Jupiter and the three Galilean moons different from the central body will be considered, as well the non-symmetric mass distribution effects of Jupiter in terms of J_2, and of the central body by means of all the available spherical harmonics, because all these lead to a relatively high perturbation with respect to the main gravitational acceleration.

4
Integration

In this chapter, the choice of the integration technique will be treated, along with the discussion of local and global truncation errors.

4.1. Integration type

Although it does not give insight in the solution, numerical integration allows to have reliable and quick results, while analytical techniques do allow a deeper comprehension, but are not able to produce solutions as accurate as the ones obtained from numerical methods. This holds in particular in the situation when perturbations have to be included, as in the case here. For these reasons, a numerical integration will be used instead of an analytical one.

4.2. Integrator choice

Integrators and different kinds of coordinates will now be compared; the most suitable ones will be then used for the propagation of the state of the spacecraft.

4.2.1. Integrators comparison

Comparisons of the absolute error of position and velocity of all the built-in MATLAB integrators with respect to an extremely accurate higher-order and higher-tolerance Runge-Kutta-Fehlberg 7(8) are performed in modified equinoctial elements, since they are in general more stable for orbit propagation, according to page 50 of Jo et al. [2011a]. Since the choice of the integrator is quite relevant, it is preferred to compare them by using the most stable coordinates, and then Cartesian coordinates and modified equinoctial elements will be compared: if the latter show to perform better than the former, the first assumption was correct, otherwise a second integrators comparison will be performed, but in Cartesian coordinates. Computation times will be compared too. Due to the very long time the Runge-Kutta-Fehlberg 7(8) method needs to propagate, it is excluded from the candidates and used just as reference for comparing all the others. Note that the R2016b version of the MATLAB software will be used for this project.

The chosen scenario relates to the propagation of the Galileo spacecraft from entering to leaving the sphere of influence of Ganymede with respect to Jupiter, because this is a good representation of the possible scenarios which will be analyzed later. The starting date is June 27, 1996 at 04:44:06.5 UTC and the propagation lasts for 3.5 hours, which is a good approximation of the Galileo's flybys duration in general.

The output time-step is equal to 60 seconds. The relative tolerance of the MATLAB integrators used for these comparisons is the best allowed by the MATLAB software, i.e. $100 \cdot 2^{-52}$ ($\approx 2 \cdot 10^{-14}$), while the relative tolerance allowed for RKF7(8) is $1 \cdot 10^{-20}$, since it has been implemented independently. Furthermore, RKF7(8) is a variable-order method where the maximum order involved is 8, while the standard MATLAB integrators can reach a maximum order equal to 5 (with the exception of ODE113 which can automatically vary the order from 1 up to 13). This proves the superiority of RKF7(8), which however does not lead to a much different final state, but the computation time is much higher than in the other cases.

In particular, the propagation has been done considering third-body perturbations, in order to avoid relevant errors in state, due to the fact that this is an important perturbation.

Figures 4.1 and 4.2 respectively show a plot for the absolute position error of the compared integrators with regard to the RKF7(8) one and a zoom of it. Figures 4.3 and 4.4 indicate the same, but for velocity. Finally, Figure 4.5 shows a comparison of all the computation times needed to perform the propagation.

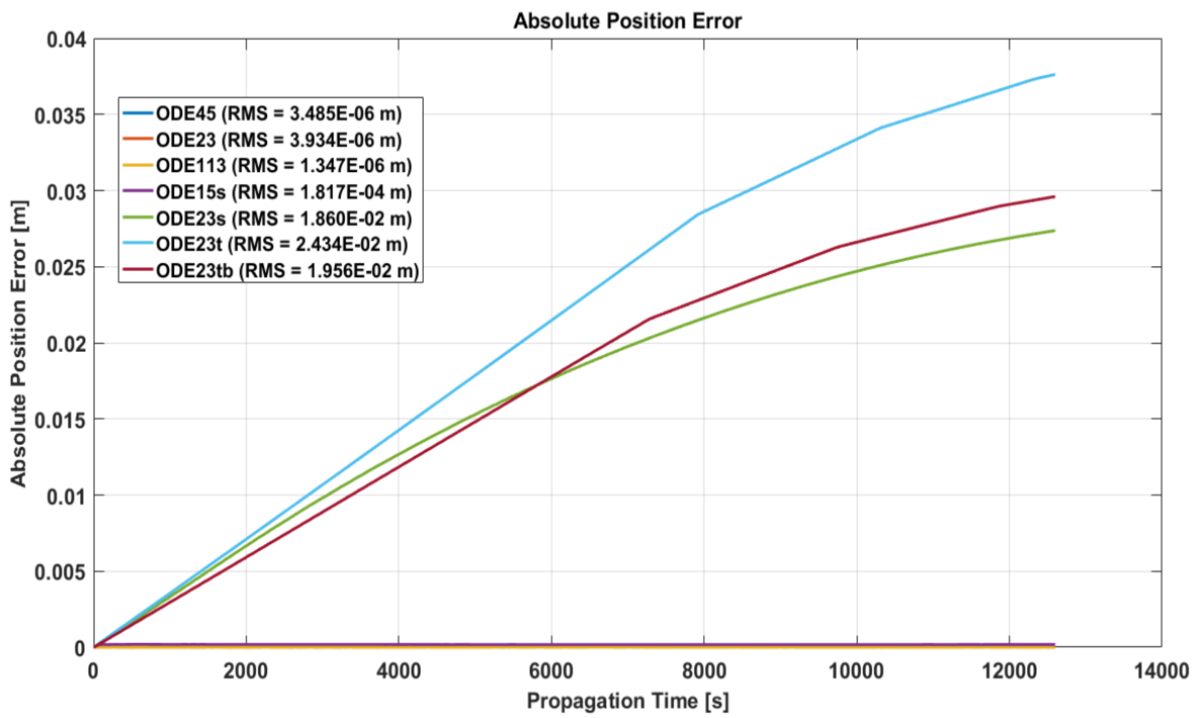

Figure 4.1: Absolute position error (with respect to RKF7(8)) comparison of all the MATLAB integrators.

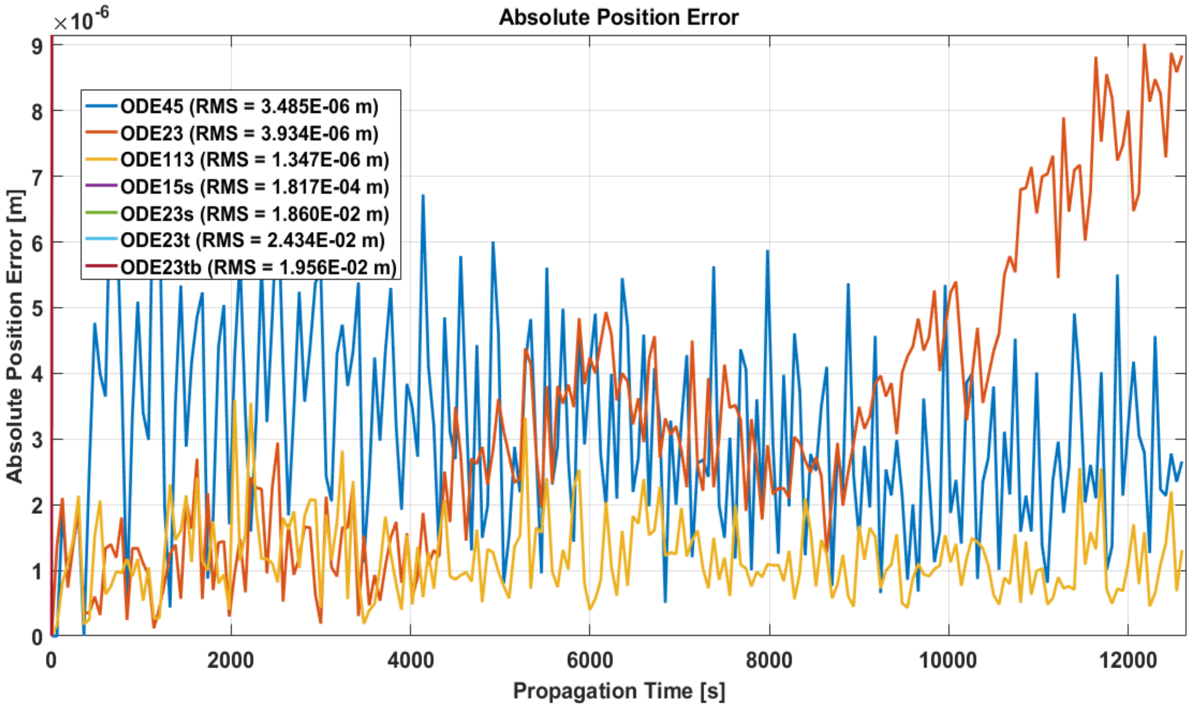

Figure 4.2: Zoom of the absolute position error (with respect to RKF7(8)) comparison of all the MATLAB integrators.

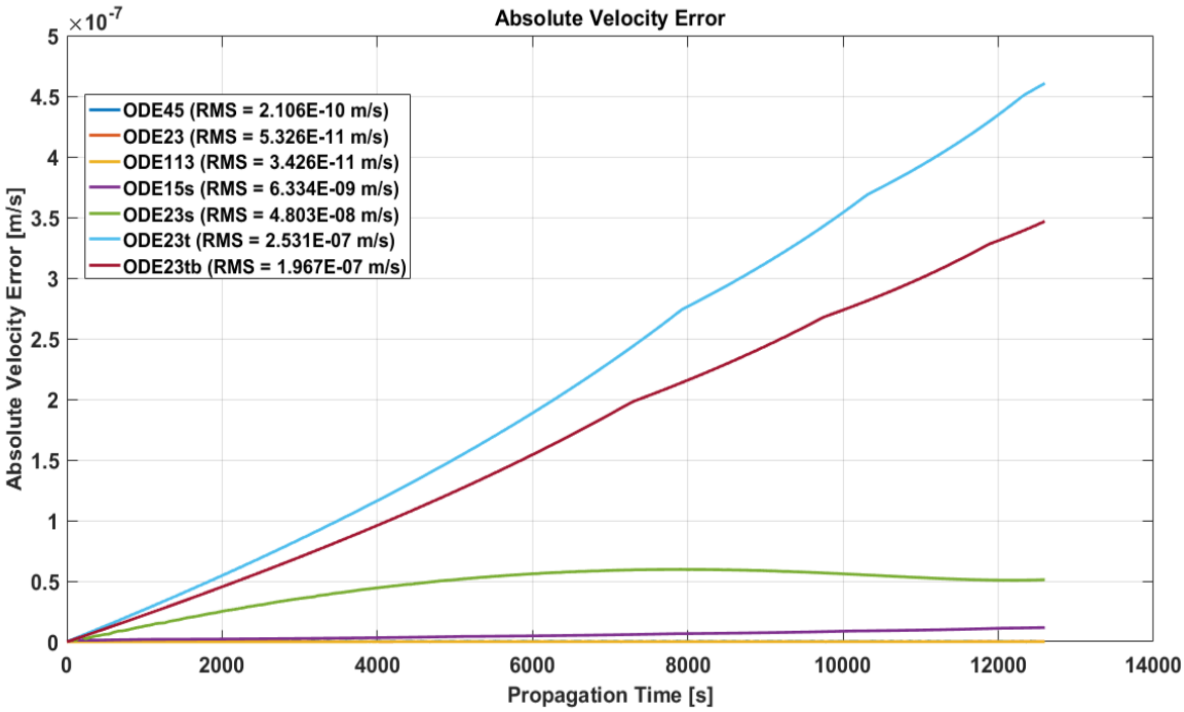

Figure 4.3: Absolute velocity error (with respect to RKF7(8)) comparison of all the MATLAB integrators.

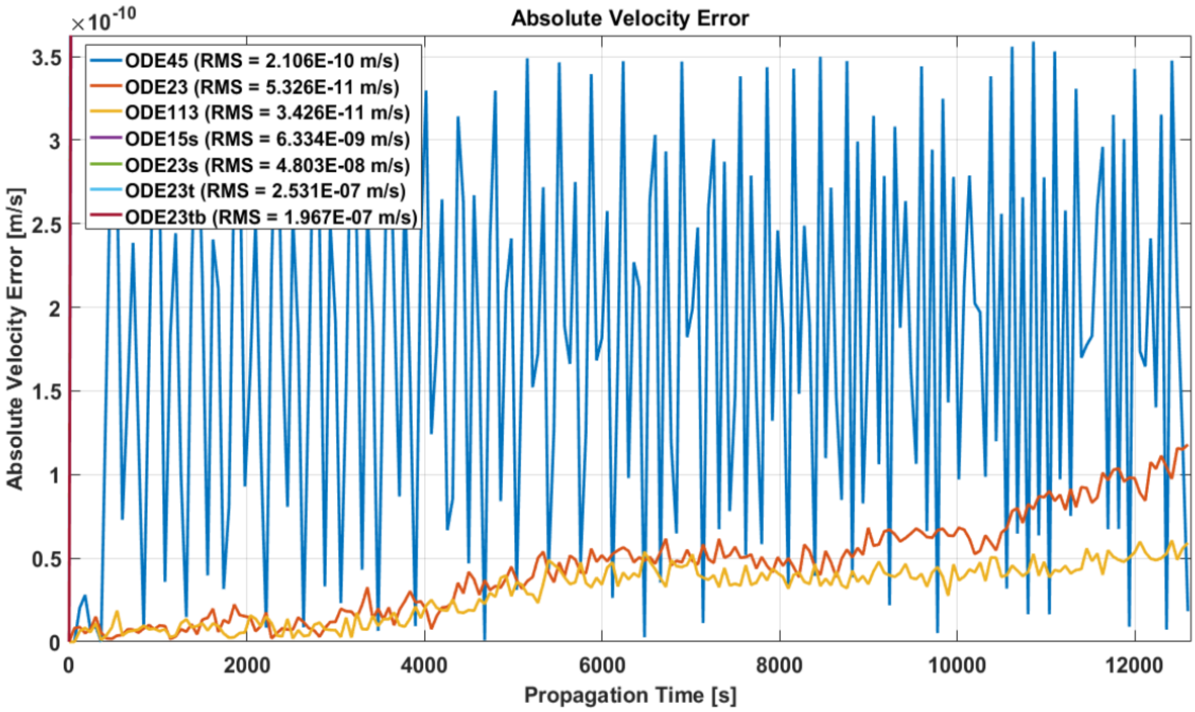

Figure 4.4: Zoom of the absolute velocity error (with respect to RKF7(8)) comparison of all the MATLAB integrators.

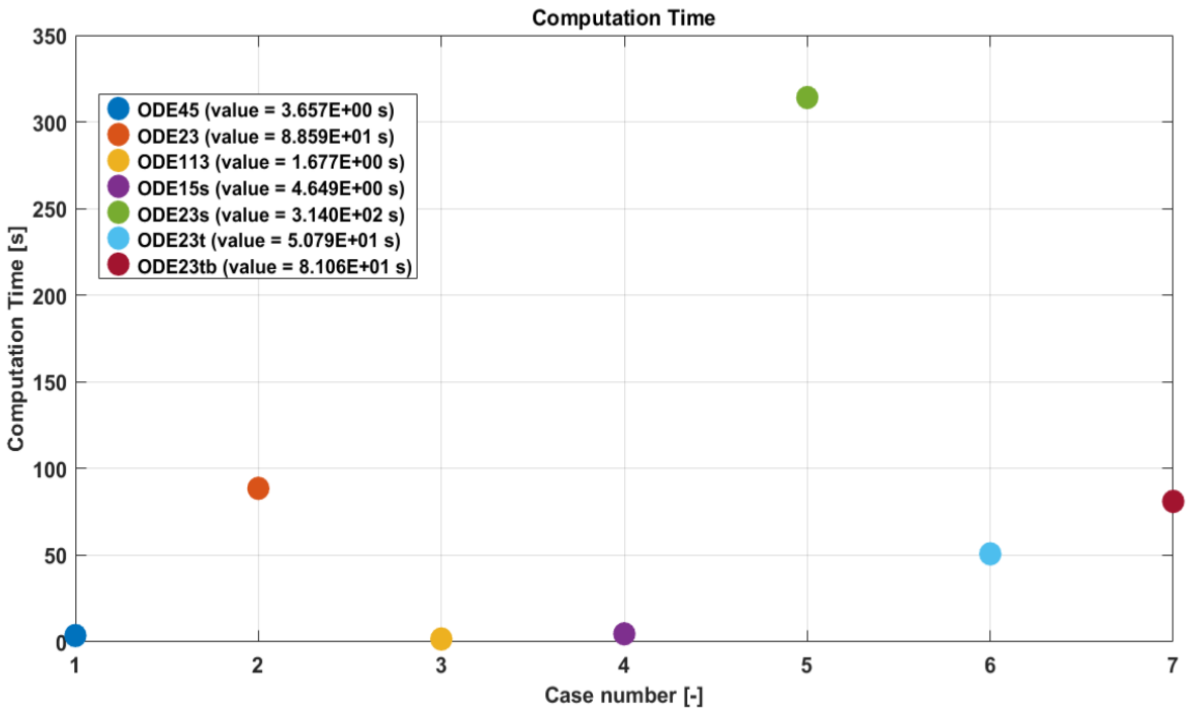

Figure 4.5: CPU time comparison of all the MATLAB integrators.

ODE113 is the single best for all the three variables, with a root mean square of absolute position error of $1.347{\cdot}10^{-6}$ m and of absolute velocity error of $3.426{\cdot}10^{-11}$ m/s, and a computation time of 1.677 s. This numerical integrator has indeed been designed for computational expensive ordinary differential equations. So, ODE113 will be the integrator used in this project.

4.2.2. COORDINATES COMPARISON

It can now be checked whether Cartesian coordinates or modified singular elements are more suitable for this kind of problem. Note that the output time-step has been reduced to 1 second to obtain more points which influence the root mean square error.

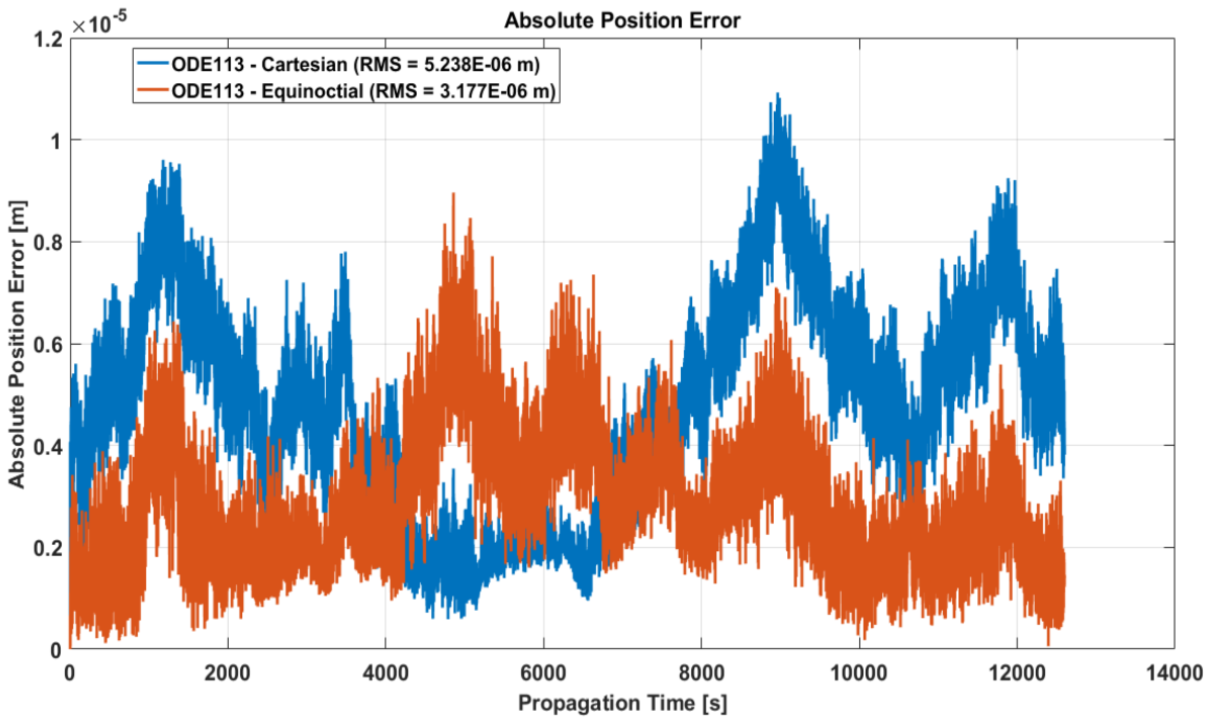

Figure 4.6: Position absolute error (with respect to Runge-Kutta-Fehlberg 7(8)) comparison between ODE113 in Cartesian coordinates and modified equinoctial elements.

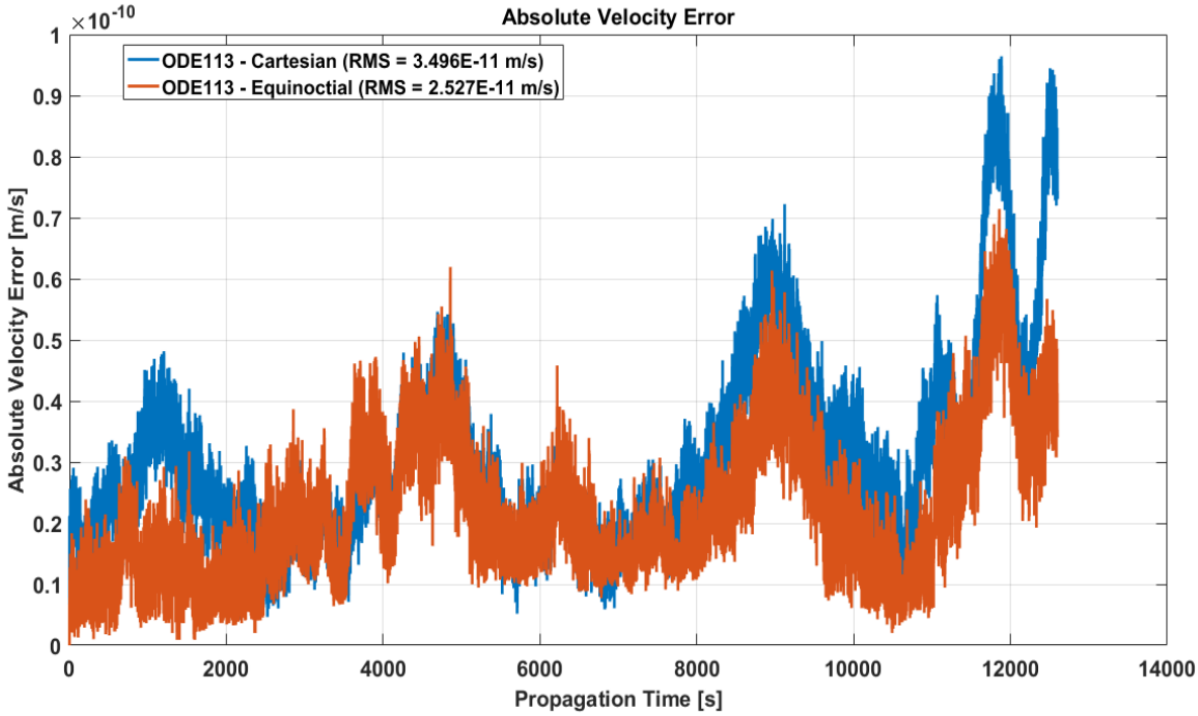

Figure 4.7: Velocity absolute error (with respect to Runge-Kutta-Fehlberg 7(8)) comparison between ODE113 in Cartesian coordinates and modified equinoctial elements.

Table 4.1 shows the CPU time of ODE113 in Cartesian coordinates and in modified equinoctial elements:

Table 4.1: CPU time comparison between ODE113 in Cartesian coordinates and modified equinoctial elements.

Coordinates	**CPU Time [s]**
Cartesian	1.823
Equinoctial	1.751

In Figures 4.6 and 4.7, as well as in Table 4.1, modified equinoctial elements proved to behave better than Cartesian coordinates, hence they will be used. In particular they have reported to lead to a root mean square of absolute position error of about $3.177 \cdot 10^{-6}$ m and of absolute velocity error of roughly $2.527 \cdot 10^{-11}$ m/s, and a computation time of 1.751 s. Hence, there is no reason to compare the integrators by using the Cartesian coordinates.

4.3. Expressions for the chosen integrator

The selected ODE113 integrator implements an Adams-Bashforth-Moulton (ABM) PECE method. The description which follows is taken after Ashino et al. [2000]. A linear multistep method with k steps can be expressed as in Equation (4.1):

$$\sum_{j=0}^{k} \alpha_j y_{n+j-k+1} = h \sum_{j=0}^{k} \beta_j f_{n+j-k+1} \tag{4.1}$$

where f indicates the derivative function, h the step-size, while α_j and β_j are constants.

There exists the Adams-Bashforth (AB) integrator which is the explicit version ($b_k = 0$) of the linear multistep method described above and it is defined by Equation (4.2):

$$y_{n+1} - y_n = h \sum_{j=0}^{k-1} \beta_j^* f_{n+j-k+1} \tag{4.2}$$

Another method, known as Adams-Moulton (AM), allows for an implicit ($b_k \neq 0$) propagation of the solution. It is described by Equation (4.3):

$$y_{n+1} - y_n = h \sum_{j=0}^{k} \beta_j f_{n+j-k+1} \tag{4.3}$$

This AB method is used to predict y_{n+1}^* of the following step. By inserting in Equation (4.3) the evaluation of the function at the point (x_{n+1}, y_{n+1}^*), a corrected value of y_{n+1} is obtained. As a last step, the function is evaluated at (x_{n+1}, y_{n+1}) to get the desired value.

This is the so-called ABM method, because it is a combination of the two; furthermore the acronym PECE stands for the four phases to be performed: Predict-Evaluate-Correct-Evaluate. According to page 7 of Xu [2015], the local truncation error for a k-step explicit step is proportional to h^k, and to h^{k+1} for a k-step implicit step. According to page 50 of Demanet [2014], if the local truncation error of a convergent stable multistep method with order p is proportional to h^{p+1}, then the global truncation error is proportional to h^p. In particular, when predictor and corrector have the same order, the local truncation error is well described by the Milne estimation, given by Equation (4.4):

$$\epsilon_{n+1} \approx \frac{C_{p+1}}{C_{p+1}^* - C_{p+1}} (y_{n+1} - y_{n+1}^*) \tag{4.4}$$

where C_{p+1}^* and C_{p+1} are respectively the error constants (they vary only when the number of steps k varies) of the AB and AM methods.

4.4. SYNOPSIS: INTEGRATOR

The ABM PECE-based MATLAB built-in integrator ODE113 in modified equinoctial elements will be the propagator used in this project, since it showed its advantages in terms state error and computation time with respect to all the other options.

5

Selection test cases and tuning integrator

In this chapter, a selection of the test cases endowed with the most precise observations will be provided. The accuracy of the observations mainly depends on the elevation angle of the Earth, i.e. the angle under which the Earth is seen from the spacecraft's orbital plane.

5.1. Orbit geometry

Unfortunately, there has been no other spacecraft which entered the Galilean moons' spheres of influence but Galileo. However, it entered and left them many times (Muller [2006]), so its flybys about these moons will be analyzed.

It is desired to have two flybys per Galilean moon, both with good elevation angles of the Earth, but one at low altitude and the other at high altitude. In particular the former is supposed to be less precise than the latter, since inaccuracies in the gravity model of the central body and other effects have greater influence at low altitudes. Furthermore, it shall also be noticed that in general a high-altitude flyby indicates a shorter duration of the flyby itself inside the sphere of influence of the central body, i.e. there is less time for dynamical errors to develop.

The spacecraft data are obtained by means of observations which use the concept of Doppler effect. In order to obtain a good reliability of the data, a constraint on the maximum absolute value of the Earth's elevation angle shall be put. For this analysis, it has been chosen to be 20°, since it is not too low, while still leading to an acceptable accuracy of the values of the spacecraft's state. Values higher than 20° would lead to a very low variation of the spacecraft's distance from Earth, thus the acquisition data made through Doppler effect analyses would be not accurate enough.

A summary of the flybys performed by the Galileo spacecraft is presented in Table 5.1.

Table 5.1: Summary of the flybys performed by Galileo about the Galilean moons. Rows with red background indicate that they would have been a good choice but the constraint on the Earth's elevation angle is not fulfilled. Rows with green background indicate the chosen flybys.

IO				
Flyby ID	Date	UTC Time	Closest-approach altitude (km)	Elevation of Earth (deg)
I0	07/12/95	17:45:58.50	897	-7.1
I24	11/10/99	04:23:02.50	611	-1.4
I25	26/11/99	04:05:21.00	301	-31.5
I31	06/08/01	04:59:20.50	194	-34.1
I32	16/10/01	01:23:21.00	184	51.4
I33	17/01/02	14:08:28.50	102	15.9

GANYMEDE				
Flyby ID	Date	UTC Time	Closest-approach altitude (km)	Elevation of Earth (deg)
G1	27/06/96	06:29:06.50	835	9.3
G2	06/09/96	18:59:34.00	261	19.8
G7	05/04/97	07:09:58.50	3102	50.8
G8	07/05/97	15:56:09.50	1603	27.0
G28	20/05/00	10:10:10.00	809	-2.4
G29	28/12/00	08:25:27.00	2338	3.4

EUROPA				
Flyby ID	Date	UTC Time	Closest-approach altitude (km)	Elevation of Earth (deg)
E4	19/12/96	06:52:58.00	692	-2.0
E6	20/02/97	17:01:10.50	586	-11.2
E11	06/11/97	20:31:44.50	2043	20.5
E12	16/12/97	12:03:20.00	201	-9.2
E14	29/03/98	13:21:05.50	1644	10.4
E15	31/05/98	21:14:00.00	2515	13.0
E16	21/07/98	05:03:45.00	1834	-24.9
E17	26/09/98	03:54:20.00	3582	-43.7
E18	22/11/98	11:38:26.50	2271	38.6
E19	01/02/99	02:19:50.00	1439	32.4
E26	03/01/00	17:59:43.00	351	-31.7

CALLISTO				
Flyby ID	Date	UTC Time	Closest-approach altitude (km)	Elevation of Earth (deg)
C3	04/11/96	13:34:28.00	1136	10.2
C9	25/06/97	13:47:50.00	418	2.2
C10	17/09/97	00:18:55.00	535	4.5
C20	05/05/99	13:56:18.50	1321	5.0
C21	30/06/99	07:46:50.00	1048	-3.2
C22	14/08/99	08:30:52.00	2299	1.0
C23	16/09/99	17:27:02.00	1052	3.2
C30	25/05/01	11:23:58.00	138	3.3

The chosen flybys are I0, I33, E12, E15, G2, G29, C22 and C30, because they are the ones which guarantee the most extreme closest-approach altitudes and a good accuracy of the data due to the orbit geometry with respect to Earth.

As an example, Galileo's flyby of Callisto on August 14, 1999 is considered as a valid test case, since the orbit appears to be almost perfectly in the plane seen from Earth and furthermore its data are assumed to be precise, because the approaching and receding of the spacecraft perceived from Earth are fundamental in the computation of its state through the Doppler effect.

Figure 5.1 shows the Earth's elevation angle between the instantaneous orbital plane of Galileo and the line which connects the spacecraft to Earth as a function of time. Note that the nearer to 0° it is, the higher the accuracy of the observation is.

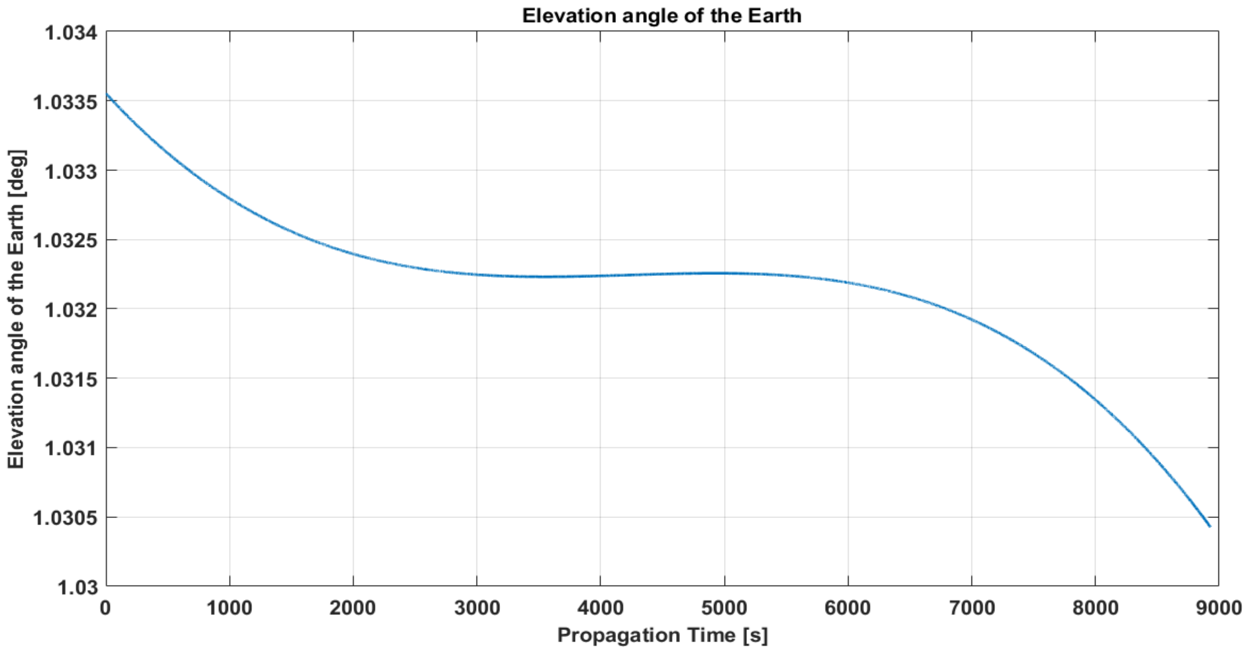

Figure 5.1: Earth's elevation angle as a function of simulation time, during the flyby of Callisto on August 14, 1999.

Since this angle is about 1° throughout the flyby, it can be concluded that the observations for the state of the spacecraft in this scenario are accurate.

Please notice this also by looking at Figure 5.2, where it can be seen that the trajectory followed by the spacecraft in a J2000 Earth-centered frame is almost planar and that the elevation angle of the Earth is almost 0°. The zero-value can be obtained only when the Earth remains in the orbital plane of the spacecraft throughout the entire flyby, so when this plane coincides with the ecliptic.

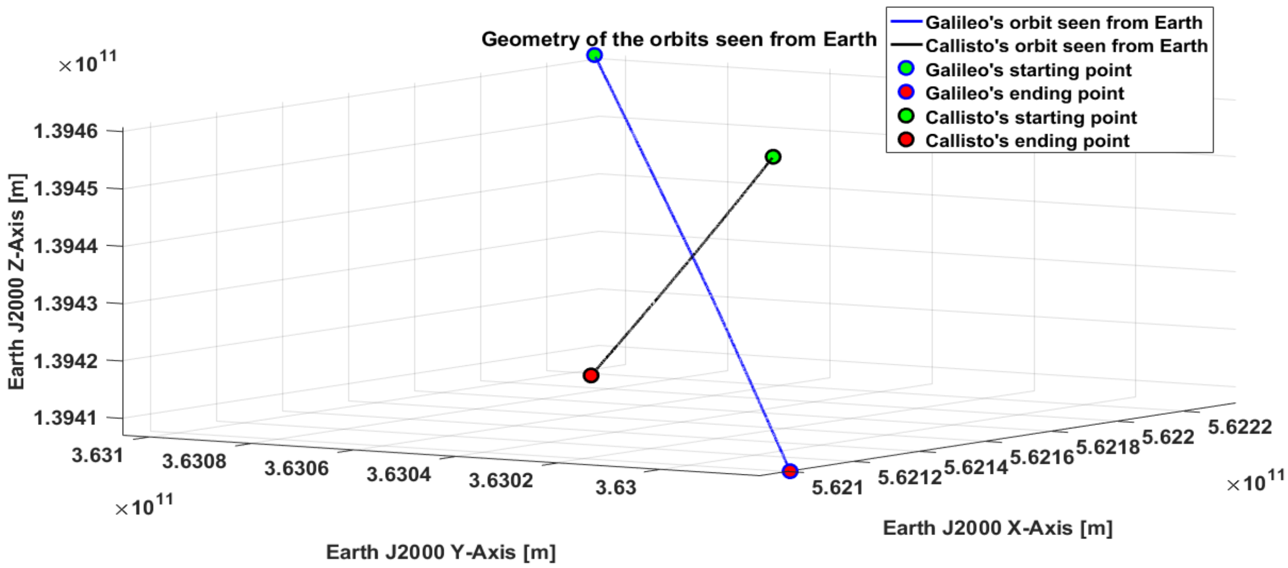

Figure 5.2: 3D representation of the flyby of Callisto on August 14, 1999 in a J2000 Earth-centered frame. For clarity, the trajectory followed by the central body is presented too.

Figure 5.3 shows instead Galileo's trajectory with respect to Callisto in the orbital plane, i.e. a hyperbola, deformed because of scale.

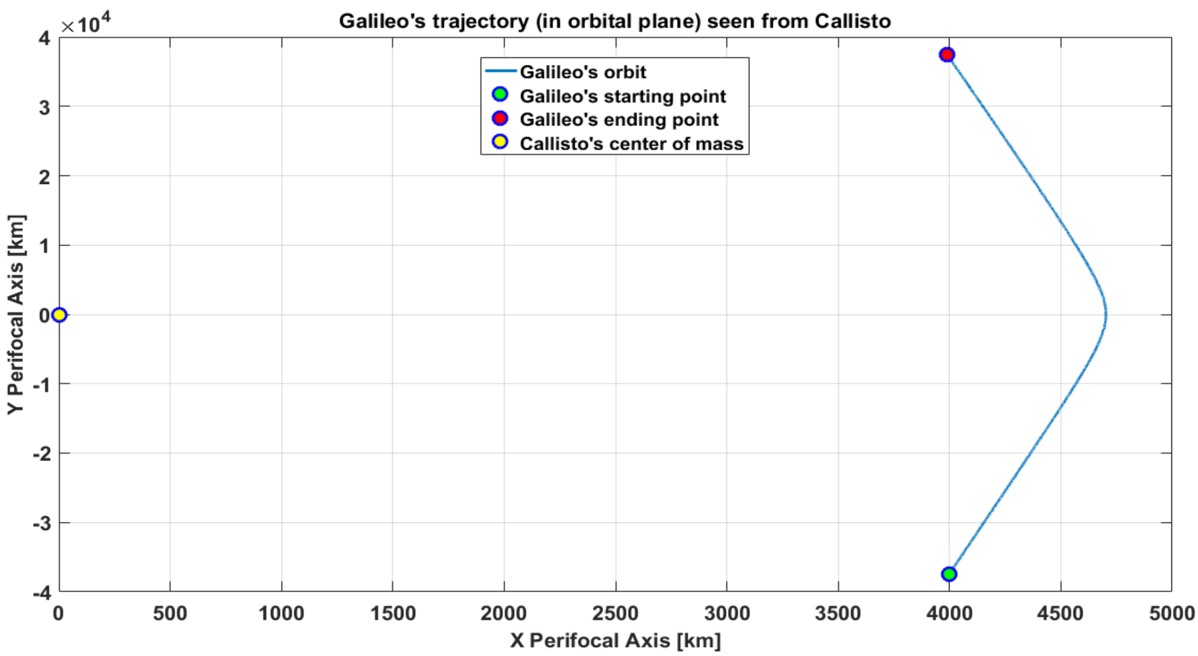

Figure 5.3: 2D representation of the flyby of Callisto on August 14, 1999 in a perifocal Callisto-centered frame. Please note that X- and Y- axes differ in scale.

All the flybys of Galilean moons made by the Galileo spacecraft have been between 1995 and 2002, so the data are relatively recent and reliable.

Appendix E gives illustrations of the distance variations for all the selected flybys. Clear variations of the distance (from the 8,000 km of Figure E.7 to the 200,000 km of Figures E.5 and E.8) are present, thus it can be stated that the observations are accurate also for this reason: no radial distance variation would mean zero relative velocity of the spacecraft with respect to the Earth, thus the Doppler effect would be useless. In particular, Figure E.7 would have the smallest accuracy-related advantage due to the fact that the distance from Earth varies less.

Please note that all these distances appear quite monotonic: they always increase or always decrease (almost) linearly, but never change their behavior throughout one flyby. This is due to the fact that the distance spacecraft-Earth is mainly dictated by the distance central body-Earth, while the variation of the spacecraft distance with respect to Earth is mainly driven by the velocity of the central body with respect to Earth, and not by the spacecraft's one, since the latter has been found to be always smaller than the former. In order to clearly understand this, please note that, in the worst-case scenario, the relative error that would be done by considering the distance of the central body with respect to Earth instead of the spacecraft's one is only about $6.4\cdot10^{-5}$ (when the spacecraft is at the limit of the sphere of influence of Callisto, at its apojove, between the Earth and Jupiter, which are respectively at their aphelion and perihelion), since the spacecraft orbital radius from the central body is very small when compared to its distance from the Earth.

5.2. TUNING OF RELATIVE TOLERANCE

A tuning of the integrator relative tolerance will now be performed. By simulating (straightforward, no fitting) the chosen low-altitude scenarios (the ones with the largest sensitivities for gravity field model errors) with ODE113 in modified equinoctial elements with an output time-step of 0.5 seconds (the minimum reachable by the JPL ephemerides), a relevant comparison between the Root Mean Square of position and velocity absolute errors, and also computation time, can be done by varying the relative tolerance allowed by the integrator. It is assumed that the RMSE on the position shall be at most $1\cdot10^{-2}$ m and the one on the velocity less or equal to $1\cdot10^{-5}$ m/s. Tables 5.2 to 5.9 show these differences; note that the solutions with the largest relative tolerance which fulfill the constraints on the RMSE are chosen and thus highlighted in green.

Table 5.2: Root mean square of absolute position and velocity errors, and computation time of the flyby I33 as function of the relative tolerance of the integrator.

Relative tolerance	$RMSE_{position}$ [m]	$RMSE_{velocity}$ [m/s]	Computation time [s]
$2\cdot10^{-14}$	7.216	$1.372\cdot10^{-2}$	48.28
$1\cdot10^{-9}$	7.217	$1.372\cdot10^{-2}$	21.09
$7\cdot10^{-9}$	7.223	$1.372\cdot10^{-2}$	18.62
$8\cdot10^{-9}$	7.224	$1.372\cdot10^{-2}$	18.08
$9\cdot10^{-9}$	7.231	$1.372\cdot10^{-2}$	17.37
$1\cdot10^{-8}$	7.366	$1.378\cdot10^{-2}$	14.45

Table 5.3: Root mean square of absolute position and velocity errors, and computation time of the flyby I0 as function of the relative tolerance of the integrator.

Relative tolerance	**RMSE$_{position}$ [m]**	**RMSE$_{velocity}$ [m/s]**	**Computation time [s]**
$2{\cdot}10^{-14}$	$2.396{\cdot}10^{-1}$	$1.301{\cdot}10^{-3}$	37.03
$1{\cdot}10^{-9}$	$2.420{\cdot}10^{-1}$	$1.301{\cdot}10^{-3}$	14.63
$4{\cdot}10^{-9}$	$2.445{\cdot}10^{-1}$	$1.301{\cdot}10^{-3}$	13.98
$5{\cdot}10^{-9}$	$2.480{\cdot}10^{-1}$	$1.301{\cdot}10^{-2}$	13.24
$6{\cdot}10^{-9}$	$2.503{\cdot}10^{-1}$	$1.301{\cdot}10^{-3}$	13.15
$1{\cdot}10^{-8}$	$4.629{\cdot}10^{-1}$	$1.304{\cdot}10^{-3}$	13.05

Table 5.4: Root mean square of absolute position and velocity errors, and computation time of the flyby E12 as function of the relative tolerance of the integrator.

Relative tolerance	**RMSE$_{position}$ [m]**	**RMSE$_{velocity}$ [m/s]**	**Computation time [s]**
$2{\cdot}10^{-14}$	12.02	$1.204{\cdot}10^{-2}$	61.65
$1{\cdot}10^{-9}$	12.03	$1.204{\cdot}10^{-2}$	24.68
$9{\cdot}10^{-9}$	12.10	$1.205{\cdot}10^{-2}$	23.80
$1{\cdot}10^{-8}$	12.12	$1.205{\cdot}10^{-2}$	23.60
$2{\cdot}10^{-8}$	12.19	$1.206{\cdot}10^{-2}$	23.07
$1{\cdot}10^{-7}$	12.31	$1.208{\cdot}10^{-2}$	20.40

Table 5.5: Root mean square of absolute position and velocity errors, and computation time of the flyby E15 as function of the relative tolerance of the integrator.

Relative tolerance	**RMSE$_{position}$ [m]**	**RMSE$_{velocity}$ [m/s]**	**Computation time [s]**
$2{\cdot}10^{-14}$	1.141	$1.242{\cdot}10^{-3}$	37.03
$1{\cdot}10^{-10}$	1.142	$1.242{\cdot}10^{-3}$	19.42
$8{\cdot}10^{-10}$	1.150	$1.243{\cdot}10^{-3}$	16.39
$9{\cdot}10^{-10}$	1.151	$1.243{\cdot}10^{-3}$	16.21
$1{\cdot}10^{-9}$	1.152	$1.243{\cdot}10^{-3}$	16.20

Table 5.6: Root mean square of absolute position and velocity errors, and computation time of the flyby G2 as function of the relative tolerance of the integrator.

Relative tolerance	**RMSE$_{position}$ [m]**	**RMSE$_{velocity}$ [m/s]**	**Computation time [s]**
$2{\cdot}10^{-14}$	1.320	$7.219{\cdot}10^{-4}$	67.10
$1{\cdot}10^{-11}$	1.323	$7.219{\cdot}10^{-4}$	41.45
$2{\cdot}10^{-11}$	1.328	$7.219{\cdot}10^{-4}$	39.73
$3{\cdot}10^{-11}$	1.330	$7.220{\cdot}10^{-4}$	36.48
$4{\cdot}10^{-11}$	1.336	$7.221{\cdot}10^{-4}$	35.92
$1{\cdot}10^{-10}$	1.365	$7.222{\cdot}10^{-4}$	35.03

Table 5.7: Root mean square of absolute position and velocity errors, and computation time of the flyby G29 as function of the relative tolerance of the integrator.

Relative tolerance	$RMSE_{position}$ [m]	$RMSE_{velocity}$ [m/s]	Computation time [s]
$2{\cdot}10^{-14}$	$5.704{\cdot}10^{-1}$	$4.080{\cdot}10^{-4}$	42.85
$1{\cdot}10^{-11}$	$5.710{\cdot}10^{-1}$	$4.080{\cdot}10^{-4}$	27.36
$9{\cdot}10^{-11}$	$5.737{\cdot}10^{-1}$	$4.080{\cdot}10^{-4}$	23.45
$1{\cdot}10^{-10}$	$5.737{\cdot}10^{-1}$	$4.080{\cdot}10^{-4}$	23.09
$2{\cdot}10^{-10}$	$5.864{\cdot}10^{-1}$	$4.081{\cdot}10^{-4}$	22.99
$1{\cdot}10^{-9}$	$6.482{\cdot}10^{-1}$	$4.085{\cdot}10^{-4}$	20.41

Table 5.8: Root mean square of absolute position and velocity errors, and computation time of the flyby C30 as function of the relative tolerance of the integrator.

Relative tolerance	$RMSE_{position}$ [m]	$RMSE_{velocity}$ [m/s]	Computation time [s]
$2{\cdot}10^{-14}$	16.52	$7.302{\cdot}10^{-3}$	60.38
$1{\cdot}10^{-10}$	16.52	$7.302{\cdot}10^{-3}$	41.07
$2{\cdot}10^{-10}$	16.52	$7.303{\cdot}10^{-3}$	38.21
$3{\cdot}10^{-10}$	16.53	$7.303{\cdot}10^{-3}$	35.74
$4{\cdot}10^{-10}$	16.54	$7.304{\cdot}10^{-3}$	34.77
$1{\cdot}10^{-9}$	16.70	$7.307{\cdot}10^{-3}$	30.72

Table 5.9: Root mean square of absolute position and velocity errors, and computation time of the flyby C22 as function of the relative tolerance of the integrator.

Relative tolerance	$RMSE_{position}$ [m]	$RMSE_{velocity}$ [m/s]	Computation time [s]
$2{\cdot}10^{-14}$	1.454	$5.484{\cdot}10^{-4}$	60.38
$1{\cdot}10^{-11}$	1.458	$5.484{\cdot}10^{-4}$	34.15
$2{\cdot}10^{-11}$	1.462	$5.484{\cdot}10^{-4}$	31.03
$3{\cdot}10^{-11}$	1.474	$5.484{\cdot}10^{-4}$	30.04
$1{\cdot}10^{-10}$	1.502	$5.485{\cdot}10^{-4}$	27.95

Thus, the relative tolerances for the low- and high-altitude flybys are respectively $8{\cdot}10^{-9}$ and $5{\cdot}10^{-9}$ for Io, $1{\cdot}10^{-8}$ and $9{\cdot}10^{-10}$ for Europa, $3{\cdot}10^{-11}$ and $1{\cdot}10^{-10}$ for Ganymede, and $3{\cdot}10^{-10}$ and $2{\cdot}10^{-11}$ for Callisto.

5.3. TUNING OF DATA ACQUISITION STEP-SIZE

In this section, the step-size of the data acquisition will be tuned in such a way that trajectory propagation and optimization will be done with accurate results and in a moderate amount of time. In particular, the JPL ephemerides have a sensitivity of 0.5 s, i.e. this is the minimum amount of time needed to consider two points as different. Tables from 5.10 to 5.17 indicates how the root mean square of position and velocity absolute errors, and also the computation time, vary by changing the time-step between two data points (and thus the total number of points), by using the relative tolerance chosen in Section 5.2. Note that the solutions with the minimum data acquisition step-size which fulfill the constraints on RMSE are chosen and thus highlighted in green.

Table 5.10: Root mean square of absolute position and velocity errors, and computation time for flyby I33 as function of the time-step between two data points. The relative tolerance is equal to $8 \cdot 10^{-9}$.

Data acquisition step-size [s]	$\mathrm{RMSE_{position}}$ [m]	$\mathrm{RMSE_{velocity}}$ [m/s]	Computation time [s]
0.5	7.224	$1.372 \cdot 10^{-2}$	18.08
10	7.225	$1.374 \cdot 10^{-2}$	18.04
30	7.225	$1.375 \cdot 10^{-2}$	18.02
60	7.226	$1.376 \cdot 10^{-2}$	17.98
120	7.226	$1.378 \cdot 10^{-2}$	17.95

Table 5.11: Root mean square of absolute position and velocity errors, and computation time for flyby I0 as function of the time-step between two data points. The relative tolerance is equal to $5 \cdot 10^{-9}$.

Data acquisition step-size [s]	$\mathrm{RMSE_{position}}$ [m]	$\mathrm{RMSE_{velocity}}$ [m/s]	Computation time [s]
0.5	$2.480 \cdot 10^{-1}$	$1.301 \cdot 10^{-2}$	13.24
10	$2.480 \cdot 10^{-1}$	$1.301 \cdot 10^{-2}$	13.24
30	$2.480 \cdot 10^{-1}$	$1.301 \cdot 10^{-2}$	13.24
60	$2.480 \cdot 10^{-1}$	$1.301 \cdot 10^{-2}$	13.24
120	$2.480 \cdot 10^{-1}$	$1.301 \cdot 10^{-2}$	13.24

Table 5.12: Root mean square of absolute position and velocity errors, and computation time for flyby E12 as function of the time-step between two data points. The relative tolerance is equal to $1 \cdot 10^{-8}$.

Data acquisition step-size [s]	$\mathrm{RMSE_{position}}$ [m]	$\mathrm{RMSE_{velocity}}$ [m/s]	Computation time [s]
0.5	12.12	$1.205 \cdot 10^{-2}$	23.60
10	12.13	$1.207 \cdot 10^{-2}$	23.55
30	12.13	$1.208 \cdot 10^{-2}$	23.53
60	12.13	$1.209 \cdot 10^{-2}$	23.51
120	12.14	$1.211 \cdot 10^{-2}$	23.47

Table 5.13: Root mean square of absolute position and velocity errors, and computation time for flyby E15 as function of the time-step between two data points. The relative tolerance is equal to $9 \cdot 10^{-10}$.

Data acquisition step-size [s]	$\mathrm{RMSE_{position}}$ [m]	$\mathrm{RMSE_{velocity}}$ [m/s]	Computation time [s]
0.5	1.151	$1.243 \cdot 10^{-3}$	16.21
10	1.151	$1.243 \cdot 10^{-3}$	16.21
30	1.151	$1.243 \cdot 10^{-3}$	16.21
60	1.151	$1.243 \cdot 10^{-3}$	16.21
120	1.151	$1.243 \cdot 10^{-3}$	16.21

Table 5.14: Root mean square of absolute position and velocity errors, and computation time for flyby G2 as function of the time-step between two data points. The relative tolerance is equal to $3 \cdot 10^{-11}$.

Data acquisition step-size [s]	**RMSE$_{\text{position}}$ [m]**	**RMSE$_{\text{velocity}}$ [m/s]**	**Computation time [s]**
0.5	1.330	$7.220 \cdot 10^{-4}$	36.48
10	1.331	$7.228 \cdot 10^{-4}$	36.41
30	1.331	$7.231 \cdot 10^{-4}$	36.38
60	1.331	$7.232 \cdot 10^{-4}$	36.35
120	1.332	$7.236 \cdot 10^{-4}$	36.32

Table 5.15: Root mean square of absolute position and velocity errors, and computation time for flyby G29 as function of the time-step between two data points. The relative tolerance is equal to $1 \cdot 10^{-10}$.

Data acquisition step-size [s]	**RMSE$_{\text{position}}$ [m]**	**RMSE$_{\text{velocity}}$ [m/s]**	**Computation time [s]**
0.5	$5.737 \cdot 10^{-1}$	$4.080 \cdot 10^{-4}$	23.09
10	$5.737 \cdot 10^{-1}$	$4.080 \cdot 10^{-4}$	23.09
30	$5.737 \cdot 10^{-1}$	$4.080 \cdot 10^{-4}$	23.09
60	$5.737 \cdot 10^{-1}$	$4.080 \cdot 10^{-4}$	23.09
120	$5.737 \cdot 10^{-1}$	$4.080 \cdot 10^{-4}$	23.09

Table 5.16: Root mean square of absolute position and velocity errors, and computation time for flyby C30 as function of the time-step between two data points. The relative tolerance is equal to $3 \cdot 10^{-10}$.

Data acquisition step-size [s]	**RMSE$_{\text{position}}$ [m]**	**RMSE$_{\text{velocity}}$ [m/s]**	**Computation time [s]**
0.5	16.53	$7.303 \cdot 10^{-3}$	35.74
10	16.55	$7.304 \cdot 10^{-3}$	35.68
30	16.55	$7.304 \cdot 10^{-3}$	35.65
60	16.55	$7.304 \cdot 10^{-3}$	35.62
120	16.56	$7.305 \cdot 10^{-3}$	35.58

Table 5.17: Root mean square of absolute position and velocity errors, and computation time for flyby C22 as function of the time-step between two data points. The relative tolerance is equal to $2 \cdot 10^{-11}$.

Data acquisition step-size [s]	**RMSE$_{\text{position}}$ [m]**	**RMSE$_{\text{velocity}}$ [m/s]**	**Computation time [s]**
0.5	1.462	$5.484 \cdot 10^{-4}$	31.03
10	1.462	$5.484 \cdot 10^{-4}$	31.03
30	1.462	$5.488 \cdot 10^{-4}$	30.86
60	1.463	$5.491 \cdot 10^{-4}$	30.71
120	1.463	$5.494 \cdot 10^{-4}$	30.40

Since the 0.5 s data acquisition step-size is the one with the largest number of data-points and has a computation time which is roughly the same as for other observation frequencies (but with a greater precision, i.e. smaller RMSE), it will be chosen for all the flybys.

5.4. SYNOPSIS: GALILEO'S FLYBYS SELECTION

Galileo has been the only spacecraft to enter the Galilean moons' spheres of influence with respect to Jupiter, thus only its state-related data can be useful for the purpose of this paper.

The flybys with the lowest and highest altitudes which fulfill the constraint on the Earth's elevation angle (i.e. its absolute value shall be less than 20°) and which will then be analyzed are I0, I33, E12, E15, G2, G29, C22 and C30.

Furthermore, the data-acquisition step-size is 0.5 s, while the relative tolerances for the low- and high-altitudes flybys are respectively $8{\cdot}10^{-9}$ and $5{\cdot}10^{-9}$ for Io, $1{\cdot}10^{-8}$ and $9{\cdot}10^{-10}$ for Europa, $3{\cdot}10^{-11}$ and $1{\cdot}10^{-10}$ for Ganymede, and $3{\cdot}10^{-10}$ and $2{\cdot}10^{-11}$ for Callisto. They are different, but this does not constitutes an issue, since the optimization will be done independently for each flyby. Absolute tolerances will not be tuned, because MATLAB integrators consider only the maximum tolerance between the absolute and the product of the relative by the state. Since the absolute tolerance can be set as small as about $2{\cdot}10^{-16}$, it has always been set to this value, but it will not be taken into account by ODE113, since $2{\cdot}10^{-16}$ will always be smaller than the product of the minimum relative tolerance $2{\cdot}10^{-14}$ and the state of the spacecraft in Cartesian coordinates (the integrator receives Cartesian coordinates as inputs, since modified equinoctial elements are not provided by SPICE).

6

Optimization

In order to improve the dynamical model used to propagate Galileo's trajectory, optimization will be performed. The parameters to be optimized are the components of the initial state of the Galileo spacecraft, but also the spherical harmonics of the moon under analysis.

6.1. State of the art optimization options

In Noomen [2015], the optimization techniques are divided in analytical and numerical. The analytical are mainly based on setting a zero derivative to get the optimum value, however this is not always possible or convenient (large amount of time to obtain reliable results), and numerical techniques are needed. This latter group is divided in other main subgroups as in Table 6.1.

Table 6.1: Comparison of numerical optimisation techniques (adapted from Noomen [2015]).

Technique	**Advantages**	**Disadvantages**
Sampling:		
Grid Search	simple implementation	slow
	need not be differentiable	not robust (limited resolution)
Monte Carlo	simple implementation	simple problems only
	need not be differentiable	luck
		not robust (limited resolution)
Latin Hypercube sampling, Sobol sampling	simple implementation	simple problems only
	need not be differentiable	luck
	variable combinations → more regular sampling	not robust
Local optimisation:		
Nelder-Mead	simple	local minimum
Newton-Raphson (1d)	simple	slow convergence near flat optimum
		local minimum and maximum
steepest descent (along axes)	simple	oscillations
	always finds a minimum	slow convergence
	only storage of gradient info	local minimum
steepest descent (arbitrary direction)	always finds a minimum	local minimum
	better convergence than steepest descent along axes	Hessian matrix
		double-differentiable
Metaheuristics:		
Genetic Algorithm Differential Evolution Particle Swarm Optimisation (Adaptive) Simulated Annealing Ant Colony Optimisation Dynamic Programming Interval Analysis	robust; no need for differentiable; good initial value not necessary; direct aim on solution	many iterations (or evaluations); convergence unclear; scales poorly with problem size; slow for large number of parameters

Sampling techniques allow to find the optimum by evaluating the function in samples. Two relevant examples of sampling techniques which are widely used are the Grid Search and the Monte Carlo technique. In the Grid Search, the function evaluations are computed in samples which lie in a defined grid, in which it is possible to set a specific resolution. In the Monte Carlo technique these samples do not belong to a grid, but are instead randomly chosen.

Local optimization techniques allow to find only local optima by computing the derivative of the function, but may get stuck at that optimum. Furthermore, the continuously differentiability of the function is a condition that is not always satisfied. Newton-Raphson (1d) and the steepest descent techniques are gradient-based; indeed they require the derivative of the function in order to find the optimum, but this constitutes a limit to the generality of problems that they can solve.

Metaheuristics ("methodic research at higher level", according to Noomen [2015]) techniques in general do not require the differentiability of the function instead, but they need many iterations (or evaluations). In particular, a fundamental characteristic of this algorithm is that it allows the elements of the population to produce offspring (thanks to crossover), the best of which will remain also for the next iteration (note that there are many possible implementations of these algorithms, e.g. probability of mutation and percentage of elitism can vary).

The Grid Search technique has been chosen, because it is simple to implement, do not need a differentiable function and it is not based on luck. Due to the strongly demanding computation time needed for this operation, in this chapter the process will be divided into two phases and then iterated. During the first phase, a Grid Search technique will be performed for each flyby with the components of the initial state as parameters to be estimated, while, during the second, another Grid Search will be done per flyby with the moons' spherical harmonics as inputs. The goal is to achieve the minimum root mean square error from the JPL ephemerides.

6.2. FIRST INITIAL STATE GRID SEARCH

In order to obtain simulations which better approximate the JPL ephemerides, the resolution of the deviations from the initial state has been set to 0.25 m for each position component and $0.25{\cdot}10^{-3}$ m/s for each velocity component, since with these variations the RMSE on position and velocity have been tested to have variations of respectively less than $1{\cdot}10^{-2}$ m and $1{\cdot}10^{-5}$ m/s.

Since there are six components which can be subjected to their nominal values, if everyone had n possibility of variations, the amount of time needed to complete the Grid Search would be n^6 times that of a single propagation. In order to allow for a perturbation of only ± 1 m (and ± 1 mm/s), n should be 9, i.e. 4 positive, 4 negative and the nominal one. This would lead to more than 500,000 combinations and hence to a total amount of time of about one year per flyby, by considering one minute as the time needed to propagate a single flyby. Due to the restricted time availability, a non-straightforward approach to the Grid Search has been adopted. It has been chosen to perturb each component by ± 0.25 m (and $\pm 0.25{\cdot}10^{-3}$ m/s), choose the best set and perturb its components by the same amount, finally do it iteratively until convergence. This leads to a much faster optimization, since it does not take into account the area of minor interest.

Grid Search simulations have been performed so that an optimal and potential new initial state would result: the one with the least RMSE = RMSE_{pos} + RMSE_{vel}. This particular objective has been chosen since it gives the greatest importance to position but still considers velocity when small variations of the initial state are required. Note that it has been tested that the same result would have been obtained by minimizing RMSE_{pos} only, however when further refinements are needed, RMSE_{vel} becomes important. Note also that by minimizing only RMSE_{vel}, the initial state would be completely different and in particular RMSE_{pos} would be much higher, because for now the greatest error is related to the position. The reader will of course notice that an error in any acceleration would cause a certain variation in velocity, its integral, but a much greater one on the position, since this latter is the integral of the velocity, i.e. the double integral of the acceleration.

Values for RMSE_{pos} and RMSE_{vel} (before and after having done the Grid Searches with steps in the initial state of 0.25 m and $0.25 \cdot 10^{-3}$ m/s) are provided in Table 6.2.

Table 6.2: Values of RMSE_{pos} and RMSE_{vel} before and after the Grid Searches performed with a step-size of 0.25 m and $0.25 \cdot 10^{-3}$ m/s.

Flyby ID	**RMSE_{pos} before Grid Search [m]**	**RMSE_{pos} after Grid Search [m]**	**RMSE_{vel} before Grid Search [10^{-3} m/s]**	**RMSE_{vel} after Grid Search [10^{-3} m/s]**
I33	7.216	2.598	13.72	10.32
I0	0.240	0.159	1.301	1.240
E12	13.20	7.515	13.29	9.743
E15	0.984	0.396	1.047	0.846
G2	1.320	0.498	0.722	0.651
G29	0.570	0.355	0.408	0.351
C30	16.52	7.500	7.302	6.303
C22	1.454	0.581	0.548	0.420

Table 6.3 provides the variations of the initial state in J2000 coordinates as resulting from the Grid Search technique. Clearly, the total changes are multiples of 0.25 m and $0.25 \cdot 10^{-3}$ m/s for position and velocity, respectively.

Table 6.3: Variations of the initial state in J2000 coordinates as a result of the Grid Search technique.

Flyby ID	**Δx_0 [m]**	**Δy_0 [m]**	**Δz_0 [m]**	**Δv_{x_0} [10^{-3} m/s]**	**Δv_{y_0} [10^{-3} m/s]**	**Δv_{z_0} [10^{-3} m/s]**
I33	+3.00	-2.25	+2.75	-6.75	+5.50	-6.25
I0	+0.00	+0.00	+0.00	+0.25	+0.25	-0.25
E12	+3.00	-4.50	+0.50	-4.75	+6.50	-0.50
E15	+0.25	+0.00	-0.25	-0.75	+0.25	+0.25
G2	-0.25	-0.25	-0.25	+0.25	-0.25	+0.00
G29	-0.25	-0.25	-0.25	+0.25	+0.00	+0.00
C30	-3.50	-4.75	+11.50	+2.00	+2.00	-5.25
C22	+0.00	-0.50	+0.50	+0.00	+0.25	-0.25

6.3. FIRST SPHERICAL HARMONICS GRID SEARCH

Next, another Grid Search will be performed with the same relative tolerances already defined, but this time with the Galilean moons' spherical harmonics as parameters, in order to improve their gravity field and the results of this project.

6.3.1. SENSITIVITY CONSIDERATIONS

By looking at the papers which show the values of these moons' spherical harmonics, it can be seen that the ratio between the formal uncertainty and the nominal value is in general equal to $1 \cdot 10^{-6}$ for the gravitational parameter μ, $1 \cdot 10^{-2}$ for the zonal harmonics J_n, and $1 \cdot 10^{-1}$ for the tesseral harmonics $J_{n,m}$. The formal uncertainties can be used to perform a sensitivity analysis: by changing the nominal values of the moons' μ, J_n and $J_{n,m}$ up to their formal uncertainties, but also the μ of the third bodies which are not Galilean moons (Sun and Jupiter) and the Jovian J_2, the root mean square errors on position and velocity change, since they are the parameters that affect the objective value in the simulation. If these RMSE respectively change by less than $1 \cdot 10^{-2}$ m and $1 \cdot 10^{-5}$ m/s, then the parameter under analysis can be neglected and it will not play a role in the Grid Search which is going to be performed.

In the estimation process, all the known harmonics and those of one order greater than the highest known one will be considered. Since it can be assumed that the nominal values for these latter harmonics are zero, but there are no uncertainties, it can also be assumed that the uncertainties are $100 \cdot 10^{-6}$ for the zonal harmonics and $10 \cdot 10^{-6}$ for the tesseral ones (realistic values induced by looking at the spherical harmonics that are known). Please note that only J_2 and $C_{2,2}$ are excluded from this range because of their great importance, however nominal values and corresponding formal uncertainties are provided for each moon, so they do not create any problem with respect to this assumption.

According to the papers which furnished the Galilean spherical harmonics, it is common practice to use a sensitivity of $0.1 \cdot 10^{-6}$ (hence, same for the Grid Search step-size) for their evaluation, and for this reason this will be also the sensitivity used in this project. The only exception is Ganymede since it has already a very precise gravity field, for which a Grid Search step-size of $0.001 \cdot 10^{-6}$ is required.

6.3.2. FIRST SPHERICAL HARMONICS ESTIMATES

The performed Grid Searches provide two interesting results. The first is that the μ of the Sun, Jupiter and the Galilean moons, as well as the Jovian J_2 are very precise and changes in their values do not lead to any improvement. The second interesting result is that for each set of flybys of a specific moon, the same estimates for the spherical harmonics have been obtained through the Grid Search.

Table 6.4 provides the literature values for some nominal spherical harmonics coefficients, evaluated new values for them (in cyan) and estimated values for other new ones (in yellow) as resulting from the Grid Search optimization. The variation between the new and old values are also shown. Note that more decimal places for these values can be found in Table F.1 in Appendix F.

Table 6.4: Literature values for some nominal spherical harmonics, evaluated new values for them (in cyan) and estimated values for other new ones (in yellow) as resulting from the Grid Search optimization are presented. The variation between the new and the old values are also shown. Note that more decimal places for these values can be found in Table F.1 in Appendix F.

Moon	**Old spherical harmonics** [10^{-6}]	**New spherical harmonics** [10^{-6}]	**Variation of spherical harmonics** [10^{-6}]
Io	J_2 = 1845.9	J_2 = 1842.6	ΔJ_2 = -3.3
	$S_{2,1}$ = N.A. (0.0)	$S_{2,1}$ = 0.8	$\Delta S_{2,1}$ = 0.8
	$C_{2,2}$ = 553.7	$C_{2,2}$ = 552.5	$\Delta C_{2,2}$ = -1.2
	$C_{3,2}$ = N.A. (0.0)	$C_{3,2}$ = -0.4	$\Delta C_{3,2}$ = -0.4
	$C_{4,1}$ = N.A. (0.0)	$C_{4,1}$ = -0.5	$\Delta C_{4,1}$ = -0.5
Europa	J_2 = 435.5	J_2 = 432.3	ΔJ_2 = -3.2
	$S_{2,1}$ = 14.0	$S_{2,1}$ = -1.0	$\Delta S_{2,1}$ = -15.0
	$C_{2,2}$ = 131.5	$C_{2,2}$ = 129.0	$\Delta C_{2,2}$ = -2.5
	$C_{3,2}$ = N.A. (0.0)	$C_{3,2}$ = -0.7	$\Delta C_{3,2}$ = -0.7
	$S_{3,3}$ = N.A. (0.0)	$S_{3,3}$ = -1.0	$\Delta S_{3,3}$ = -1.0
	J_4 = N.A. (0.0)	J_4 = 2.1	ΔJ_4 = 2.1
Ganymede	J_9 = N.A. (0.000)	J_9 = 0.014	ΔJ_9 = 0.014
Callisto	J_2 = 32.7	J_2 = 33.3	ΔJ_2 = 0.6
	$C_{2,1}$ = 0.0	$C_{2,1}$ = 1.0	$\Delta C_{2,1}$ = 1.0
	$S_{2,1}$ = 0.0	$S_{2,1}$ = 1.6	$\Delta S_{2,1}$ = 1.6
	$C_{2,2}$ = 10.2	$C_{2,2}$ = 9.9	$\Delta C_{2,2}$ = -0.3
	$S_{2,2}$ = -1.1	$S_{2,2}$ = -0.8	$\Delta S_{2,2}$ = 0.3
	$C_{3,2}$ = N.A. (0.0)	$C_{3,2}$ = -0.1	$\Delta C_{3,2}$ = -0.1
	$S_{3,2}$ = N.A. (0.0)	$S_{3,2}$ = -0.2	$\Delta S_{3,2}$ = -0.2

Please note that, among the changed ten spherical harmonics, only the updates on Europa's $\Delta S_{2,1}$ and Callisto's $\Delta C_{2,1}$ are beyond the formal uncertainties provided by the corresponding papers, i.e. $12.0 \cdot 10^{-6}$ (page 2020 of Anderson et al. [1998]) and $0.3 \cdot 10^{-6}$ (page 157 of Anderson et al. [2001]). This means that the other eight coefficients lie inside the uncertainty range in which their true values are more probable to be, while these latter two not.

Values for $RMSE_{pos}$ and $RMSE_{vel}$ (before and after the Grid Searches performed with a step-size of $0.1 \cdot 10^{-6}$ (and $0.001 \cdot 10^{-6}$ for Ganymede)) are presented in Table 6.5, of course with the new initial states shown in Table 6.3.

Table 6.5: Values of $RMSE_{pos}$ and $RMSE_{vel}$ before and after the Grid Searches performed with a step-size of $0.1 \cdot 10^{-6}$ (and $0.001 \cdot 10^{-6}$ for Ganymede), with the new initial states shown in Table 6.3.

Flyby ID	**$RMSE_{pos}$ before Grid Search [m]**	**$RMSE_{pos}$ after Grid Search [m]**	**$RMSE_{vel}$ before Grid Search [10^{-3} m/s]**	**$RMSE_{vel}$ after Grid Search [10^{-3} m/s]**
I33	2.598	2.422	10.32	9.322
I0	0.159	0.156	1.240	1.235
E12	7.515	2.708	9.743	6.110
E15	0.396	0.359	0.846	0.805
G2	0.498	0.486	0.651	0.639
G29	0.355	0.354	0.351	0.350
C30	7.500	6.446	6.303	5.351
C22	0.581	0.567	0.420	0.298

6.4. SECOND INITIAL STATE GRID SEARCH

Now the Grid Searches which have as parameters the initial state components of the Galileo spacecraft will be performed again, but this time with the new spherical harmonics, to refine the results.

Values for $RMSE_{pos}$ and $RMSE_{vel}$ (before and after the second round of Grid Searches performed with a step-size of 0.25 m and $0.25 \cdot 10^{-3}$ m/s) are presented in Table 6.6.

Table 6.6: Values of $RMSE_{pos}$ and $RMSE_{vel}$ before and after the second round of Grid Searches performed with a step-size of 0.25 m and $0.25 \cdot 10^{-3}$ m/s.

Flyby ID	**$RMSE_{pos}$ before Grid Search [m]**	**$RMSE_{pos}$ after Grid Search [m]**	**$RMSE_{vel}$ before Grid Search [10^{-3} m/s]**	**$RMSE_{vel}$ after Grid Search [10^{-3} m/s]**
I33	2.422	2.247	9.322	9.090
I0	0.156	0.147	1.235	1.197
E12	2.708	2.347	6.110	6.018
E15	0.359	0.359	0.805	0.805
G2	0.486	0.478	0.639	0.638
G29	0.354	0.354	0.350	0.350
C30	6.446	5.989	5.351	5.131
C22	0.567	0.481	0.298	0.295

Table 6.7 provides the variations of the initial state in J2000 coordinates (with respect to the last initial state, defined in Table 6.3) as resulting from the second round of the Grid Search technique.

Table 6.7: Variations of the initial state in J2000 coordinates (with respect to the last initial state, defined in Table 6.3) as resulting from the the second round of Grid Search technique.

Flyby ID	$\Delta\mathbf{x}_0$ **[m]**	$\Delta\mathbf{y}_0$ **[m]**	$\Delta\mathbf{z}_0$ **[m]**	$\Delta\mathbf{v}_{x_0}$ $[10^{-3}$ **m/s]**	$\Delta\mathbf{v}_{y_0}$ $[10^{-3}$ **m/s]**	$\Delta\mathbf{v}_{z_0}$ $[10^{-3}$ **m/s]**
I33	-0.25	+0.50	-0.50	+0.75	-0.75	+1.00
I0	+0.00	+0.00	+0.00	+0.00	-0.25	+0.00
E12	+0.25	+1.00	+0.00	+0.25	-1.00	+0.25
E15	+0.00	+0.00	+0.00	+0.00	+0.00	+0.00
G2	+0.00	+0.25	+0.00	+0.00	+0.00	+0.00
G29	+0.00	+0.00	+0.00	+0.00	+0.00	+0.00
C30	-0.50	+0.00	-1.25	+0.00	+0.00	+0.75
C22	+0.00	+0.00	+0.25	+0.00	+0.00	+0.00

Note that there are two flybys, E15 and G29, which have not been subjected to any further variation in the initial state, thus the next spherical harmonic Grid Search will not be performed again for them, since the results would not change.

6.5. Second Spherical Harmonics Grid Search

The second round of spherical harmonics coefficients by means of Grid Search shows no improvement: all the flybys have the same spherical harmonics as before, and thus the same RMSE. In particular, note from Table 6.7 that the flybys are either not subjected to any change in initial state or just for a very small amount. This means that the end of the iterative harmonics coefficients estimation process (and of course of the initial state Grid Searches as well) has been reached. Note that this fact is not an indication of a missing perturbation, rather of convergence: the proposed model fits the nominal JPL ephemerides at its best. Remember that also these latter ones are affected by error.

6.6. Synopsis: Optimization outcomes

Tables 6.4 and 6.7 respectively show the values of the Galilean moons' spherical harmonics as estimated through the Grid Search technique, and the variation in the J2000 moon-centered initial state of the Galileo spacecraft with respect to the JPL ephemerides.

Table 6.6 contains instead the final values of the RMSE for both position and velocity. Due to the fact that all the RMSE on the position are smaller than 9 m (maximum error on JPL ephemerides), it is assessed that the quality of the optimized trajectories appear to be high. In particular, a small RMSE indicates that the corresponding optimized trajectory is very similar to the nominal JPL one, i.e. the most probable to be correct (among the trajectories which can be created by allowing a variation from it of up to 9 m).

7

Further results

In this chapter, physical considerations related to the estimates of some spherical harmonics coefficients will be presented, along with the verification of these latter ones by means of the study of eight other flybys. Then, the obtained errors will be interpreted, decomposed along the LO-axes and finally related to the initial Keplerian elements (of the orbits corresponding to those flybys) and the Earth's elevation angle.

7.1. Physical considerations

This section does not present a prime objective of the research, but rather a by-product: the determination of the hydrostaticity of the Galilean moons.

A moon is said to be in hydrostatic equilibrium when gravity and pressure gradient forces balance themselves (page 63 of White [2008]). It is now interesting to understand which body, if any, among the Galilean moons can be considered to be in this state. According to page 1190 of Gao and Stevenson [2013], this happens to be the case when the ratio between J_2 and $C_{2,2}$ of a synchronously rotating body is 10/3.

Since all the four moons are synchronous, only their $\frac{J_2}{C_{2,2}}$ ratio remains to be computed. A new parameter λ_{nh}, which indicates the deviation from the hydrostatic state, is defined in Equation (7.1) (page 1190 of Gao and Stevenson [2013]):

$$\lambda_{nh} = 100 \cdot \frac{\frac{J_2}{C_{2,2}} - \frac{10}{3}}{\frac{10}{3}} \quad \% \tag{7.1}$$

It can be said that the bigger $|\lambda_{nh}|$ is, the less hydrostatic a body will be.

By using the old and new values of J_2 and $C_{2,2}$ as presented in Table 6.4, the corresponding computed values of λ_{nh} are shown in Table 7.1.

Table 7.1: Values of λ_{nh} as computed by using the old and the new spherical harmonics coefficients. The variation between the new and the old values are also shown.

Moon	$\lambda_{nh_{OLD}}$ [%]	$\lambda_{nh_{NEW}}$ [%]	$\Delta\lambda_{nh}$ [%]
Io	0.013	0.051	0.038
Europa	-0.646	0.535	1.181
Ganymede	-0.101	-0.101	0.000
Callisto	-3.824	0.909	4.733

By looking at the second and third columns of Table 7.1, it can be seen how Io turned out to be less hydrostatic than previously thought, while Europa and Callisto are apparently more hydrostatic (it is the absolute value of λ_{nh} which determines the nonhydrostaticity). Ganymede exhibits the same λ_{nh} value, since its J_2 and $C_{2,2}$ did not change during the Grid Searches.

A more direct visualization of these conclusions can be obtained by looking at the legend of Figure 7.1: all the Galilean moons have a $\frac{J_2}{C_{2,2}}$ ratio near the hydrostatic one (nearer than the Moon, and much nearer than planets like the Earth, Mars and Jupiter, which are definitely nonhydrostatic), however none of those is perfectly hydrostatic.

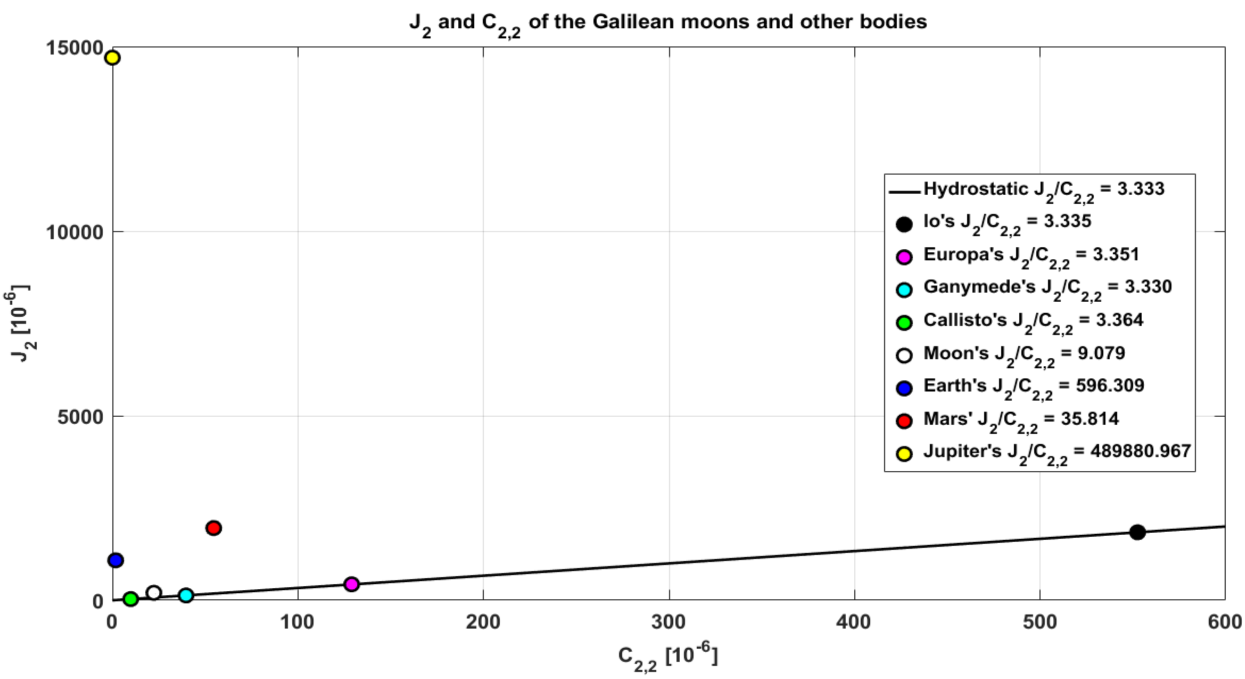

Figure 7.1: J_2 and $C_{2,2}$ of the Galilean moons, and their ratio (for hydrostatic considerations). Also the values for the Moon (page 1429 of Konopliv et al. [2013]), the Earth (page 529 of Wakker [2015]), Mars (page 6 of Liu et al. [2012]) and Jupiter (page 370 of Campbell and Synnott [1985]) are presented for comparison purposes.

From Figure 7.1, it can be realized that, while the planets orbit about the Sun, they do not change their shape much (Jupiter in particular): this leads to high internal stresses, since they are not released in a shape deformation of the body itself. This is different for the analyzed moons, the Galilean in particular, since they are subjected to a change in shape which hence allows to decrease the internal stresses.

It shall be noticed that, if the ratio is higher than the one for hydrostaticity (true for all the bodies except Ganymede), then it can be induced that J_2 is higher than the hydrostatic J_2 and/or $C_{2,2}$ is less than the hydrostatic $C_{2,2}$; when the ratio is less than the hydrostatic one instead (true only for Ganymede), it is vice-versa. In order to have a better physical insight, please remember that J_2 is a zonal harmonic and thus the acceleration it causes depends only on latitude ϕ (and so how much the radius changes by changing the latitude), while $C_{2,2}$ is sectorial, hence only the longitude λ (and so how much the radius changes by changing longitude) affects the related acceleration.

Due to the fact that J_2 and $C_{2,2}$ have a certain accuracy, according to Michigan State University [2003] the maximum error on λ_{nh} is given by Equation (7.2):

$$\begin{aligned}\delta\lambda_{nh} &= \sqrt{\left(\frac{\partial\lambda_{nh}}{\partial J_2}\,\delta J_2\right)^2+\left(\frac{\partial\lambda_{nh}}{\partial C_{2,2}}\,\delta C_{2,2}\right)^2} = \sqrt{\left(\frac{30}{C_{2,2}}\,\delta J_2\right)^2+\left(-\frac{30J_2}{C_{2,2}^2}\,\delta C_{2,2}\right)^2} = \\ &= \frac{30}{C_{2,2}}\sqrt{\left(\delta J_2\right)^2+\left(\frac{J_2}{C_{2,2}}\,\delta C_{2,2}\right)^2}\end{aligned} \tag{7.2}$$

where $\delta\lambda_{nh}$, δJ_2, $\delta C_{2,2}$ indicate the accuracy of λ_{nh}, J_2 and $C_{2,2}$.

The accuracy of J_2 and $C_{2,2}$ is $0.1\cdot10^{-6}$, thus the values for the accuracy of $\delta\lambda_{nh}$ as given by Equation (7.2) are presented in Table 7.2.

Table 7.2: Values of the accuracy of λ_{nh} for the new spherical harmonics.

Moon	$\delta\lambda_{nh_{NEW}}$ **[%]**
Io	$1.9\cdot10^{-8}$
Europa	$8.1\cdot10^{-8}$
Ganymede	$2.6\cdot10^{-7}$
Callisto	$1.1\cdot10^{-6}$

Since $\delta\lambda_{nh}$ is very small for every moon, it can be concluded that the nominal values presented in Table 7.1 are accurate, and thus the possible errors on λ_{nh} do not affect the determination of the hydrostaticity of the bodies.

7.2. VERIFICATION OF THE SPHERICAL HARMONICS COEFFICIENTS

In order to prove that the new spherical harmonics better approximate the gravitational field of the Galilean moons, eight other flybys have been chosen from Table 5.1. Their initial state have been optimized (as done before for the previous flybys) and finally the root mean square errors have been computed with both the old and new harmonics coefficients. The new flybys are I25, I31, G1, G28, E6, E26, C9 and C10, since they are the ones with the lowest altitude (they can be expected to be more sensitive to gravity field perturbations and have greater RMSE, thus they can give more interesting results) which do not have a very high Earth's elevation angle (I32 has not been chosen for this reason, since it has an elevation angle of 51.4°).

Table 7.3 provides the variations of the initial state in J2000 coordinates as resulting from the Grid Search technique (by using the relative tolerances already used for the low-altitude flybys: for their values, the reader is referred to Section 5.4) and the gravitational field with the new spherical harmonics coefficients estimates presented in Table 6.4.

Table 7.3: Variations of the initial state in J2000 coordinates of the new eight flybys as resulting from the Grid Search technique.

Flyby ID	$\Delta \mathbf{x}_0$ **[m]**	$\Delta \mathbf{y}_0$ **[m]**	$\Delta \mathbf{z}_0$ **[m]**	$\Delta \mathbf{v}_{x_0}$ **[10^{-3} m/s]**	$\Delta \mathbf{v}_{y_0}$ **[10^{-3} m/s]**	$\Delta \mathbf{v}_{z_0}$ **[10^{-3} m/s]**
I25	-1.50	-2.00	+5.00	+4.00	+4.75	-10.75
I31	+7.00	-2.00	-7.50	-13.00	+4.25	+12.75
E6	+2.75	+1.50	-3.75	-3.50	-2.50	+4.25
E26	+3.00	-2.50	+2.50	-7.25	+5.75	-5.25
G1	-0.50	+0.50	-2.50	+0.25	-0.50	+1.50
G28	+0.00	+0.25	+0.25	+0.00	-0.25	+0.00
C9	-0.75	-1.25	+4.75	+0.25	+0.50	-1.75
C10	-0.75	-0.25	+1.25	-0.25	+0.25	-0.50

Values for RMSE_{pos} and RMSE_{vel} (before and after the Grid Searches performed with a Grid Search step-size of 0.25 m and $0.25{\cdot}10^{-3}$ m/s) are provided in Table 7.4.

Table 7.4: Values of RMSE_{pos} and RMSE_{vel} before and after the Grid Searches performed with a Grid Search step-size of 0.25 m and $0.25{\cdot}10^{-3}$ m/s.

Flyby ID	**RMSE_{pos} with old spherical harmonics [m]**	**RMSE_{pos} with new spherical harmonics [m]**	**RMSE_{vel} with old spherical harmonics [10^{-3} m/s]**	**RMSE_{vel} with new spherical harmonics [10^{-3} m/s]**
I25	3.457	3.268	12.339	11.244
I31	6.796	6.649	23.479	21.218
E6	4.649	2.499	5.727	5.537
E26	3.036	2.618	11.026	10.696
G1	0.385	0.384	0.453	0.452
G28	0.315	0.314	0.590	0.581
C9	3.618	3.414	3.297	2.659
C10	2.634	1.578	1.275	1.014

All these flybys have a RMSE greater than those of the flybys analyzed before (RMSE in Table 6.6), with the exception that G2 has a RMSE greater than that of G1 and G28, and that

C30 has one greater than that of C9 and C10. This can be explained by the fact that G2 has a closest-approach altitude of 261 km, while G1 and G28 of 835 and 809 km, respectively, and C30 of 138 km, but C9 and C10 of 418 and 535 km, according to Table 5.1. Relevant conclusions of this are treated in a stand-alone section, i.e. Section 7.3.

7.3. INTERPRETATION OF THE OBTAINED RMSE

In this section, the RMSE will be interpreted and possible causes will be addressed, so that it can be reduced in further missions. In particular, the error will be related to the three axes of the LO frame, as well as to the Earth's elevation and azimuth angles.

Figure 7.2 presents a graphical representation of the variables which are going to be analyzed, i.e. $\vec{r}_{S/C-M}$, $\vec{r}_{M-E}$, $\vec{r}_{S/C-E}$, el, az, el_M and az_M (note that the moon itself, az and az_M lie in the $X_{LO}Y_{LO}$ plane).

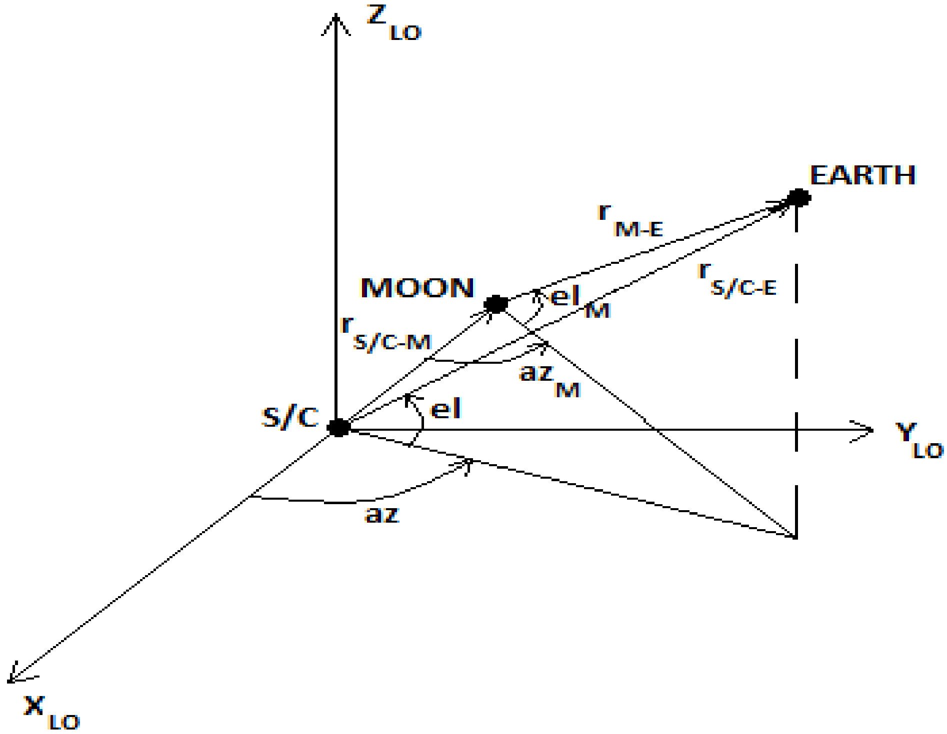

Figure 7.2: Graphical representation of the LO frame, the relative position of the spacecraft, a generic moon and the Earth, and also of the elevation and azimuth angles of the Earth as seen from the spacecraft (el, az) and the moon (el_M, az_M).

From Figure 7.2, the System of Equation (7.3) can be written:

$$\begin{cases} \vec{r}_{S/C-M} = \vec{r}_{S/C-E} - \vec{r}_{M-E} \\ \vec{r}_{S/C-E} = r_{S/C-E} \begin{pmatrix} cos(el) \cdot cos(az) \\ cos(el) \cdot sin(az) \\ sin(el) \end{pmatrix} \begin{pmatrix} \hat{X}_{LO} \\ \hat{Y}_{LO} \\ \hat{Z}_{LO} \end{pmatrix} \\ \vec{r}_{M-E} = r_{M-E} \begin{pmatrix} cos(el_M) \cdot cos(az_M) \\ cos(el_M) \cdot sin(az_M) \\ sin(el_M) \end{pmatrix} \begin{pmatrix} \hat{X}_{LO} \\ \hat{Y}_{LO} \\ \hat{Z}_{LO} \end{pmatrix} \end{cases} \tag{7.3}$$

Reference axes for az and az_M are different in sign, but this does not constitute a problem, because these angles simply measure the angular distance between two vectors exactly as indicated in Figure 7.2, so the different directions of the axes do not create an issue.

Furthermore, for every analyzed flyby, $|el_M - el| < 1 \cdot 10^{-4}$ deg and $|az_M - az| < 1 \cdot 10^{-3}$ deg, so it will be assumed that these differences are negligible.

Note that a small perturbation (e.g. an observation error) in $\vec{r}_{S/C-E}$ and/or $\vec{r}_{M-E}$ will then affect $\vec{r}_{S/C-M}$ as described in Equation (7.4):

$$\delta\vec{r}_{S/C-M} \approx \left(\delta r_{S/C-E} - \delta r_{M-E}\right) \begin{pmatrix} cos(el) \cdot cos(az) \\ cos(el) \cdot sin(az) \\ sin(el) \end{pmatrix} \begin{pmatrix} \hat{X}_{LO} \\ \hat{Y}_{LO} \\ \hat{Z}_{LO} \end{pmatrix} \tag{7.4}$$

This clearly indicates that the distance between spacecraft and moon is computed from two other observed distances (i.e. $r_{S/C-E}$ and r_{M-E}) and that observation errors on these have a specific impact on the final value of each component of $\vec{r}_{S/C-M}$, according to Equation (7.4).

Note also that for simplicity el can be assumed as constant as a first approximation, since its value changes for less than 0.1° during the flyby, since the distance between the spacecraft and the Earth is very large, while az cannot because it can vary for almost 180°, since it depends on the angular relative position of the two bodies and the spacecraft itself.

For completeness, also the expressions for the elevation el and the azimuth angle az are presented in Equations (7.5) and (7.6):

$$el = \frac{\pi}{2} - atan2\left(||\vec{r}_{SC-E} x \hat{Z}_{LO}||, \vec{r}_{SC-E} \cdot \hat{Z}_{LO}\right) \tag{7.5}$$

$$az = atan2\left(||\vec{r}_{SC-E}\ cos(el) x \hat{X}_{LO}||, \vec{r}_{SC-E}\ cos(el) \cdot \hat{X}_{LO}\right) \tag{7.6}$$

Note that the first argument of the atan2 function is the norm of a cross product, thus the product of the magnitude of the two vectors by the sinus of the angle between them, while the second is a scalar product, thus the product of the magnitude of the two vectors by the cosinus of the angle between them. Clearly, the atan2 allows for the determination of the angle between these vectors.

In particular, when the elevation angle is high, then the cross-track error ($\hat{Z}_{LO}$ direction) will be relatively large. In particular it can be seen from Table 5.1 that Callisto's flybys are the ones with the lowest Earth's elevation angles, but they are also the ones with the highest RMSE (see Table 6.6): according to Equation (7.4), it can hence be assumed that $\left(\delta r_{S/C-E} - \delta r_{M-E}\right)$ is quite large for Callisto's flybys. Please note that, in Appendix G, Figures G.1 to G.32 show the error decomposed along the three LO axes, for each of the 16 analyzed flybys.

It is now of interest to understand the relation between the directions of the error $\delta r_{S/C-M}$ and the errors in the initial Keplerian elements. The equations for the radial, along-track and cross-track errors as a function of Keplerian elements are for hyperbolic orbits (modified from page 6 of Born [2002]) given by the System of Equations (7.7):

$$\begin{cases} R \approx \left(1 - e \cdot cosh(\theta) + \frac{3}{2}\frac{e \cdot sinh(\theta) \cdot n \cdot \Delta t}{e-1}\right) \cdot \Delta a + \\ \qquad -a \cdot e \cdot sinh(\theta) \cdot \Delta\theta_0 - a \cdot \left(cosh(\theta) + sinh(\theta) \cdot \left(1 + cos(\theta)\right) \cdot sin(\theta) \cdot cos^2(\theta)\right) \cdot \Delta e \\ A \approx r\left(\Delta\omega + \Delta\theta_0 - \frac{3}{2}\frac{n \cdot \Delta t}{a \cdot (e-1)} \cdot \Delta a + cos(i) \cdot \Delta\Omega + \frac{\left(1+cos(\theta)\right) \cdot sin(\theta) \cdot cos^2(\theta)}{e} \cdot \Delta e\right) \\ C \approx r\left(sin\left(\omega + (e-1) \cdot \theta\right) \cdot \Delta i - cos\left(\omega + (e-1) \cdot \theta\right) \cdot sin(i) \cdot \Delta\Omega\right) \end{cases} \tag{7.7}$$

Table 7.5 shows the main error directions (they are the main at the first instant of propagation, as well as on average), initial Keplerian elements and initial errors on the Keplerian elements, after the performance of the Grid Search; the relation between them and the System of Equations (7.7) is highlighted through the use of colors.

Table 7.5: Main error directions (R stands for Radial, A for Along-track and C for Cross-track direction), initial Keplerian elements and initial errors on the Keplerian elements, after the performance of the Grid Search. R is red, A is blue, C is green, the combination of R and A is purple, the one of R and C is yellow, while the one of A and C is cyan.

Flyby ID	Main error axis	a_0 [km]	e_0 -	i_0 [deg]	ω_0 [deg]	Ω_0 [deg]	θ_0 [deg]	Δa_0 [mm]	Δe_0 [10^{-6}]	Δi_0 [10^{-6} deg]	$\Delta\omega_0$ [10^{-6} deg]	$\Delta\Omega_0$ [10^{-6} deg]	$\Delta\theta_0$ [10^{-6} deg]
I33	C	-82	24	127	240	235	282	12	2	136	10	16	1
I0	A	-27	102	17	186	333	290	0.04	4	1	10	9	0.9
I31	R,A,C	-134	16	90	115	58	282	67	44	157	121	182	68
I25	R,A	-106	21	90	250	236	284	42	55	14	100	0.9	62
E12	A	-88	21	22	164	338	278	25	65	2	20	101	47
E15	R,A	-81	51	29	154	31	294	9	4	1	0.8	7	6
E26	C	-26	75	123	240	236	281	4	25	140	13	23	2
E6	R,A,C	-107	21	150	216	213	281	27	35	79	33	100	32
G2	R,C	-174	18	85	112	75	274	8	0.3	12	0.8	7	0.1
G29	R,A,C	-92	55	73	115	58	281	2	4	3	0.1	3	0.6
G28	R,A,C	-81	44	143	229	209	277	3	1	5	5	6	0.2
G1	C	-179	20	40	116	54	276	0.3	6	30	36	39	3
C30	C	-81	32	153	157	148	272	2	22	54	367	419	4
C22	C	-103	47	155	175	183	276	3	0.5	2	15	17	0.1
C9	C	-115	26	156	220	175	272	2	5	55	110	123	1
C10	R,A,C	-114	27	29	131	5	272	5	14	19	36	44	4

For example, flyby I33 has a great error in the cross-track direction, because it has a high value of Δi_0, which influences exactly that direction, according to the System of Equations (7.7). Flyby I0 has the main error in the along-track direction, since it has small values of semi-major axis and inclination, but relevant $\Delta\omega_0$ and $\Delta\Omega_0$. The reader will notice that $\Delta\Omega_0$ of course influences also the cross-track error, but this latter is proportional to the sinus of the inclination, while the along-track one is proportional to its cosinus and of course if the value of the inclination is low as in this case, the error will mostly be in the along-track direction. By applying this reasoning to every flyby, Table 7.5 has been filled in.

Note from Table 7.5 that all the Ganymede's and Callisto's flybys have a relevant error in the cross-track direction, in fact the greatest variation in the initial state after the Grid Searches is always in this direction. This is due to the fact that these moons possess a great sphere of influence and thus at the first instant the distance between their center of mass and the spacecraft is high. In this way, the along-track error would be relevant as well according to the System of Equations (7.7), however these flybys are also characterized by a relatively high Δi_0, while $\Delta\theta_0$, Δa_0 and Δe_0 are quite low.

Figures (7.3) to (7.6) show the RMSE for position and velocity with respect to the closest-approach altitude and the Earth's elevation angle.

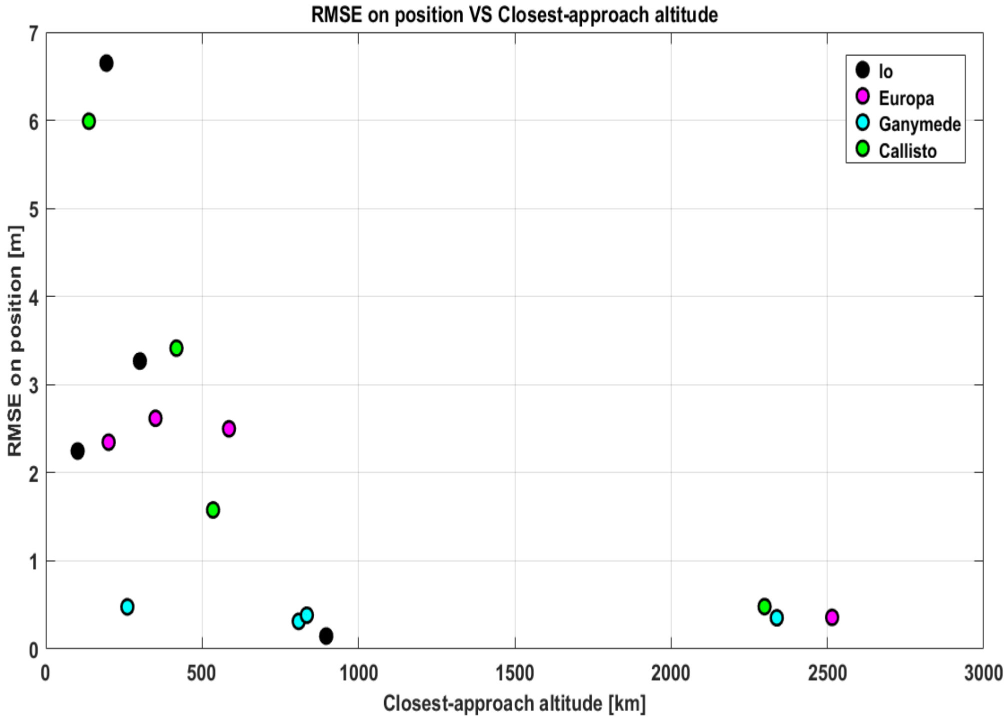

Figure 7.3: Graphical representation of the RMSE on position as a function of the closest-approach altitude.

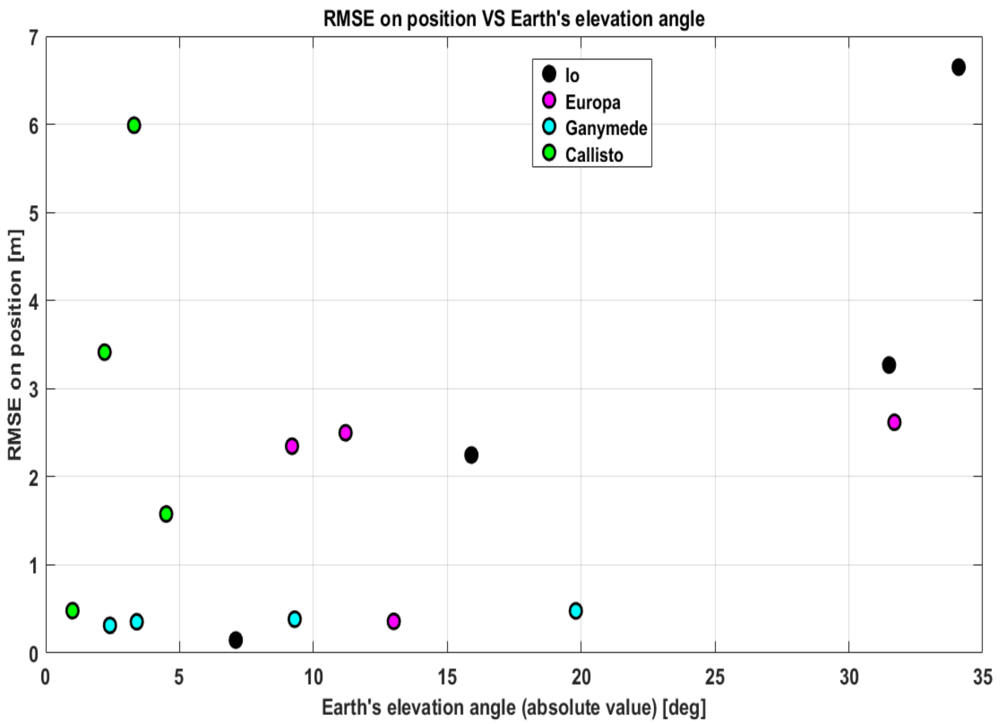

Figure 7.4: Graphical representation of the RMSE on position as a function of the Earth's elevation angle.

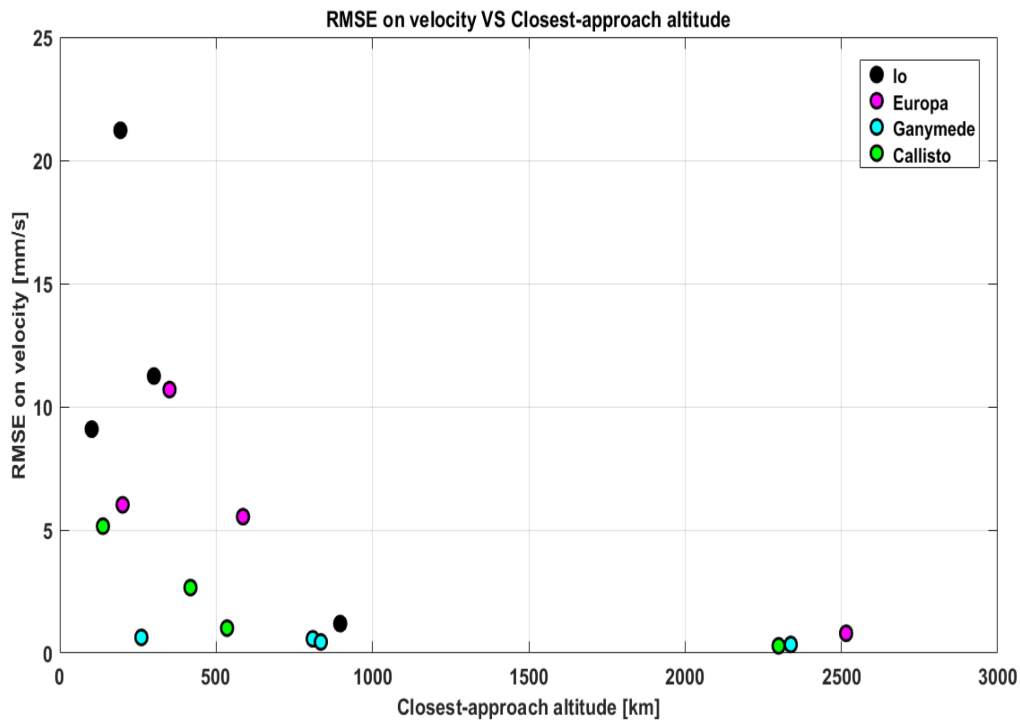

Figure 7.5: Graphical representation of the RMSE on velocity as a function of the closest-approach altitude.

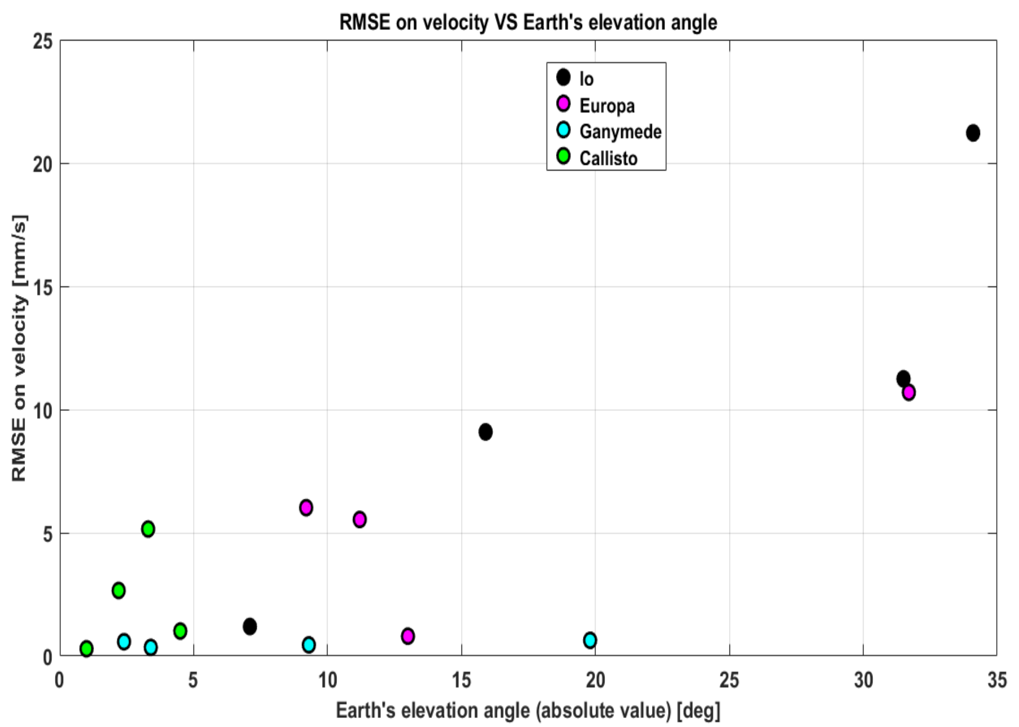

Figure 7.6: Graphical representation of the RMSE on velocity as a function of the Earth's elevation angle.

It can thus be realized that in general a lower closest-approach altitude (by comparing flybys about the same moon) implies a higher error, but there are some exceptions for which this does not happen. However, in all these cases the Earth's elevation angle for the flyby with a higher closest-approach altitude is always larger, thus its observation data are less accurate: high values of elevation can lead to a very low variation of the spacecraft's distance from Earth, thus the acquisition data made through Doppler effect analyses may be not so accurate.

It is thus shown how the Earth's elevation angle is a very important parameter which does play a fundamental role in the final accuracy of the trajectory. For this reason, it is pointed out that, in order to limit the final error on the trajectory already in the design phase of a mission, it is of great importance not only limit the minimum closest-approach altitude, but also the maximum Earth's elevation angle. As can be seen in Figures 7.3 to 7.6, it is indeed possible to have a flyby with a better accuracy than one with a slightly higher closest-approach altitude if the elevation angle of the former is lower.

7.4. SYNOPSIS: ANALYSIS OF THE RESULTS

The new spherical harmonics coefficients lead to a small variation in the estimate of hydrostaticity of the Galilean moons, which have been proven to be in an almost perfect hydrostatic equilibrium. The estimated harmonics have been also proven to perform better than the literature ones for eight other flybys too. Then, the error has been related analytically to the three axes of the LO frame by means of the Systems of Equations (7.4) and (7.7). A relevant conclusion is that the propagation of a spacecraft's trajectory about bodies with a great sphere of influence are more subjected to errors in the along-track and cross-track directions; furthermore if Δi_0 is relatively high, then the latter outclasses the former.

Moreover, the Earth's elevation angle has been shown to be an important parameter which, for flybys with similar altitudes, can determine which of those will have the best data accuracy, i.e. the one with the lowest elevation angle.

8
Validation

In this chapter, the validation of the MATLAB (version R2016b) script by means of the already validated ASTOS software (version 9.0.0) is presented.

8.1. Validation of the MATLAB script with ASTOS

A test-case scenario is chosen and its results, in terms of final state, will be compared between the two softwares and of course the JPL ephemerides. The test-case scenario is flyby I33, since it is the one with the lowest altitude, thus the one in which the gravitational perturbations will be relatively high. Please note that by comparing for example an unperturbed two-body problem, it would not be possible to deduce as much as in a perturbed case, in which instead also the disturbances are taken into account.

Unfortunately ASTOS does not support the possibility of using the spherical harmonics of a non-central body, i.e. the Jovian J_2 cannot be used.

By using Io's known values of J_4, $C_{3,1}$, $C_{3,3}$, $C_{4,2}$, $C_{4,4}$, the new ones of J_2 and $C_{2,2}$, along with the estimated $S_{2,1}$, $C_{3,2}$ and $C_{4,1}$ (from Section 6.3) and the corresponding new initial state (from Section 6.4), the I33 flyby can be simulated in both MATLAB and ASTOS and the final state can finally be checked. In order to have the same inputs, an ODE45 (Runge-Kutta 4(5)) with a relative tolerance of $1 \cdot 10^{-10}$ has been used, since ASTOS does not allow lower relative tolerances, neither an Adams-Bashforth-Moulton PECE integrator. Note that this, along with the neglect of the Jovian J_2, will result in a loss of accuracy, but this is of no concern now, since the purpose is just the comparison of the two softwares.

The final state produced at the end of the propagation by ASTOS is described by the System of Equations (8.1):

$$\begin{cases} x_A = -660555.9381926542 \text{ m} \\ y_A = -6547759.5055887220 \text{ m} \\ z_A = -4244934.660600572 \text{ m} \\ v_{x_A} = -2316.8489620832 \text{ m/s} \\ v_{y_A} = -7624.6180913323 \text{ m/s} \\ v_{z_A} = -3220.1063463816 \text{ m/s} \end{cases} \tag{8.1}$$

The final state furnished by the MATLAB script is presented in the System of Equations (8.2):

$$\begin{cases} x_M = -660555.937819105 \text{ m} \\ y_M = -6547759.50496799 \text{ m} \\ z_M = -4244934.66035191 \text{ m} \\ v_{x_M} = -2316.84896189603 \text{ m/s} \\ v_{y_M} = -7624.61809136641 \text{ m/s} \\ v_{z_M} = -3220.10634640675 \text{ m/s} \end{cases} \tag{8.2}$$

The absolute and relative differences between the MATLAB final state and the ASTOS one are presented in Systems of Equations (8.3) and (8.4)

$$\begin{cases} \Delta x \approx 3.7 \cdot 10^{-4} \text{ m} \\ \Delta y \approx 6.2 \cdot 10^{-4} \text{ m} \\ \Delta z \approx 2.5 \cdot 10^{-4} \text{ m} \\ \Delta v_x \approx 1.9 \cdot 10^{-7} \text{ m/s} \\ \Delta v_y \approx -3.4 \cdot 10^{-8} \text{ m/s} \\ \Delta v_z \approx -2.5 \cdot 10^{-8} \text{ m/s} \end{cases} \tag{8.3}$$

$$\begin{cases} \frac{\Delta x}{x_A} \approx -5.7 \cdot 10^{-10} \\ \frac{\Delta y}{y_A} \approx -9.5 \cdot 10^{-11} \\ \frac{\Delta z}{z_A} \approx -5.9 \cdot 10^{-11} \\ \frac{\Delta v_x}{v_{x_A}} \approx -8.1 \cdot 10^{-11} \\ \frac{\Delta v_y}{v_{y_A}} \approx 4.5 \cdot 10^{-12} \\ \frac{\Delta v_z}{v_{z_A}} \approx 7.8 \cdot 10^{-12} \end{cases} \tag{8.4}$$

It can be concluded that, since the differences in the norm of the final Galileo position and velocity are only $7.7 \cdot 10^{-4}$ m and $1.9 \cdot 10^{-7}$ m/s (definitely negligible for the aim of this research), the MATLAB script is validated.

Note that ASTOS 9.0.0 also allows for the usage of solar radiation pressure and relativistic effects, which have been tested for this flyby with the worst-case scenario parameters described in Subsections 3.6.3 and 3.6.6: in ASTOS, both of them reported a variation of less than $1 \cdot 10^{-2}$ m and $1 \cdot 10^{-5}$ m/s respectively for the norms of the final position and velocity. Hence, it is a clear confirmation of the negligibility of the two greatest non-considered perturbations.

8.2. SYNOPSIS: VALIDATION OF THE SCRIPT

The comparison of the I33 flyby simulated with both MATLAB and ASTOS 9.0.0 allowed to conclude that the MATLAB script is validated, since the difference between the norms of the final Galileo's position and velocity are only $7.7 \cdot 10^{-4}$ m and $1.9 \cdot 10^{-7}$ m/s. Furthermore, since the addition of general relativity and solar radiation pressure in the software developed by Astos Solutions GmbH has led to negligible variations of the final state, ASTOS proved the negligibility of these perturbations.

9

Conclusions and recommendations

In this chapter, the conclusions will be treated: in particular, final considerations about what has been done will be presented, and possible consequences, also for real life missions, will be identified. Finally, recommendations to the reader will be provided.

9.1. Final considerations

Two flybys per moon have been chosen to be analyzed, depending on their closest-approach altitude and Earth's elevation angle: I33, I0, E12, E15, G2, G29, C30 and C22. The equations of motion in equinoctial elements of the perturbed two-body problem have been propagated in the pseudo-inertial J2000 reference frame centered in the Galilean moon about which the spacecraft is flying, by means of the ODE113 MATLAB integrator with a relative tolerance of about $2 \cdot 10^{-14}$. The perturbations used are the third-body perturbation of Sun, Jupiter and the three moons different from the central one, but also the Jovian J_2 and all the available central body's spherical harmonics.

The initial state and the spherical harmonics have been optimized in such a way that the minimum root mean square error with respect to the JPL ephemerides is obtained. Furthermore the harmonics coefficients $S_{2,1}$, $C_{3,2}$ and $C_{4,1}$ of Io, $C_{3,2}$, $S_{3,3}$ and J_4 of Europa, J_9 of Ganymede, $C_{3,2}$ and $S_{3,2}$ of Callisto have been estimated ex novo. The updated values of J_2 and $J_{2,2}$ of Io, Europa and Callisto led to a corresponding determination of their hydrostaticity, for which the inner moon resulted to be less hydrostatic, while the other two to be more hydrostatic than previously thought. Note however that all the four Galilean moons are almost perfectly hydrostatic (slightly more than the Moon, and much more than planets like Mars, Earth or Jupiter) and hence that the internal stresses are mostly released as shape changes during their orbits about Jupiter.

Eight other flybys (I25, I31, G1, G28, E6, E26, C9 and C10) have been studied and have shown that the new harmonics perform better than the old for the selected cases. Furthermore, the magnitude of the error on the position of the spacecraft with respect to the moon depends on the accuracy of the position of these two bodies with respect to the Earth, while the magnitude of its components along the LO axes depends on the elevation and azimuth at the observation time. Note that it is possible to relate the radial, along-track and cross-track errors to specific errors in the Keplerian elements; it is highlighted that Ganymede and Callisto which are characterized by a large sphere of influence are much more likely to have high errors in the along-track and cross-track directions. Two parameters turned out to be fundamental for the accuracy of a flyby trajectory, i.e. the closest-approach altitude (higher altitude implies more accuracy) and the Earth's elevation angle (higher elevation angle implies less accuracy). It can finally be stated that, in order to keep a certain accuracy already from the design of a flyby mission, it is not only important to limit the minimum closest-approach altitude but also the maximum allowed Earth's elevation angle, since this latter parameter turned out to be very important when flybys with similar altitudes are compared.

9.2. RECOMMENDATIONS

Those who are interested in the expansion of this work may want to analyze the remaining flybys and find values of the Galilean moons' spherical harmonics coefficients by using the complete set of flybys, in order to get an even more precise estimation. It is pointed out that the moons' ephemerides used for the determination of the Galileo's trajectory are subjected to an error which can reach 9 meters (NASA [2004]), while a new file with a much better accuracy (0.5 m, according to NASA [2013]) has been recently made available. In order to have a very precise trajectory of the spacecraft and thus be able to extrapolate more accurate information about the gravity field of these moons, it is thus suggested to ask directly to JPL (or through a cooperation with it) the observation data relative to the spacecraft's state with respect to Earth and combine it with the new ephemerides of the Galilean moons. It is possible that this will result in an analysis so precise that other perturbations neglected in this research, like relativistic effects and solar radiation pressure, may start to play a relevant role. In this way the Callisto flybys in particular would see their root mean square errors decreased by a considerable factor, since now they are about one order of magnitude greater than the reachable 0.5 meters.

A

Transformation between J2000 and PCPF

This appendix presents the transformation used in Chapter 3 needed to pass from the J2000 to the PCPF frame and vice-versa.

Accelerations in J2000 and PCPF frames are defined as in Equations (A.1) and (A.2):

$$\vec{a}_{J2000} = \begin{pmatrix} a_{J2000_x} \\ a_{J2000_y} \\ a_{J2000_z} \end{pmatrix} \tag{A.1}$$

$$\vec{a}_{PCPF} = \begin{pmatrix} a_{PCPF_x} \\ a_{PCPF_y} \\ a_{PCPF_z} \end{pmatrix} \tag{A.2}$$

According to pages 63-64 of Bao and Tsui [2000], a rotation matrix can be defined as in Equation (A.3):

$$R_{\tau\delta\alpha} = R_\tau R_\delta R_\alpha =$$
$$= \begin{bmatrix} cos(\tau) & -sin(\tau) & 0 \\ sin(\tau) & cos(\tau) & 0 \\ 0 & 0 & 1 \end{bmatrix} \begin{bmatrix} 1 & 0 & 0 \\ 0 & cos(\frac{pi}{2}-\delta) & -sin(\frac{pi}{2}-\delta) \\ 0 & sin(\frac{pi}{2}-\delta) & cos(\frac{pi}{2}-\delta) \end{bmatrix} \begin{bmatrix} cos(\frac{pi}{2}+\alpha) & -sin(\frac{pi}{2}+\alpha) & 0 \\ sin(\frac{pi}{2}+\alpha) & cos(\frac{pi}{2}+\alpha) & 0 \\ 0 & 0 & 1 \end{bmatrix} \tag{A.3}$$

where R_τ, R_δ and R_α are the matrices which respectively represent a rotation of the sidereal time angle about the Z-axis, the declination about the X-axis, and the right ascension about the Z-axis.

It can finally be stated that:

$$\vec{a}_{PCPF} = R_{\tau\delta\alpha}\vec{a}_{J2000} \tag{A.4}$$

Of course, also the inverse transformation can be performed, as described in Equation (A.5):

$$\vec{a}_{J2000} = R^{-1}_{\tau\delta\alpha}\vec{a}_{PCPF} \tag{A.5}$$

Please note that values for τ, δ, α can be found in Seidelmann et al. [2007].

B

Transformation between J2000 and LO

This appendix presents the transformation used in Chapter 3 needed to pass from the J2000 to the LO frame and vice-versa.

Accelerations in J2000 and LO frames are defined as in Equations (B.1) and (B.2):

$$\vec{a}_{J2000} = \begin{pmatrix} a_{J2000_x} \\ a_{J2000_y} \\ a_{J2000_z} \end{pmatrix} \tag{B.1}$$

$$\vec{a}_{LO} = \begin{pmatrix} a_{LO_x} \\ a_{LO_y} \\ a_{LO_z} \end{pmatrix} \tag{B.2}$$

According to page 59 of Bao and Tsui [2000], a rotation matrix can be defined as in Equation (B.3):

$$R_{ui\Omega} = R_u R_i R_\Omega = \begin{bmatrix} cos(u) & -sin(u) & 0 \\ sin(u) & cos(u) & 0 \\ 0 & 0 & 1 \end{bmatrix} \begin{bmatrix} 1 & 0 & 0 \\ 0 & cos(i) & -sin(i) \\ 0 & sin(i) & cos(i) \end{bmatrix} \begin{bmatrix} cos(\Omega) & -sin(\Omega) & 0 \\ sin(\Omega) & cos(\Omega) & 0 \\ 0 & 0 & 1 \end{bmatrix} \tag{B.3}$$

where R_Ω, R_i and R_u are the matrices which respectively represent a rotation of the right ascension of the ascending node about the Z-axis, the inclination about the X-axis, and the argument of latitude (sum of argument of pericenter and true anomaly) about the Z-axis.

It can finally be stated that:

$$\vec{a}_{LO} = R_{ui\Omega}\vec{a}_{J2000} \tag{B.4}$$

Of course, also the inverse transformation can be performed, as described in Equation (B.5):

$$\vec{a}_{J2000} = R^{-1}_{ui\Omega}\vec{a}_{LO} \tag{B.5}$$

C
Zonal Harmonics

This appendix presents the equations needed to get the final expression of the maximum perturbing acceleration due to zonal harmonics.

By applying the condition of a zero order ($m = 0$) in Equation (3.21), it holds true that the magnitude of the perturbing acceleration due to a zonal harmonic of degree n is given by Equation (C.1) (where it has been written $P_{n,m}$ instead of $P_{n,m}(sin\phi)$ for the sake of the length of the expression):

$$a_{MD_{zonal}} =$$
$$= \sqrt{\left((n+1)P_n cos\phi + P_{n,1} sin\phi\right)^2 + \left((n+1)P_n sin\phi - P_{n,1} cos\phi\right)^2}\,\mu_{PB} R_{PB}^n \left(\frac{1}{r_{S/C-PB}^{n+2}} - \frac{1}{r_{PB-CB}^{n+2}}\right)|J_n| =$$
$$= \sqrt{\left((n+1)P_n\right)^2 + \left(P_{n,1}\right)^2}\,\mu_{PB} R_{PB}^n \left(\frac{1}{r_{S/C-PB}^{n+2}} - \frac{1}{r_{PB-CB}^{n+2}}\right)|J_n| \tag{C.1}$$

Note that there is no dependency on the longitude of the spacecraft.

The function $\sqrt{\left((n+1)P_n\right)^2 + \left(P_{n,1}\right)^2}$ always has a maximum at $\phi = \pm\frac{\pi}{2}$, where $|\sin\phi|$ is 1, independently of the value of n. Please note that this means that each zonal harmonic has its greatest effect at the poles.

Since $P_n(1) = 1$ and $P_{n,1}(1) = 0\ \forall n$, it can be stated that the maximum acceleration due to a zonal harmonic is given by Equation (C.2):

$$a_{MD_{zonalmax}} = (n+1)\mu_{PB} R_{PB}^n \left(\frac{1}{r_{S/C-PB}^{n+2}} - \frac{1}{r_{PB-CB}^{n+2}}\right)|J_n| \tag{C.2}$$

D

Tesseral Harmonics

This appendix presents the equations needed to get the final expression of the maximum perturbing acceleration due to tesseral harmonics.

Since the acceleration $a_{MD_{tesseral}}$ is defined as the gradient of the perturbing gravitational potential, it can be written as in Equation (D.1)

$$\vec{a}_{MD_{tesseral}} = \vec{\nabla} U^* = \frac{\partial U^*}{\partial r}\hat{r} + \frac{1}{r}\frac{\partial U^*}{\partial \phi}\hat{\phi} + \frac{1}{r \cdot cos\phi}\frac{\partial U^*}{\partial \lambda}\hat{\lambda} \tag{D.1}$$

and thus that

$$a_{MD_{tesseral}} = \sqrt{\left(\frac{\partial U^*}{\partial r}\right)^2 + \frac{1}{r^2}\left(\frac{\partial U^*}{\partial \phi}\right)^2 + \frac{1}{r^2 \cdot cos^2\phi}\left(\frac{\partial U^*}{\partial \lambda}\right)^2} \tag{D.2}$$

By using Equation (3.22) and writing $P_{n,m}$ instead of $P_{n,m}(sin\phi)$ for the sake of the length of the expression, it holds true that:

$$\begin{cases} \left(\frac{\partial U^*}{\partial r}\right)^2 = \frac{\mu^2 R^{2n}}{r^{2n+4}}\left((n+1)P_{n,m}\right)^2\left(C_{n,m}cos(m\lambda) + S_{n,m}sin(m\lambda)\right)^2 \\ \frac{1}{r^2}\left(\frac{\partial U^*}{\partial \phi}\right)^2 = \frac{\mu^2 R^{2n}}{r^{2n+4}}\left(P_{n,m+1} - m \cdot tan\phi \cdot P_{n,m}\right)^2\left(C_{n,m}cos(m\lambda) + S_{n,m}sin(m\lambda)\right)^2 \\ \frac{1}{r^2 \cdot cos^2\phi}\left(\frac{\partial U^*}{\partial \lambda}\right)^2 = \frac{\mu^2 R^{2n}}{r^{2n+4}}\frac{1}{cos^2\phi}m^2 P^2_{n,m}\left(S_{n,m}cos(m\lambda) - C_{n,m}sin(m\lambda)\right)^2 \end{cases} \tag{D.3}$$

By substituting Equation (D.3) in Equation (D.1) and by considering both direct and indirect terms, it results that:

$$a_{MD_{tesseral}} =$$

$$= \sqrt{f\left(C_{n,m}cos(m\lambda) + S_{n,m}sin(m\lambda)\right)^2 + g\left(S_{n,m}cos(m\lambda) - C_{n,m}sin(m\lambda)\right)^2}\,\mu_{PB} R^n_{PB}\left(\frac{1}{r^{n+2}_{S/C-PB}} - \frac{1}{r^{n+2}_{PB-CB}}\right) \tag{D.4}$$

with $f = \left((n+1)P_{n,m}\right)^2 + \left(P_{n,m+1} - m \cdot tan\phi \cdot P_{n,m}\right)^2$ and $g = \frac{1}{cos^2\phi}m^2 P^2_{n,m}$.

Since f and g are always positive, it is now desired to maximize the $a_{MD_{tesseral}}$ with respect to the longitude. By equalizing its derivative to zero, it is suddenly shown that the radicand has a maximum at $\lambda_{a_{max}} = \frac{1}{m}atan\left(\frac{S_{n,m}}{C_{n,m}}\right) + \frac{2k}{m}\pi$, with $k \in \mathbb{Z}$. Please note that this leads to the annulment of the term which multiplies g and to the reduction of $\left(C_{n,m}cos(m\lambda_{a_{max}})+S_{n,m}sin(m\lambda_{a_{max}})\right)^2$ to $\left(C_{n,m}^2+S_{n,m}^2\right)$.

By using $|J_{n,m}|=\sqrt{C_{n,m}^2+S_{n,m}^2}$, it can be finally stated that:

$$a_{MD_{tesseral max}}=\sqrt{\left((n+1)P_{n,m}\right)^2+\left(P_{n,m+1}-m\cdot tan\phi_{a_{max}}\cdot P_{n,m}\right)^2}\,\mu_{PB}R_{PB}^n\left(\frac{1}{r_{S/C-PB}^{n+2}}-\frac{1}{r_{PB-CB}^{n+2}}\right)|J_{n,m}| \tag{D.5}$$

where of course $P_{n,m}$ indicates $P_{n,m}\left(sin\phi_{a_{max}}\right)$.

Notice that $\phi_{a_{max}}$ can be found by maximizing the radical in Equation (D.5), and so by equalizing its derivative with respect to ϕ to zero, as done in Equation (D.6):

$$\phi_{a_{max}}=\phi\,\Big| \\ (n+1)P_{n,m}\frac{dP_{n,m}}{dsin\phi}cos\phi+\left(P_{n,m+1}-m\cdot tan\phi\cdot P_{n,m}\right)\left(\frac{dP_{n,m+1}}{dsin\phi}cos\phi-m\left((1+tan^2\phi)P_{n,m}+\right.\right. \\ \left.\left.+\frac{dP_{n,m}}{dsin\phi}sin\phi\right)\right)=0 \tag{D.6}$$

E

Variation of Galileo's distance from Earth

This appendix presents figures which show the variation of the distance between the Galileo spacecraft and the Earth.

The Doppler effect takes advantage of the change in distance between the target and the observer; for this reason, Figures E.1 to E.8 present the distance between Galileo and Earth as a function of time.

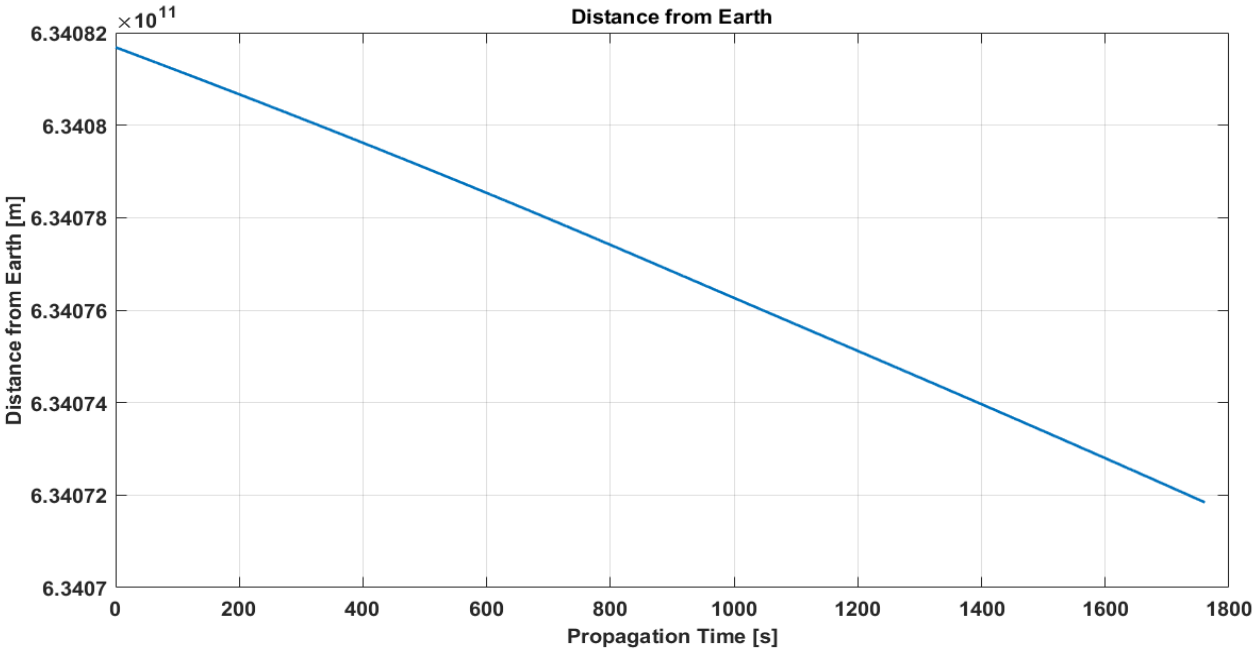

Figure E.1: Distance between Galileo and the Earth, during the flyby I33.

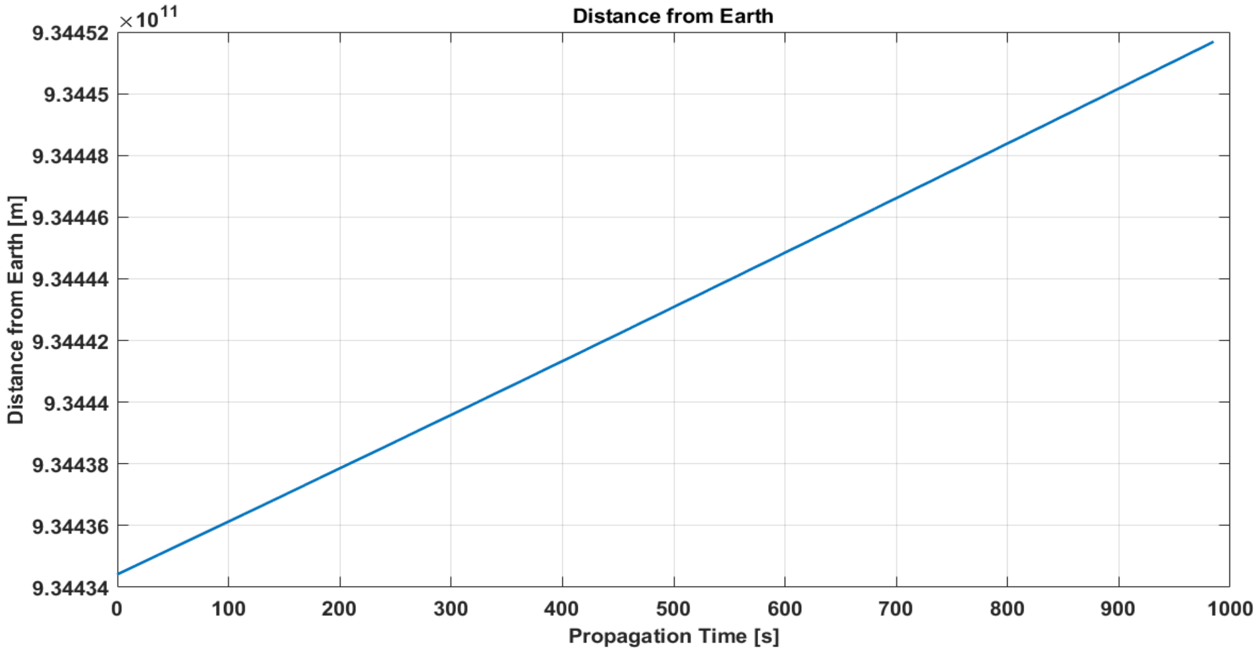

Figure E.2: Distance between Galileo and the Earth, during the flyby I0.

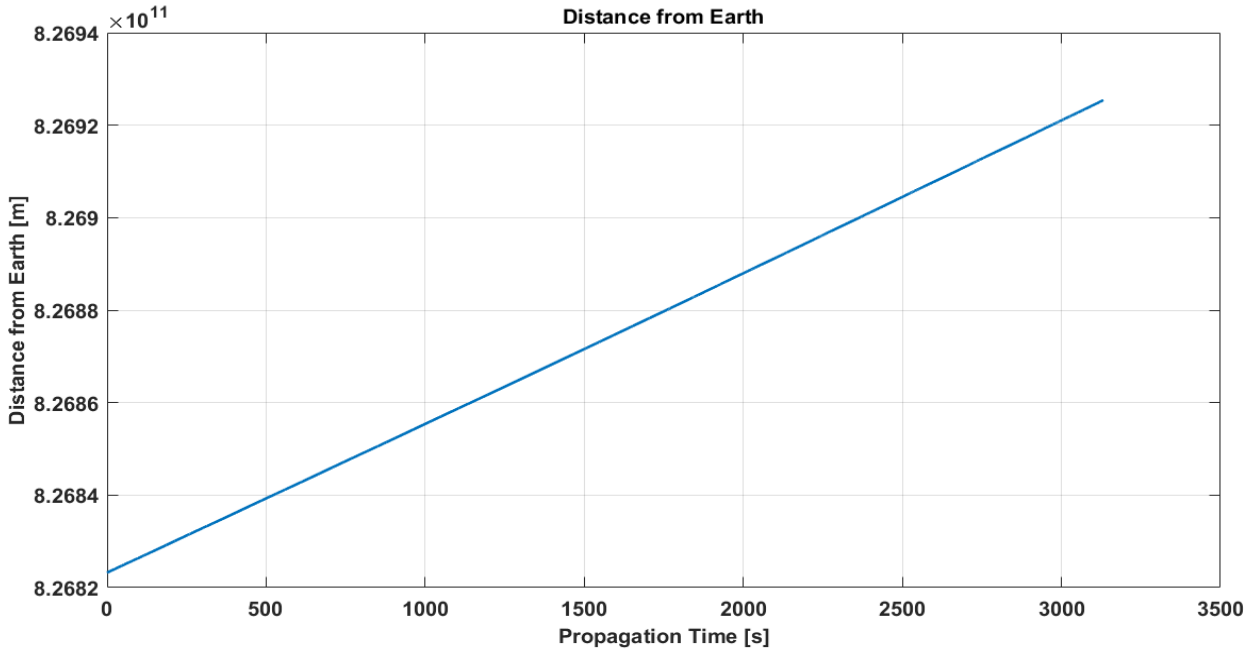

Figure E.3: Distance between Galileo and the Earth, during the flyby E12.

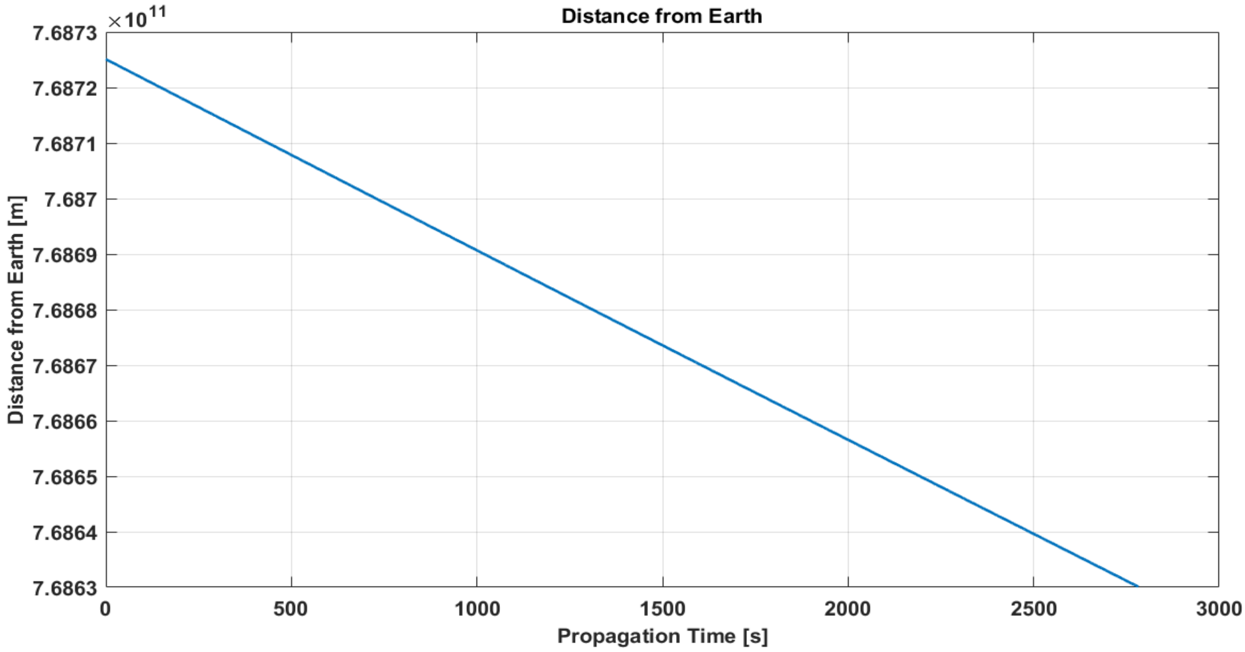

Figure E.4: Distance between Galileo and the Earth, during the flyby E15.

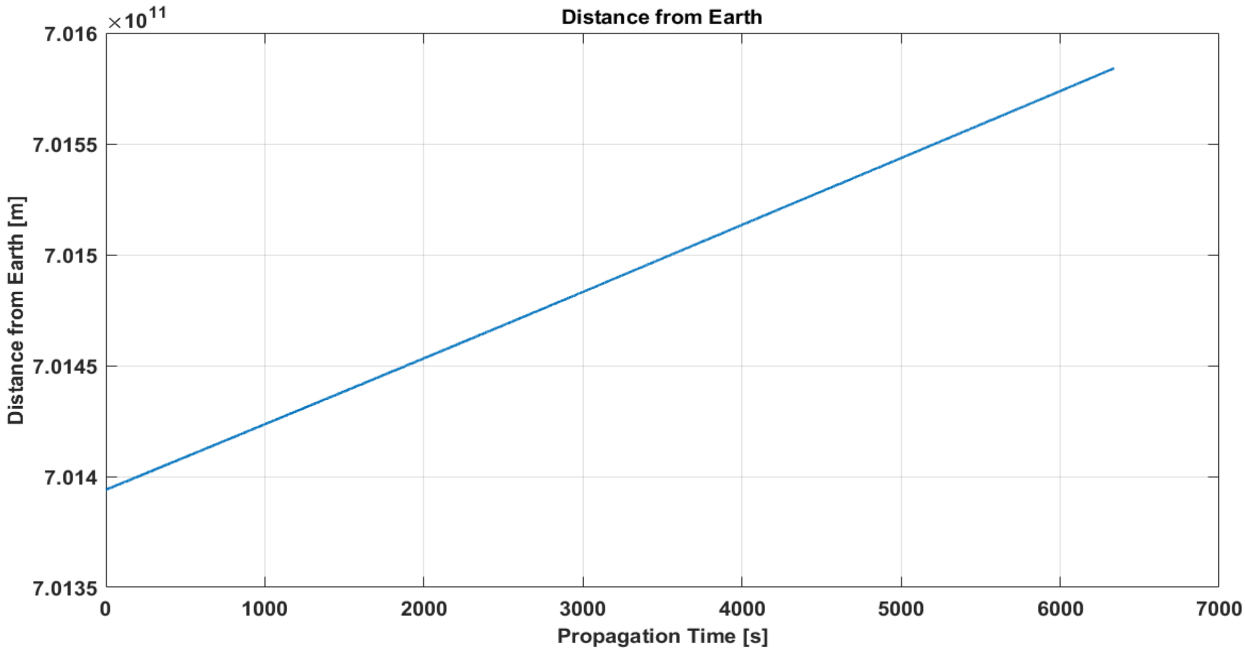

Figure E.5: Distance between Galileo and the Earth, during the flyby G2.

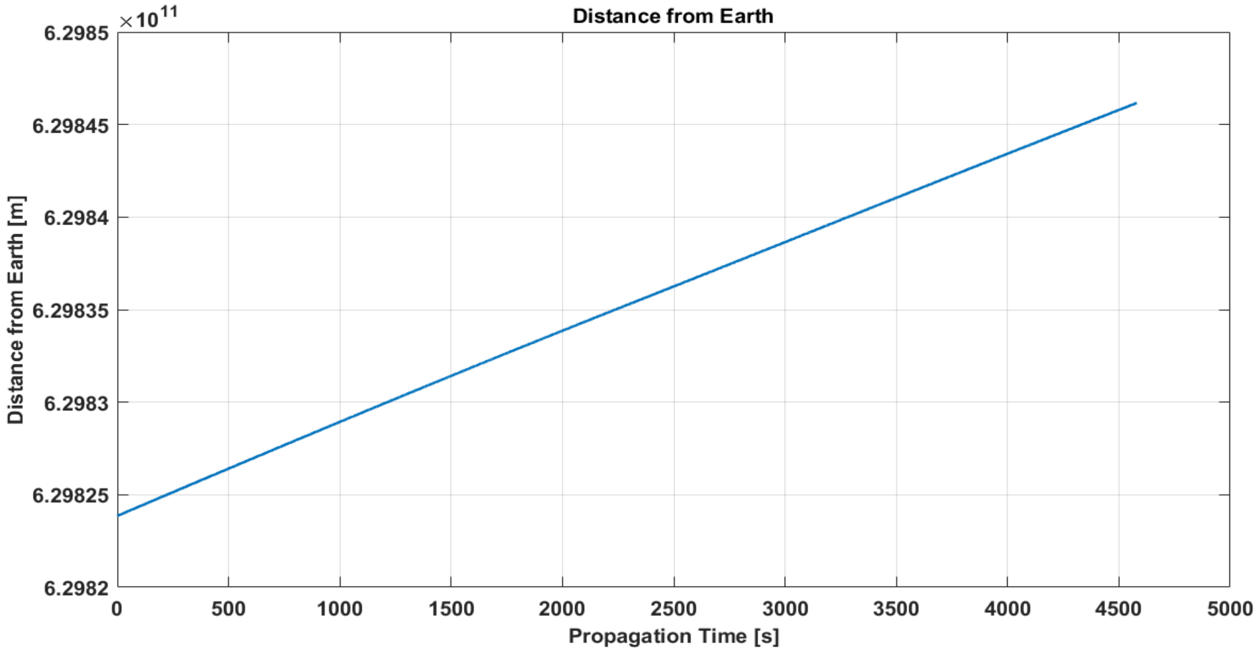

Figure E.6: Distance between Galileo and the Earth, during the flyby G29.

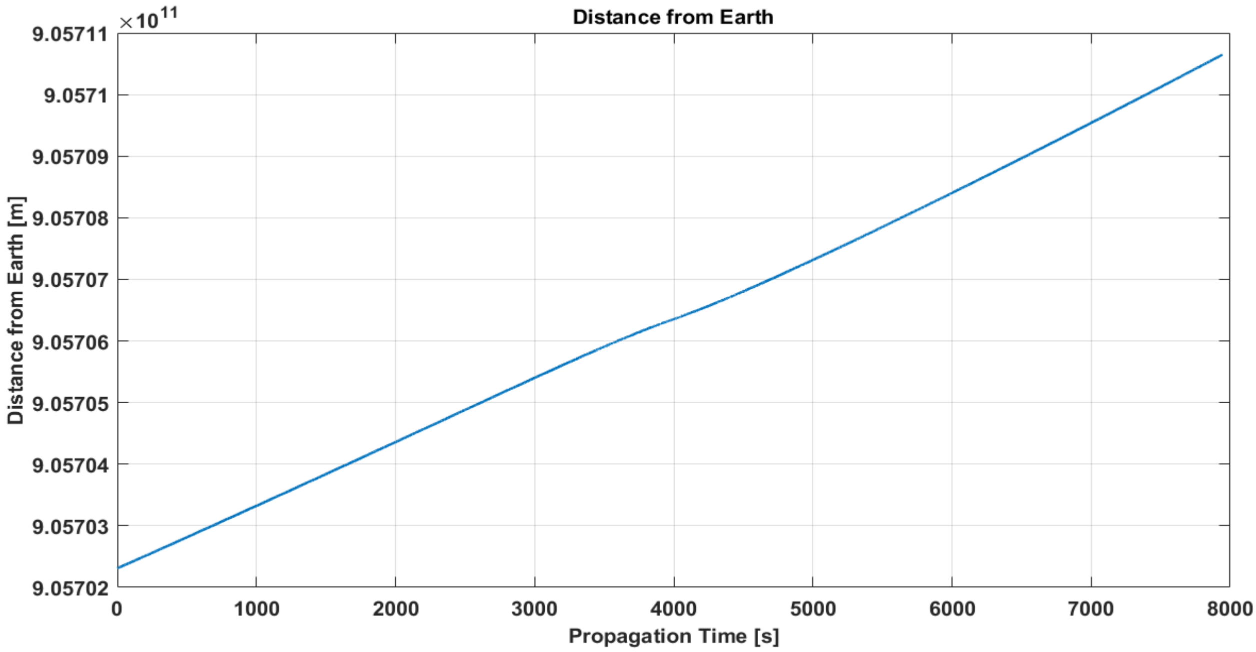

Figure E.7: Distance between Galileo and the Earth, during the flyby C30.

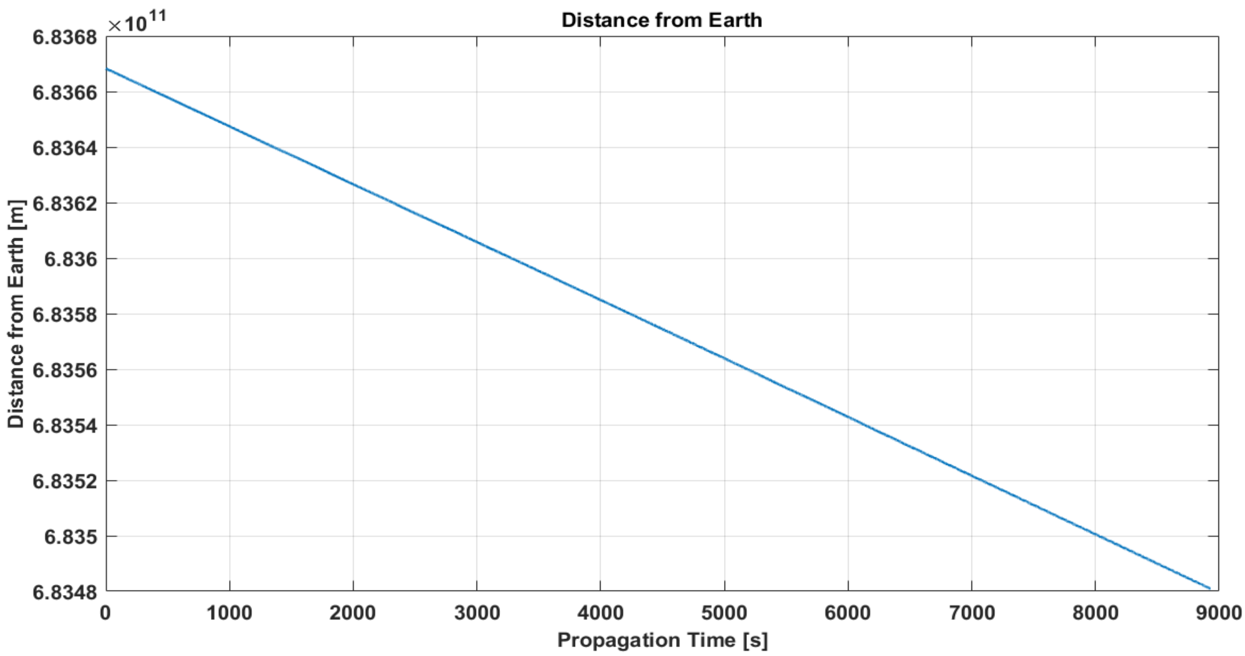

Figure E.8: Distance between Galileo and the Earth, during the flyby C22.

F

Spherical Harmonics

This appendix shows the nominal spherical harmonics, with the complete number of decimal places as found in literature.

They are shown in Table F.1:

Table F.1: Literature values for some nominal spherical harmonics, evaluated new values for them (in cyan) and estimated values for other new ones (in yellow) as resulting from the Grid Search technique are presented. The variation between the new and the old values are also shown.

Moon	Old spherical harmonics [10^{-6}]	New spherical harmonics [10^{-6}]	Variation of spherical harmonics [10^{-6}]
Io	J_2 = 1845.9	J_2 = 1842.6	ΔJ_2 = -3.3
	$C_{2,1}$ = N.A. (0.0)	$C_{2,1}$ = 0.0	$\Delta C_{2,1}$ = 0.0
	$S_{2,1}$ = N.A. (0.0)	$S_{2,1}$ = 0.8	$\Delta S_{2,1}$ = 0.8
	$C_{2,2}$ = 553.7	$C_{2,2}$ = 552.5	$\Delta C_{2,2}$ = -1.2
	$S_{2,2}$ = N.A. (0.0)	$S_{2,2}$ = 0.0	$\Delta S_{2,2}$ = 0.0
	J_3 = N.A. (0.0)	J_3 = 0.0	ΔJ_3 = 0.0
	$C_{3,1}$ = -1.216867078471049	$C_{3,1}$ = -1.216867078471049	$\Delta C_{3,1}$ = 0.0
	$S_{3,1}$ = N.A. (0.0)	$S_{3,1}$ = 0.0	$\Delta S_{3,1}$ = 0.0
	$C_{3,2}$ = N.A. (0.0)	$C_{3,2}$ = -0.4	$\Delta C_{3,2}$ = -0.4
	$S_{3,2}$ = N.A. (0.0)	$S_{3,2}$ = 0.0	$\Delta S_{3,2}$ = 0.0
	$C_{3,3}$ = 0.2028203347656355	$C_{3,3}$ = 0.2028203347656355	$\Delta C_{3,3}$ = 0.0
	$S_{3,3}$ = N.A. (0.0)	$S_{3,3}$ = 0.0	$\Delta S_{3,3}$ = 0.0
	J_4 = -9.2778	J_4 = -9.2778	ΔJ_4 = 0.0
	$C_{4,1}$ = N.A. (0.0)	$C_{4,1}$ = -0.5	$\Delta C_{4,1}$ = -0.5
	$S_{4,1}$ = N.A. (0.0)	$S_{4,1}$ = 0.0	$\Delta S_{4,1}$ = 0.0
	$C_{4,2}$ = -0.7862685829282511	$C_{4,2}$ = -0.7862685829282511	$\Delta C_{4,2}$ = 0.0
	$S_{4,2}$ = N.A. (0.0)	$S_{4,2}$ = 0.0	$\Delta S_{4,2}$ = 0.0
	$C_{4,3}$ = N.A. (0.0)	$C_{4,3}$ = 0.0	$\Delta C_{4,3}$ = 0.0
	$S_{4,3}$ = N.A. (0.0)	$S_{4,3}$ = 0.0	$\Delta S_{4,3}$ = 0.0
	$C_{4,4}$ = 0.04034766412073938	$C_{4,4}$ = 0.04034766412073938	$\Delta C_{4,4}$ = 0.0
	$S_{4,4}$ = N.A. (0.0)	$S_{4,4}$ = 0.0	$\Delta S_{4,4}$ = 0.0
Europa	J_2 = 435.5	J_2 = 432.3	ΔJ_2 = -3.2
	$C_{2,1}$ = -1.4	$C_{2,1}$ = -1.4	$\Delta C_{2,1}$ = 0.0
	$S_{2,1}$ = 14.0	$S_{2,1}$ = -1.0	$\Delta S_{2,1}$ = -15.0
	$C_{2,2}$ = 131.5	$C_{2,2}$ = 129.0	$\Delta C_{2,2}$ = -2.5
	$S_{2,2}$ = 0.0	$S_{2,2}$ = 0.0	$\Delta S_{2,2}$ = 0.0
	J_3 = N.A. (0.0)	J_3 = 0.0	ΔJ_3 = 0.0
	$C_{3,1}$ = N.A. (0.0)	$C_{3,1}$ = 0.0	$\Delta C_{3,1}$ = 0.0
	$S_{3,1}$ = N.A. (0.0)	$S_{3,1}$ = 0.0	$\Delta S_{3,1}$ = 0.0
	$C_{3,2}$ = N.A. (0.0)	$C_{3,2}$ = -0.7	$\Delta C_{3,2}$ = -0.7
	$S_{3,2}$ = N.A. (0.0)	$S_{3,2}$ = 0.0	$\Delta S_{3,2}$ = 0.0
	$C_{3,3}$ = N.A. (0.0)	$C_{3,3}$ = 0.0	$\Delta C_{3,3}$ = 0.0
	$S_{3,3}$ = N.A. (0.0)	$S_{3,3}$ = -1.0	$\Delta S_{3,3}$ = -1.0
	J_4 = N.A. (0.0)	J_4 = 2.1	ΔJ_4 = 2.1

Ganymede	J_2 = 132.1749381068281	J_2 = 132.1749381068281	ΔJ_2 = 0.0
	$C_{2,1}$ = -0.01406383388388918	$C_{2,1}$ = -0.01406383388388918	$\Delta C_{2,1}$ = 0.0
	$S_{2,1}$ = -1.555435272149148	$S_{2,1}$ = -1.555435272149148	$\Delta S_{2,1}$ = 0.0
	$C_{2,2}$ = 39.7137621	$C_{2,2}$ = 39.7137621	$\Delta C_{2,2}$ = 0.0
	$S_{2,2}$ = -3.4924128	$S_{2,2}$ = -3.4924128	$\Delta S_{2,2}$ = 0.0
	J_3 = -1.037589660052676	J_3 = -1.037589660052676	ΔJ_3 = 0.0
	$C_{3,1}$ = -7.413877126265827	$C_{3,1}$ = -7.413877126265827	$\Delta C_{3,1}$ = 0.0
	$S_{3,1}$ = -6.450288178958351	$S_{3,1}$ = -6.450288178958351	$\Delta S_{3,1}$ = 0.0
	$C_{3,2}$ = -2.213830322146840	$C_{3,2}$ = -2.213830322146840	$\Delta C_{3,2}$ = 0.0
	$S_{3,2}$ = 3.482543908197695	$S_{3,2}$ = 3.482543908197695	$\Delta S_{3,2}$ = 0.0
	$C_{3,3}$ = -1.05629956762470	$C_{3,3}$ = -1.05629956762470	$\Delta C_{3,3}$ = 0.0
	$S_{3,3}$ = -0.1154464124145312	$S_{3,3}$ = -0.1154464124145312	$\Delta S_{3,3}$ = 0.0
	J_4 = 4.858141177350019	J_4 = 4.858141177350019	ΔJ_4 = 0.0
	$C_{4,1}$ = 3.811968749609735	$C_{4,1}$ = 3.811968749609735	$\Delta C_{4,1}$ = 0.0
	$S_{4,1}$ = 5.53109333310153	$S_{4,1}$ = 5.53109333310153	$\Delta S_{4,1}$ = 0.0
	$C_{4,2}$ = -0.2058302082476025	$C_{4,2}$ = -0.2058302082476025	$\Delta C_{4,2}$ = 0.0
	$S_{4,2}$ = -1.726226830065382	$S_{4,2}$ = -1.726226830065382	$\Delta S_{4,2}$ = 0.0
	$C_{4,3}$ = 0.1080367439331393	$C_{4,3}$ = 0.1080367439331393	$\Delta C_{4,3}$ = 0.0
	$S_{4,3}$ = 0.2320586551260027	$S_{4,3}$ = 0.2320586551260027	$\Delta S_{4,3}$ = 0.0
	$C_{4,4}$ = 0.006552813929525020	$C_{4,4}$ = 0.006552813929525020	$\Delta C_{4,4}$ = 0.0
	$S_{4,4}$ = 0.1195145846971386	$S_{4,4}$ = 0.1195145846971386	$\Delta S_{4,4}$ = 0.0
	J_5 = -2.317732751096073	J_5 = -2.317732751096073	ΔJ_5 = 0.0
	$C_{5,1}$ = N.A. (0.0)	$C_{5,1}$ = 0.0	$\Delta C_{5,1}$ = 0.0
	$S_{5,1}$ = N.A. (0.0)	$S_{5,1}$ = 0.0	$\Delta S_{5,1}$ = 0.0
	$C_{5,2}$ = N.A. (0.0)	$C_{5,2}$ = 0.0	$\Delta C_{5,2}$ = 0.0
	$S_{5,2}$ = N.A. (0.0)	$S_{5,2}$ = 0.0	$\Delta S_{5,2}$ = 0.0
	$C_{5,3}$ = N.A. (0.0)	$C_{5,3}$ = 0.0	$\Delta C_{5,3}$ = 0.0
	$S_{5,3}$ = N.A. (0.0)	$S_{5,3}$ = 0.0	$\Delta S_{5,3}$ = 0.0
	$C_{5,4}$ = N.A. (0.0)	$C_{5,4}$ = 0.0	$\Delta C_{5,4}$ = 0.0
	$S_{5,4}$ = N.A. (0.0)	$S_{5,4}$ = 0.0	$\Delta S_{5,4}$ = 0.0
	$C_{5,5}$ = N.A. (0.0)	$C_{5,5}$ = 0.0	$\Delta C_{5,5}$ = 0.0
	$S_{5,5}$ = N.A. (0.0)	$S_{5,5}$ = 0.0	$\Delta S_{5,5}$ = 0.0
	J_6 = -1.789263684630473	J_6 = -1.789263684630473	ΔJ_6 = 0.0
	J_7 = -0.8344089674985037	J_7 = -0.8344089674985037	ΔJ_7 = 0.0
	J_8 = -0.8882961790496313	J_8 = -0.8882961790496313	ΔJ_8 = 0.0
	J_9 = N.A. (0.000)	J_9 = 0.014	ΔJ_9 = 0.014
Callisto	J_2 = 32.7 $C_{2,1}$ = 0.0 $S_{2,1}$ = 0.0 $C_{2,2}$ = 10.2 $S_{2,2}$ = -1.1	J_2 = 33.3 $C_{2,1}$ = 1.0 $S_{2,1}$ = 1.6 $C_{2,2}$ = 9.9 $S_{2,2}$ = -0.8	ΔJ_2 = 0.6 $\Delta C_{2,1}$ = 1.0 $\Delta S_{2,1}$ = 1.6 $\Delta C_{2,2}$ = -0.3 $\Delta S_{2,2}$ = 0.3
	J_3 = N.A. (0.0)	J_3 = 0.0	ΔJ_3 = 0.0
	$C_{3,1}$ = N.A. (0.0)	$C_{3,1}$ = 0.0	$\Delta C_{3,1}$ = 0.0
	$S_{3,1}$ = N.A. (0.0)	$S_{3,1}$ = 0.0	$\Delta S_{3,1}$ = 0.0
	$C_{3,2}$ = N.A. (0.0) $S_{3,2}$ = N.A. (0.0)	$C_{3,2}$ = -0.1 $S_{3,2}$ = -0.2	$\Delta C_{3,2}$ = -0.1 $\Delta S_{3,2}$ = -0.2
	$C_{3,3}$ = N.A. (0.0)	$C_{3,3}$ = 0.0	$\Delta C_{3,3}$ = 0.0
	$S_{3,3}$ = N.A. (0.0)	$S_{3,3}$ = 0.0	$\Delta S_{3,3}$ = 0.0

G

RMSE IN LO COMPONENTS

This Appendix presents the RMSE (on both position and velocity) decomposed along the three LO axes, for every flyby investigated in this paper.

This is shown through the Figures G.1 to G.32:

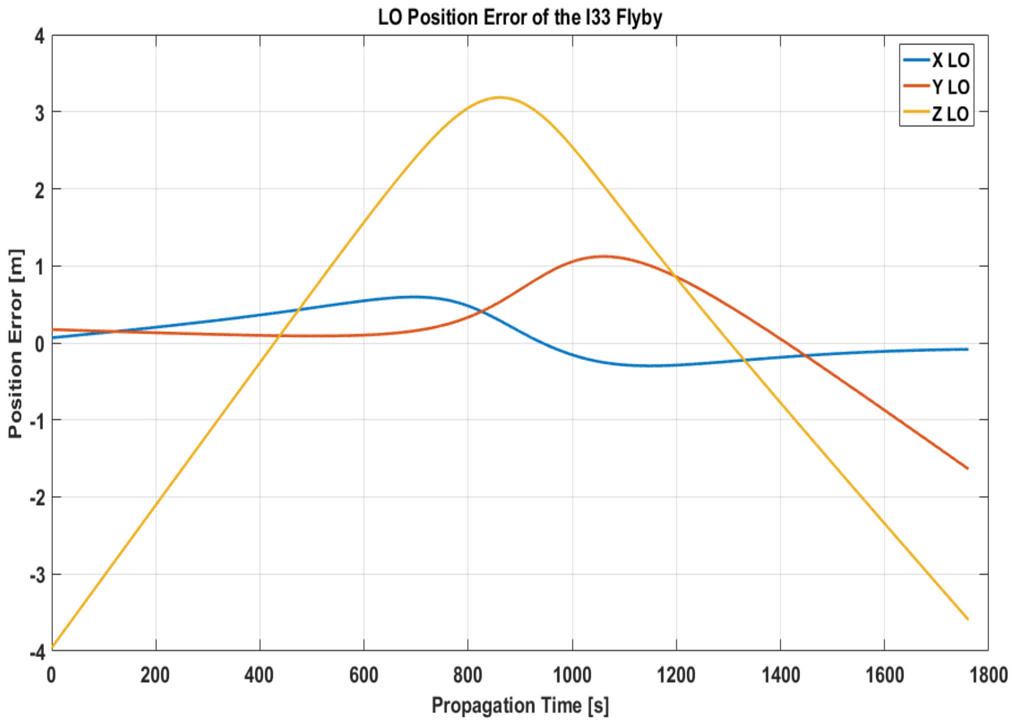

Figure G.1: Graphical representation of the RMSE on position of the I33 flyby as a function of the propagation time.

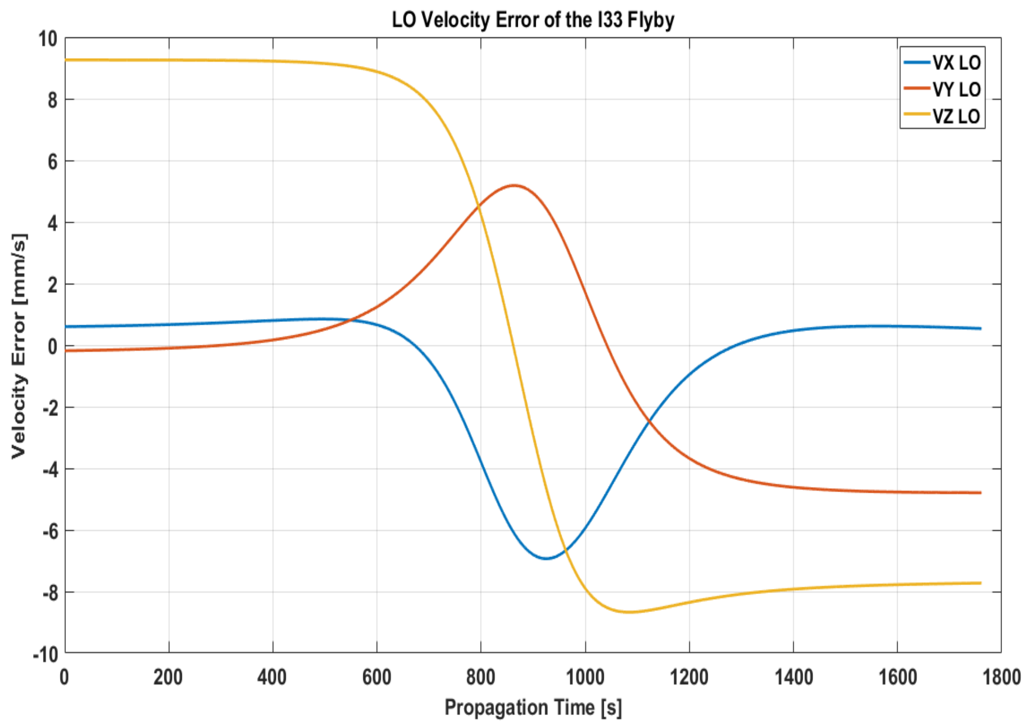

Figure G.2: Graphical representation of the RMSE on velocity of the I33 flyby as a function of the propagation time.

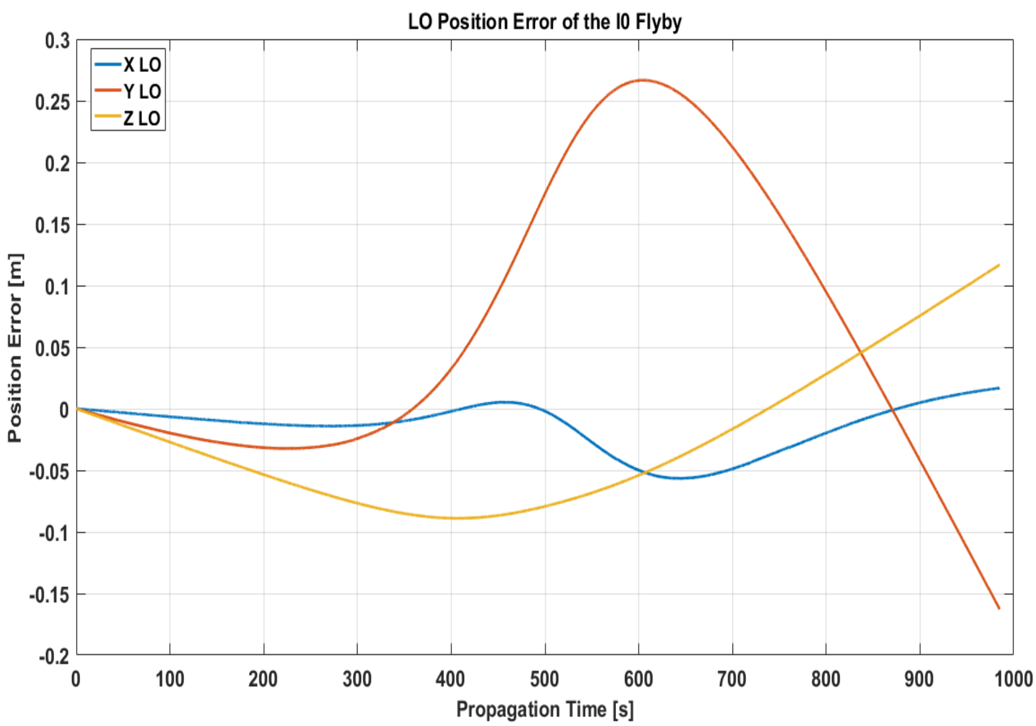

Figure G.3: Graphical representation of the RMSE on position of the I0 flyby as a function of the propagation time.

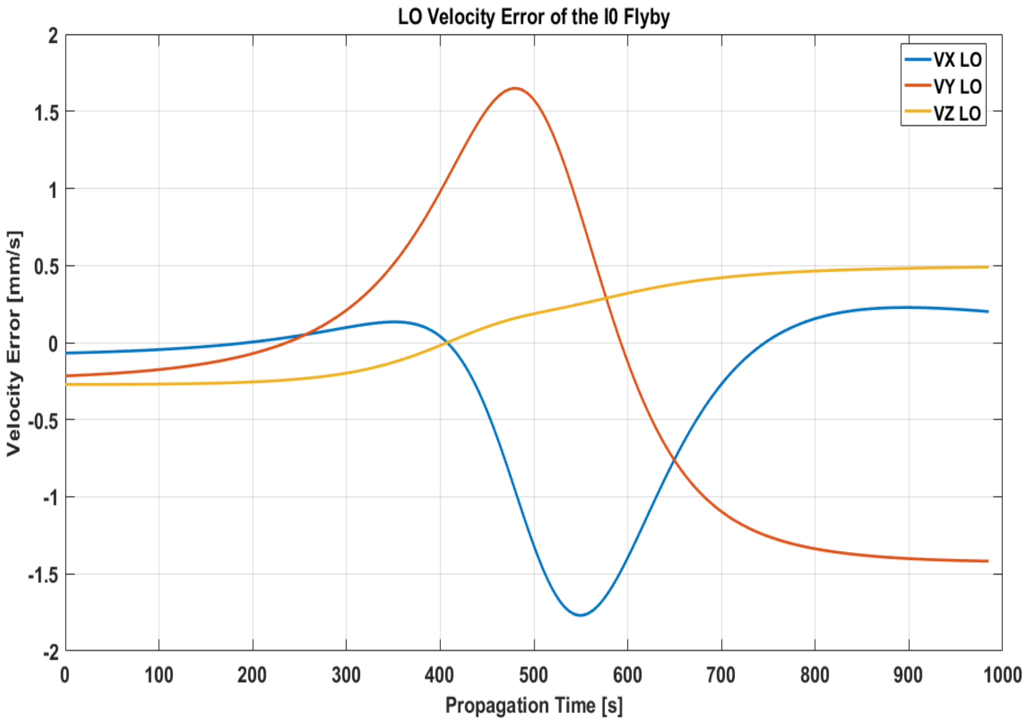

Figure G.4: Graphical representation of the RMSE on velocity of the I0 flyby as a function of the propagation time.

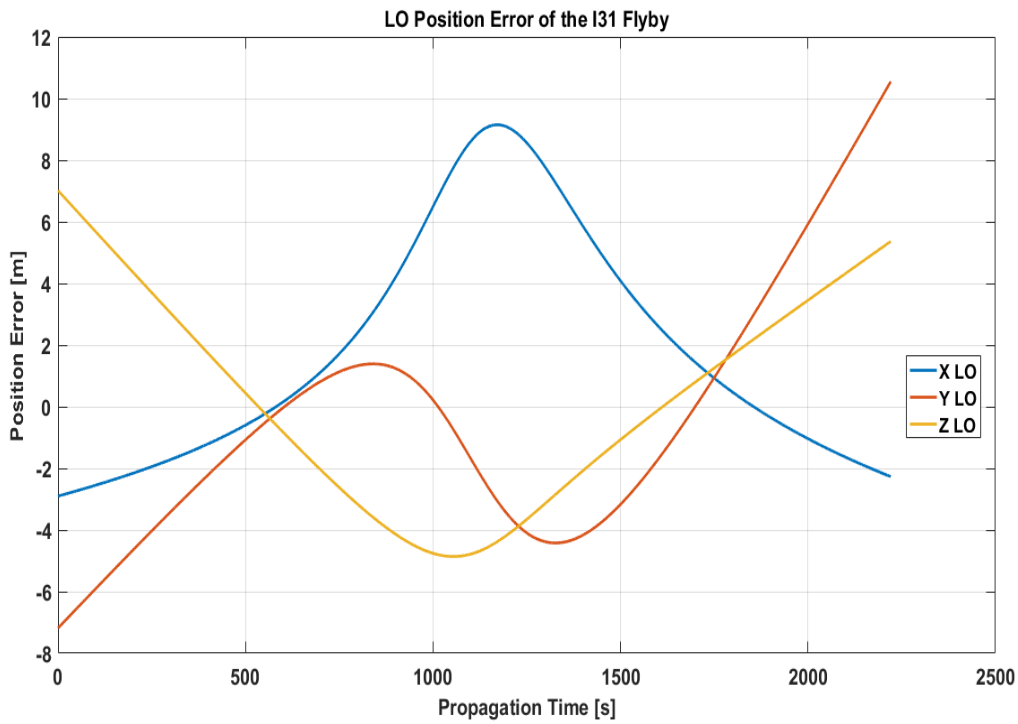

Figure G.5: Graphical representation of the RMSE on position of the I31 flyby as a function of the propagation time.

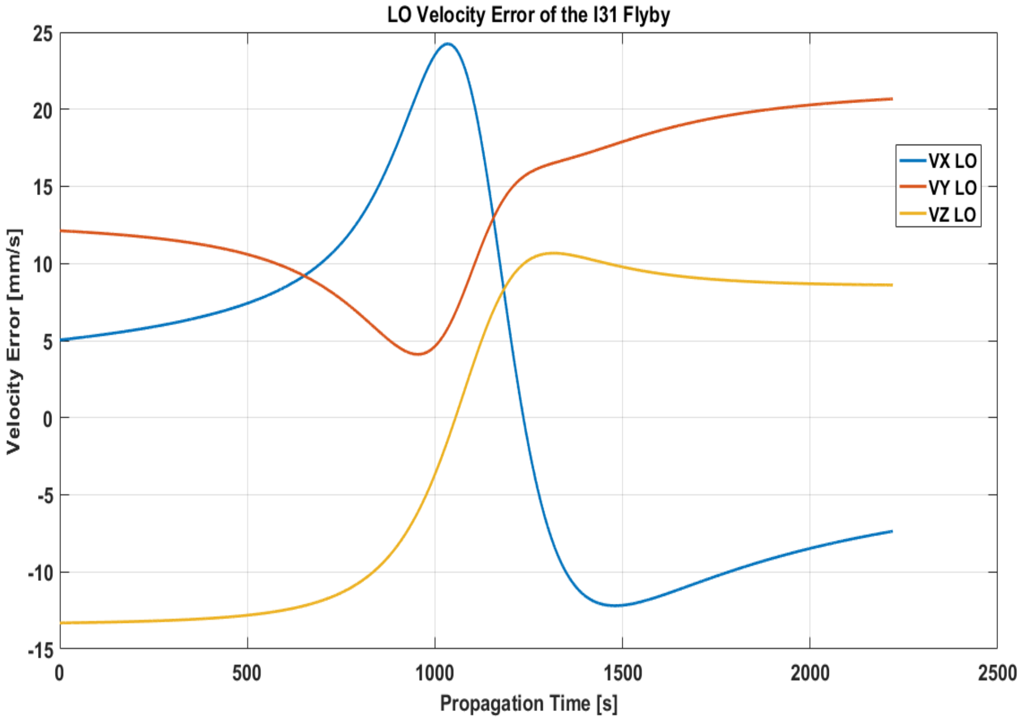

Figure G.6: Graphical representation of the RMSE on velocity of the I31 flyby as a function of the propagation time.

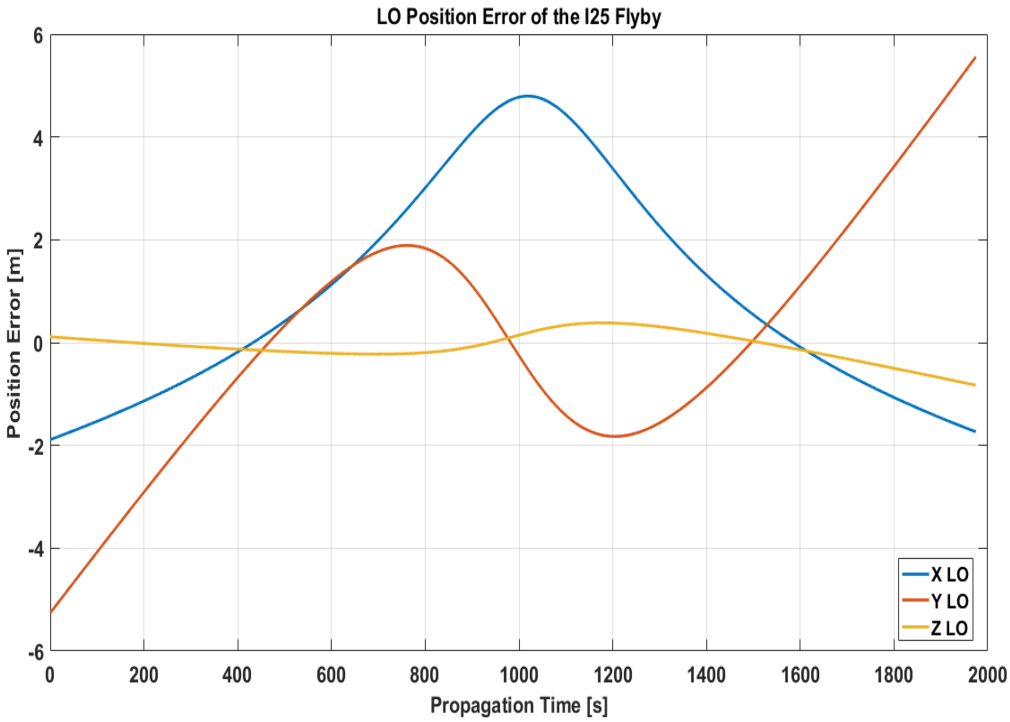

Figure G.7: Graphical representation of the RMSE on position of the I25 flyby as a function of the propagation time.

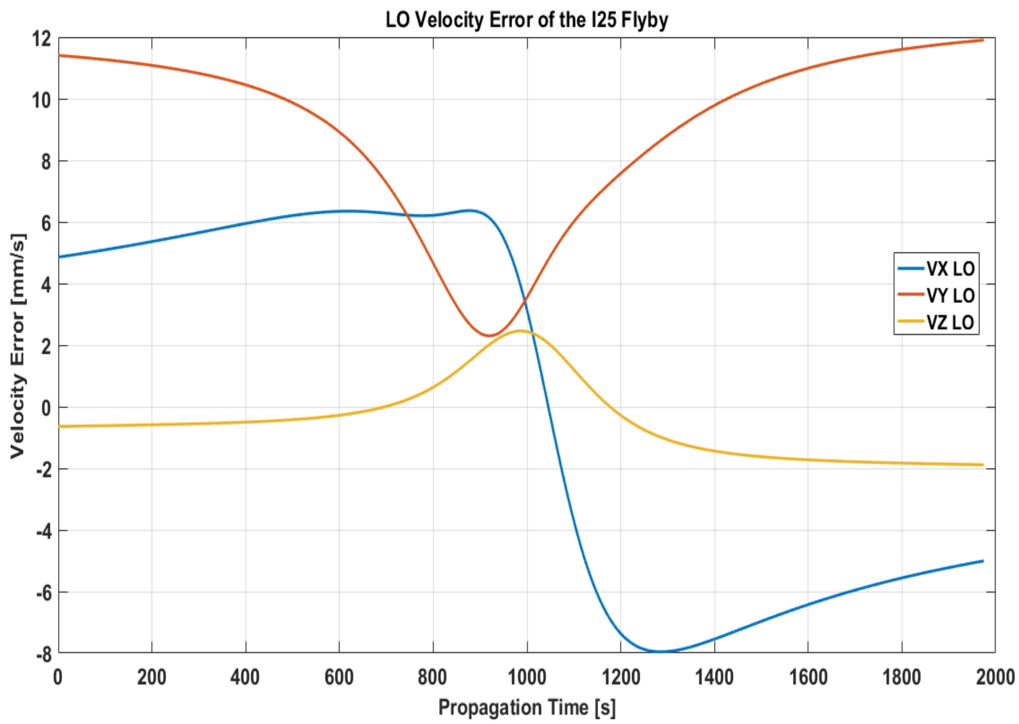

Figure G.8: Graphical representation of the RMSE on velocity of the I25 flyby as a function of the propagation time.

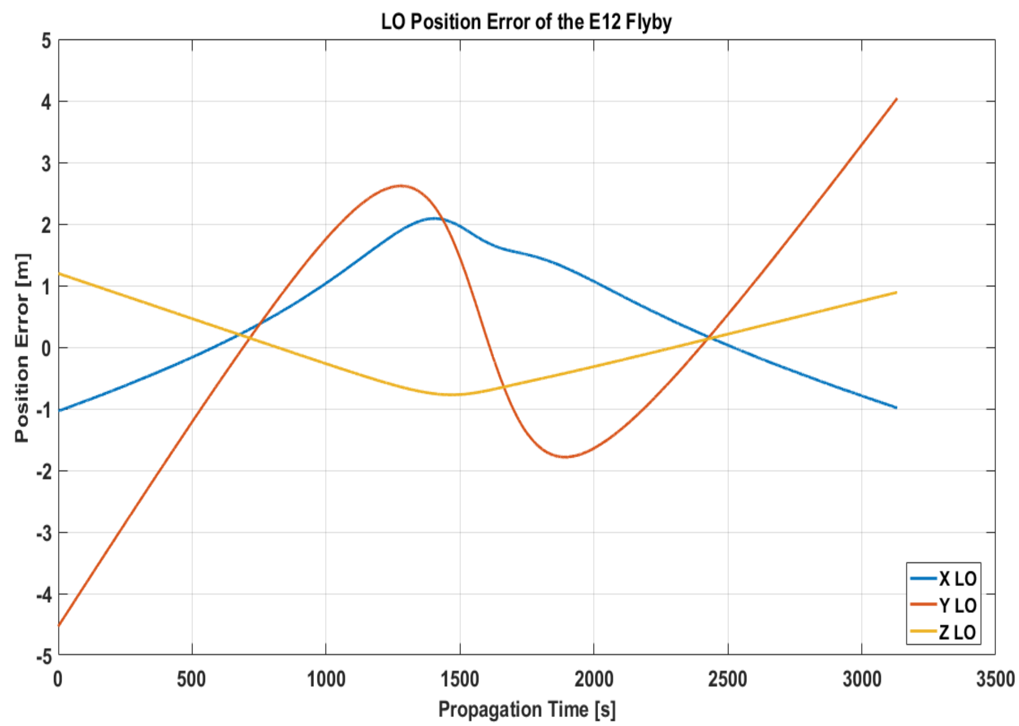

Figure G.9: Graphical representation of the RMSE on position of the E12 flyby as a function of the propagation time.

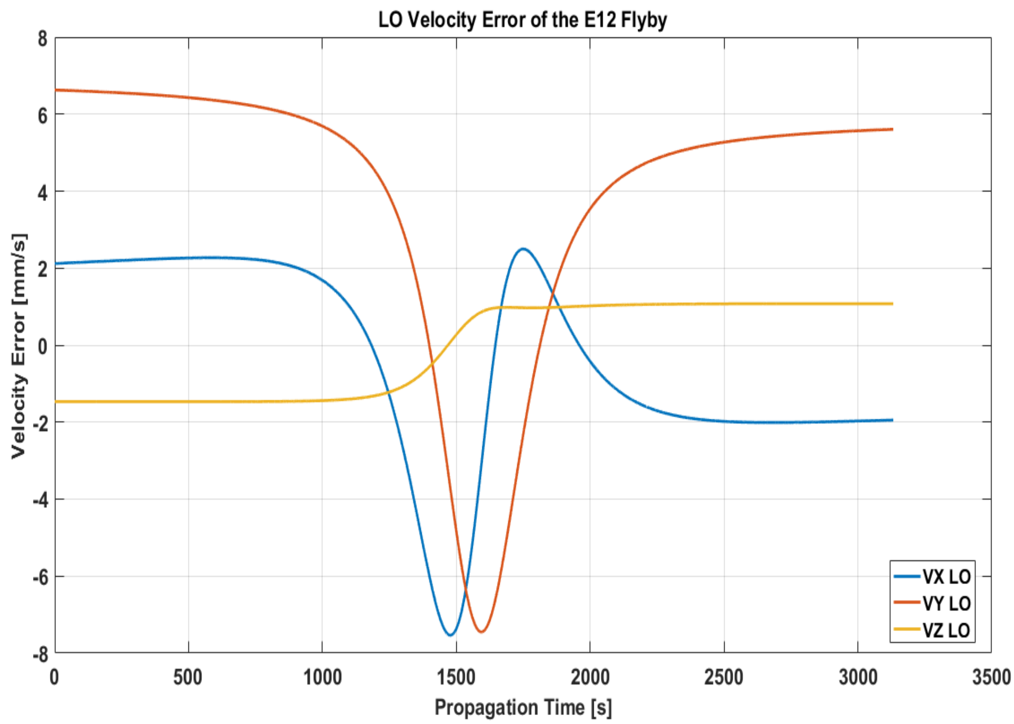

Figure G.10: Graphical representation of the RMSE on velocity of the E12 flyby as a function of the propagation time.

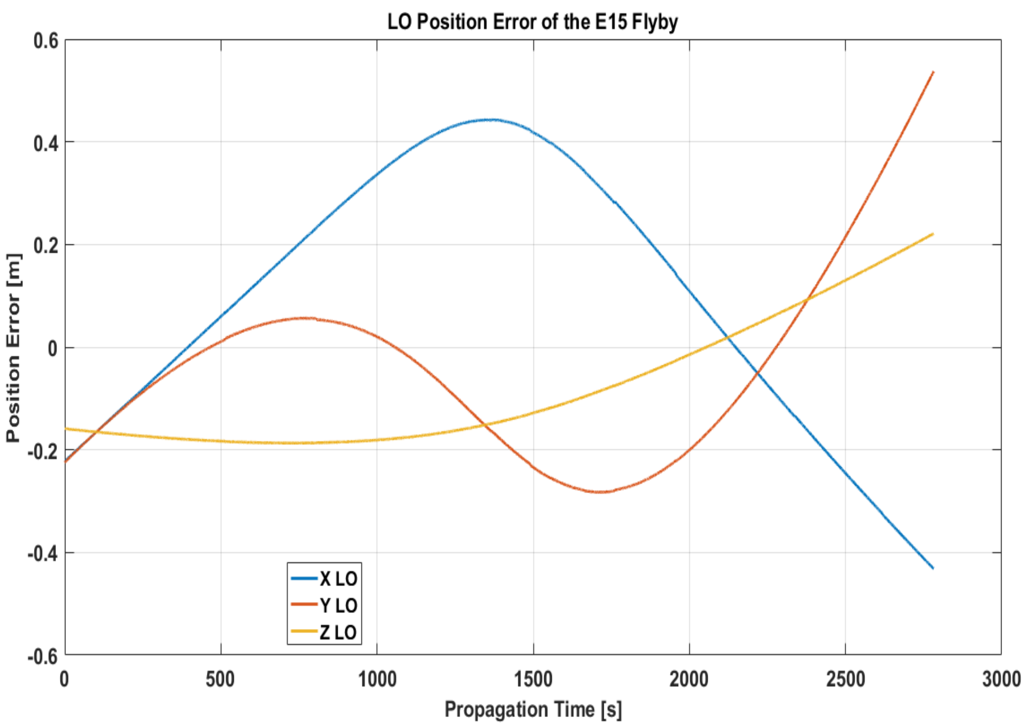

Figure G.11: Graphical representation of the RMSE on position of the E15 flyby as a function of the propagation time.

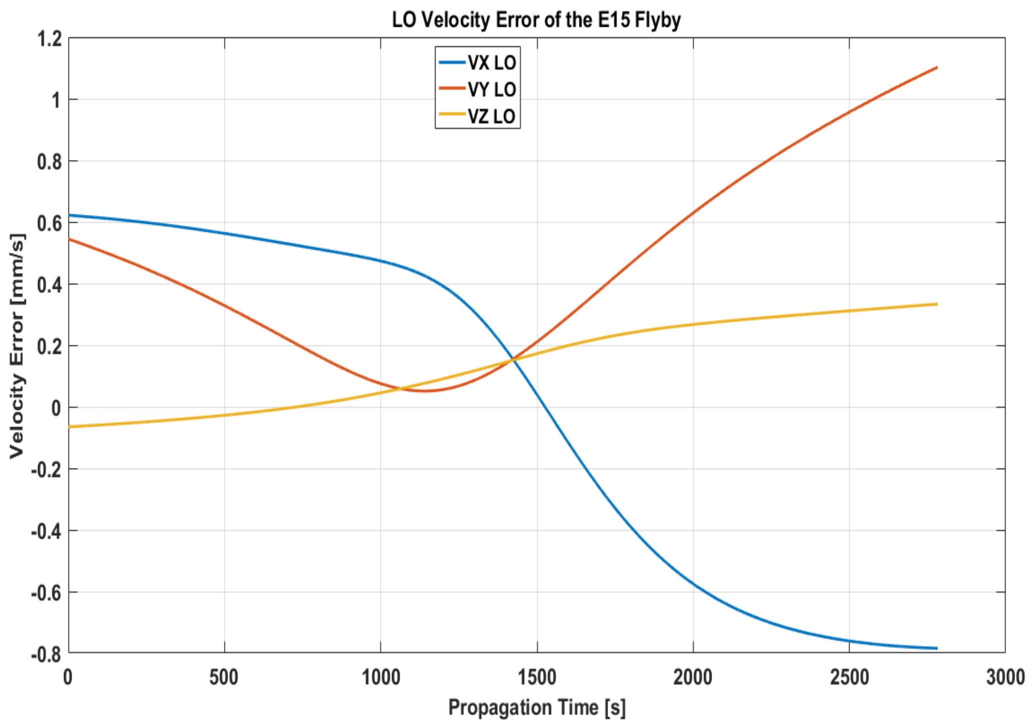

Figure G.12: Graphical representation of the RMSE on velocity of the E15 flyby as a function of the propagation time.

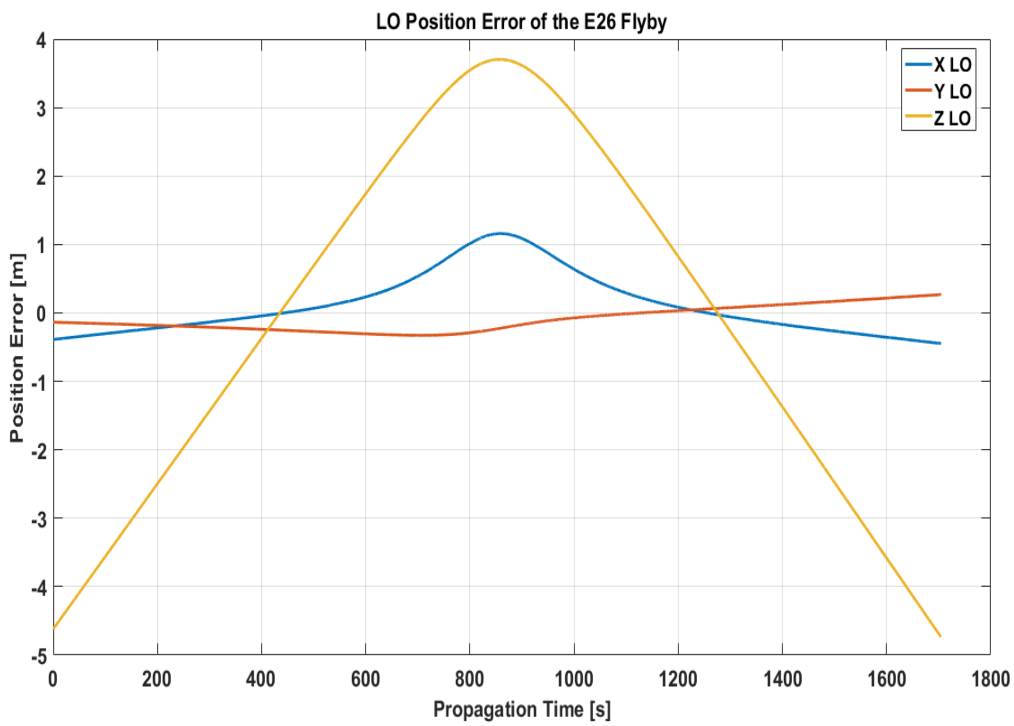

Figure G.13: Graphical representation of the RMSE on position of the E26 flyby as a function of the propagation time.

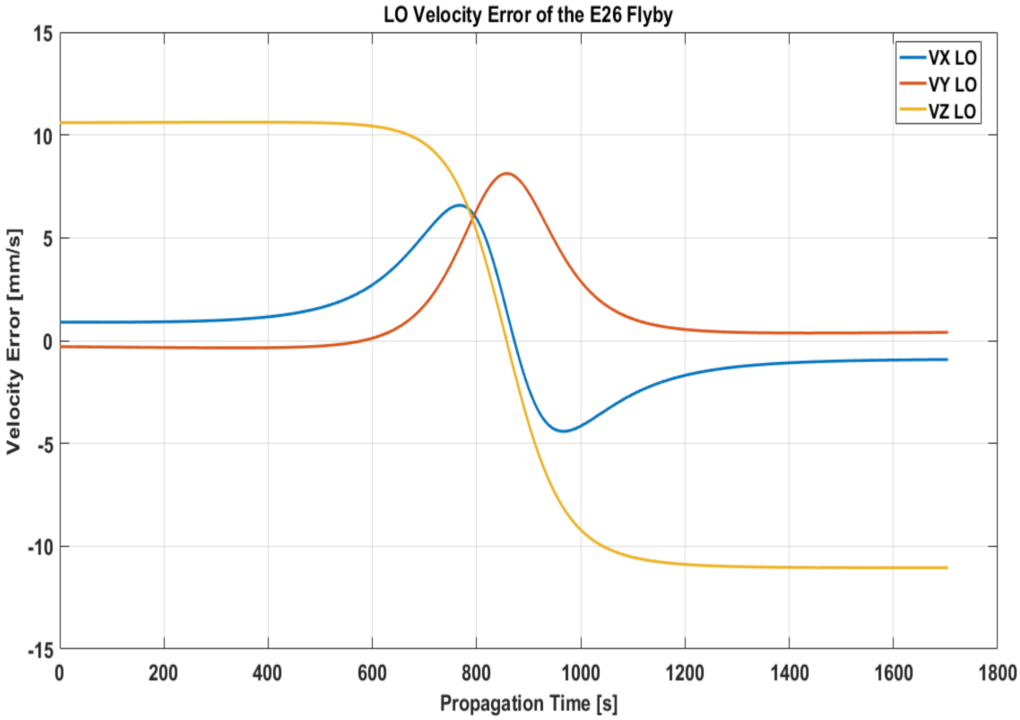

Figure G.14: Graphical representation of the RMSE on velocity of the E26 flyby as a function of the propagation time.

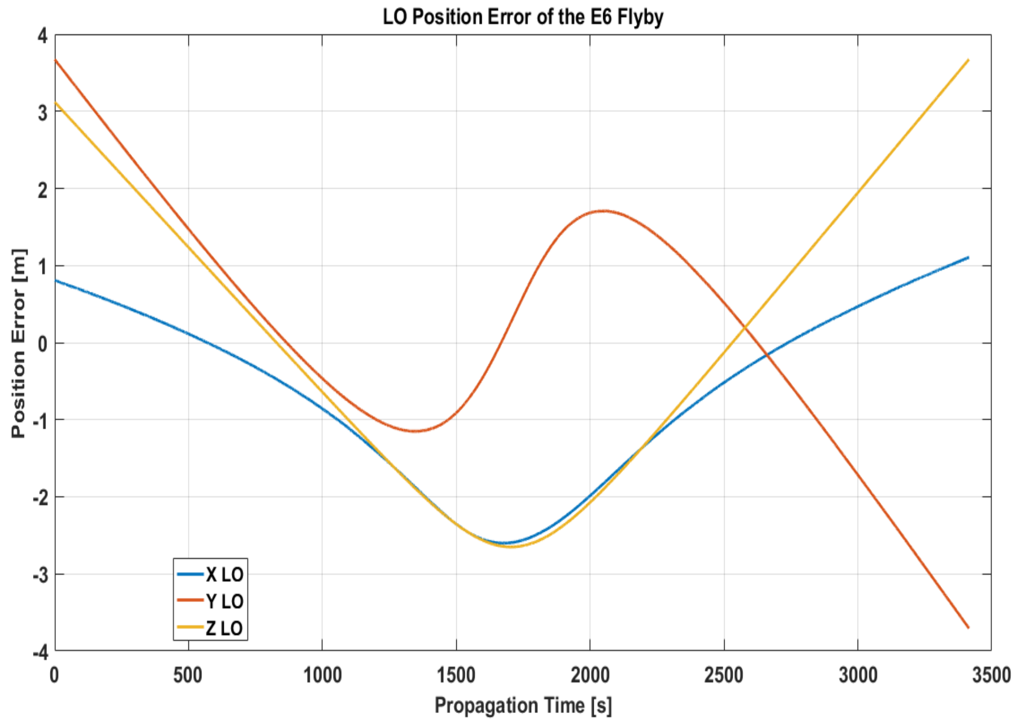

Figure G.15: Graphical representation of the RMSE on position of the E6 flyby as a function of the propagation time.

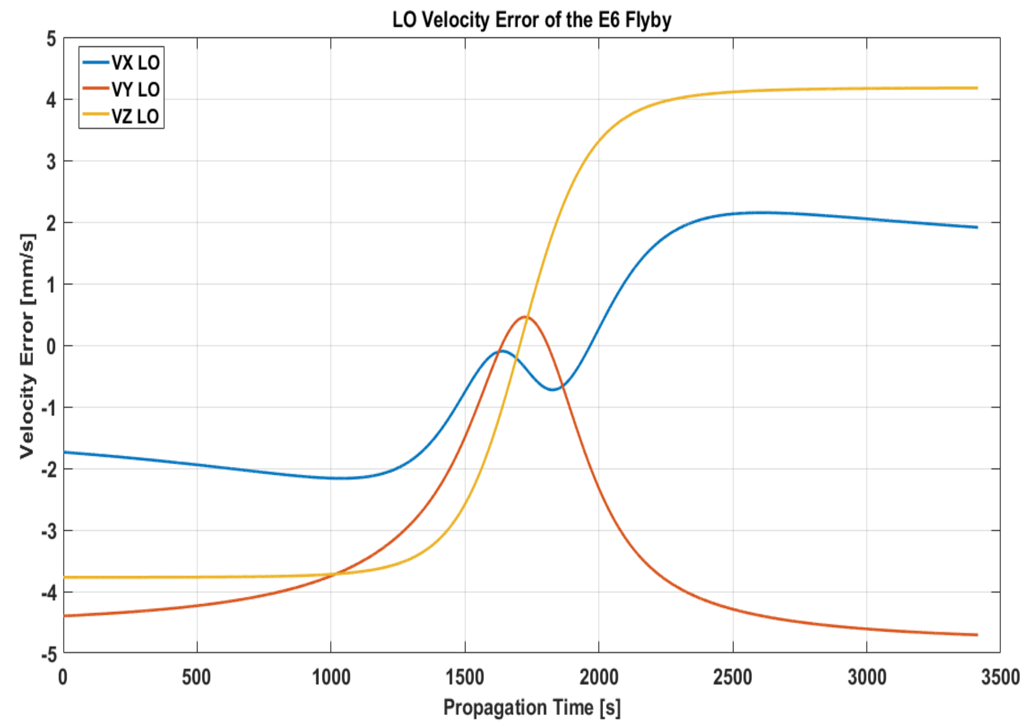

Figure G.16: Graphical representation of the RMSE on velocity of the E6 flyby as a function of the propagation time.

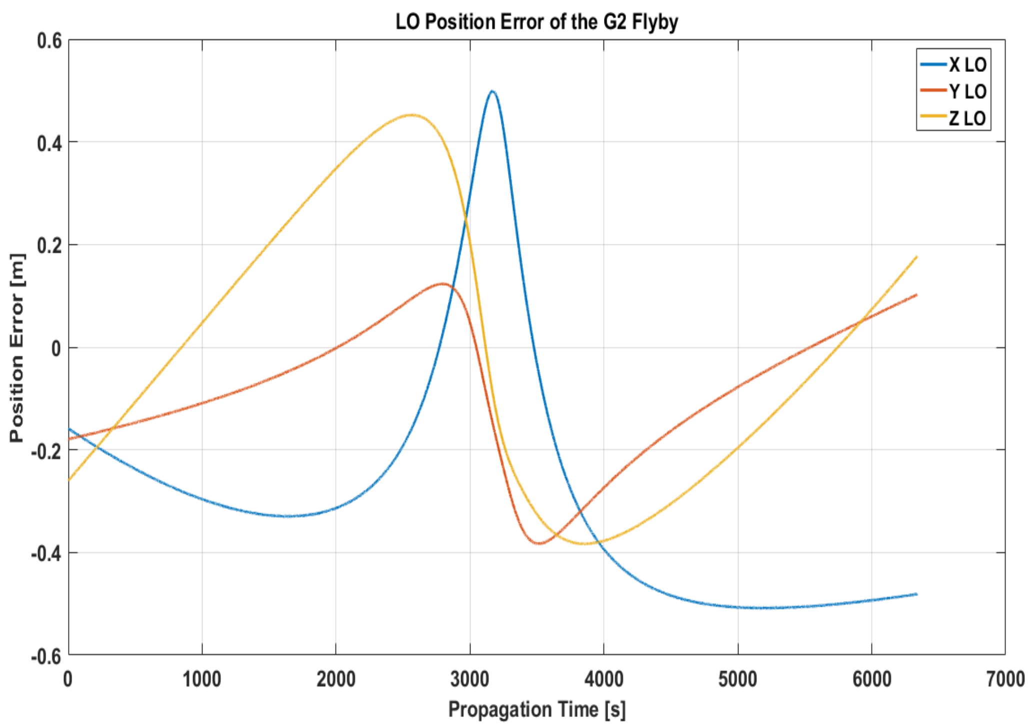

Figure G.17: Graphical representation of the RMSE on position of the G2 flyby as a function of the propagation time.

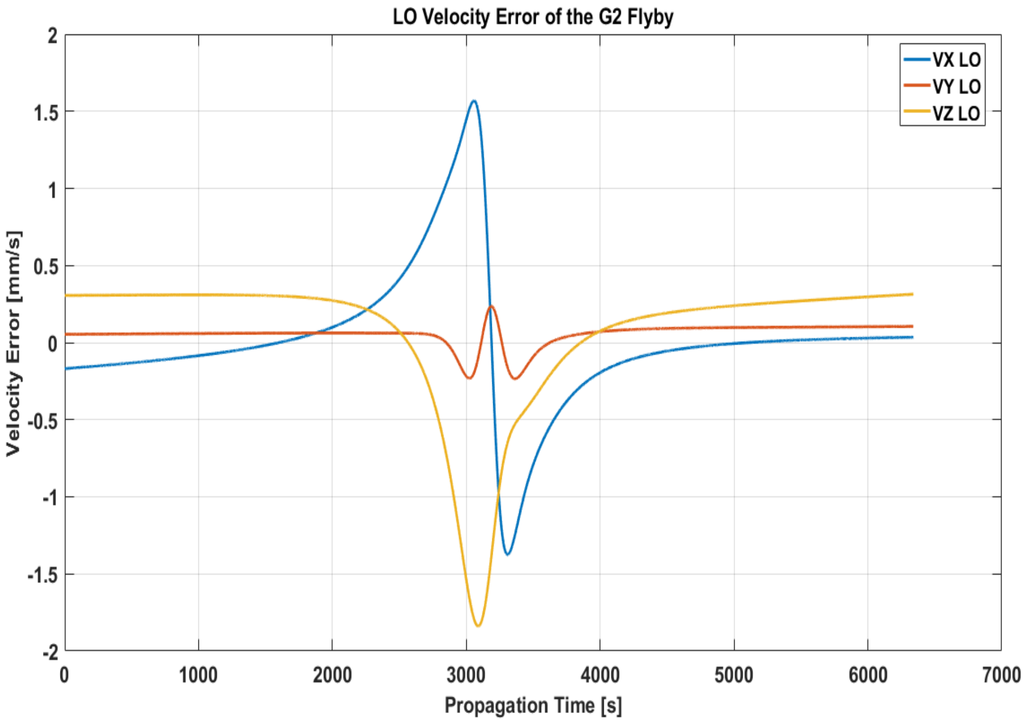

Figure G.18: Graphical representation of the RMSE on velocity of the G2 flyby as a function of the propagation time.

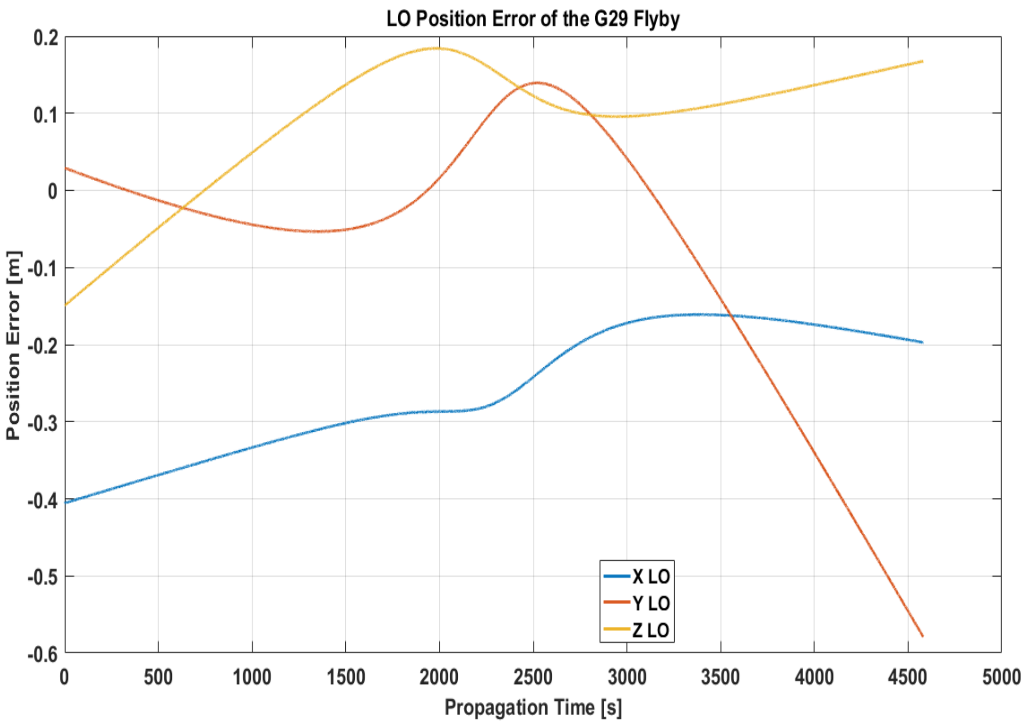

Figure G.19: Graphical representation of the RMSE on position of the G29 flyby as a function of the propagation time.

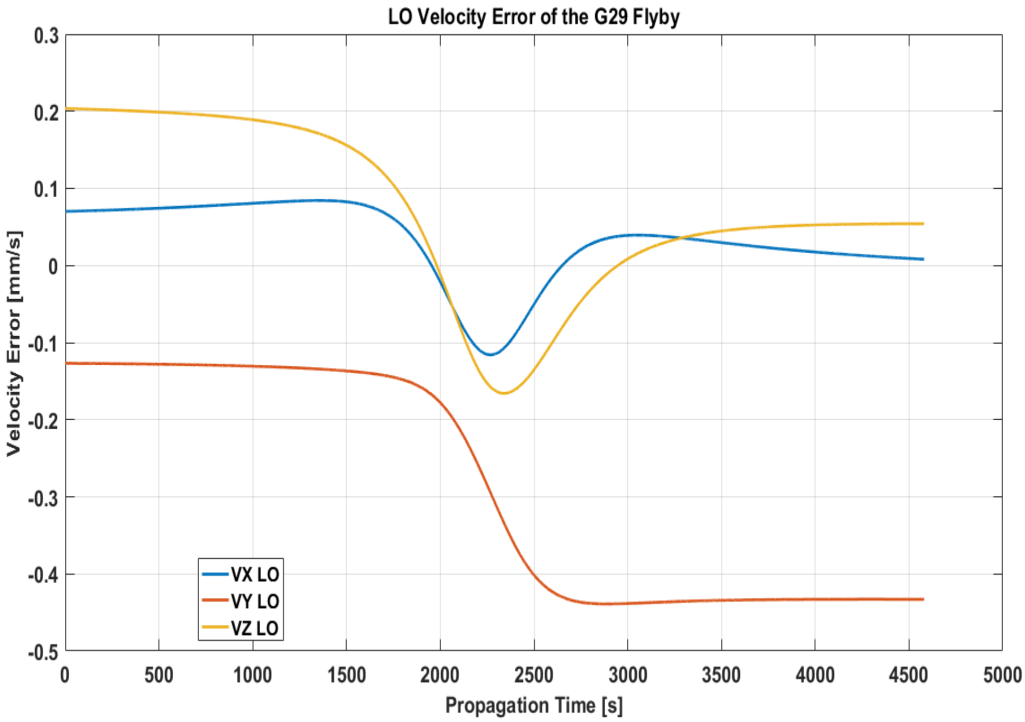

Figure G.20: Graphical representation of the RMSE on velocity of the G29 flyby as a function of the propagation time.

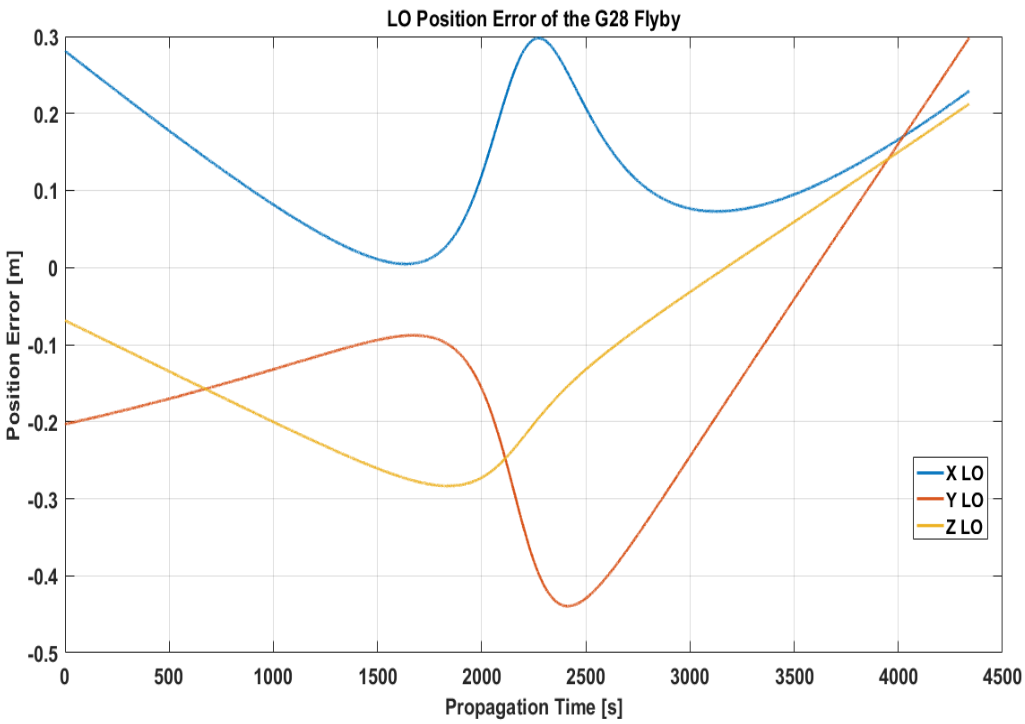

Figure G.21: Graphical representation of the RMSE on position of the G28 flyby as a function of the propagation time.

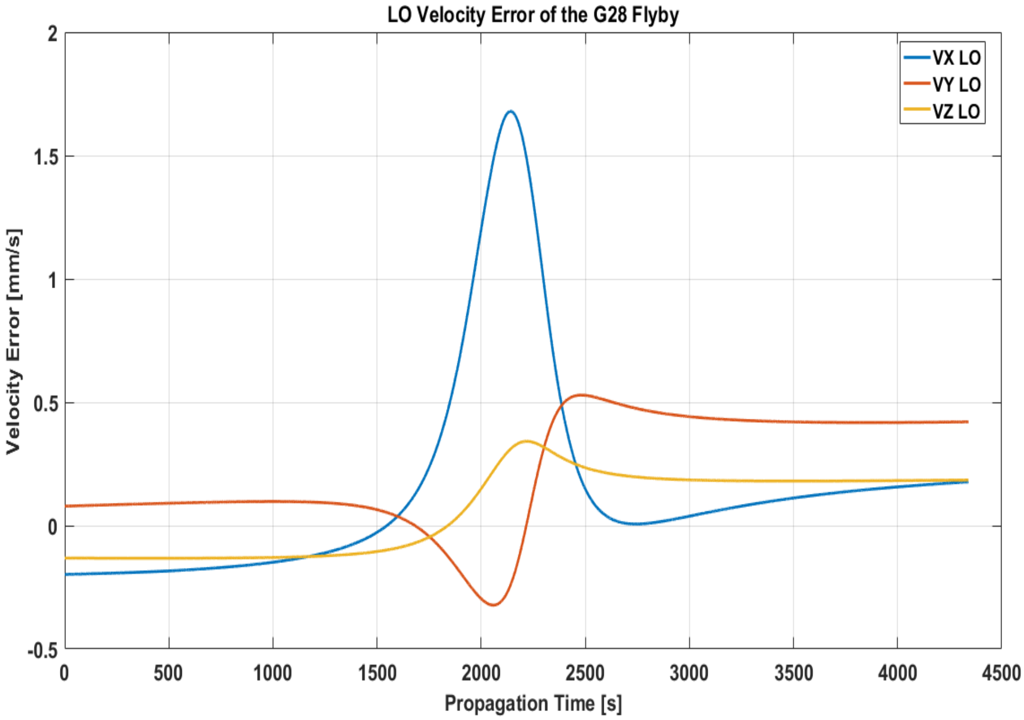

Figure G.22: Graphical representation of the RMSE on velocity of the G28 flyby as a function of the propagation time.

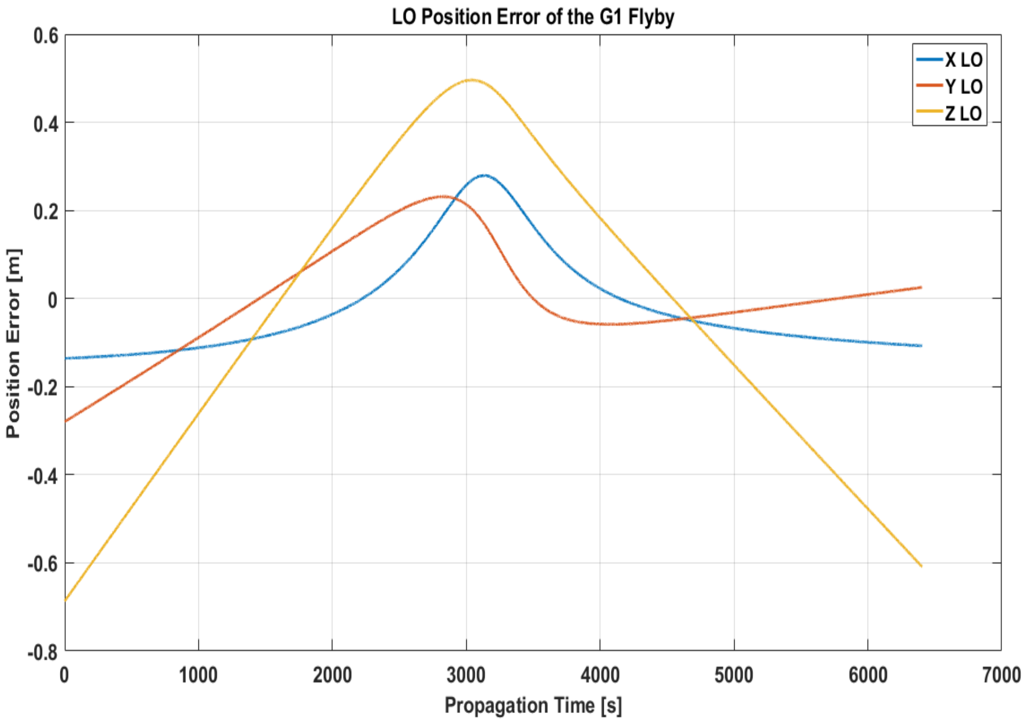

Figure G.23: Graphical representation of the RMSE on position of the G1 flyby as a function of the propagation time.

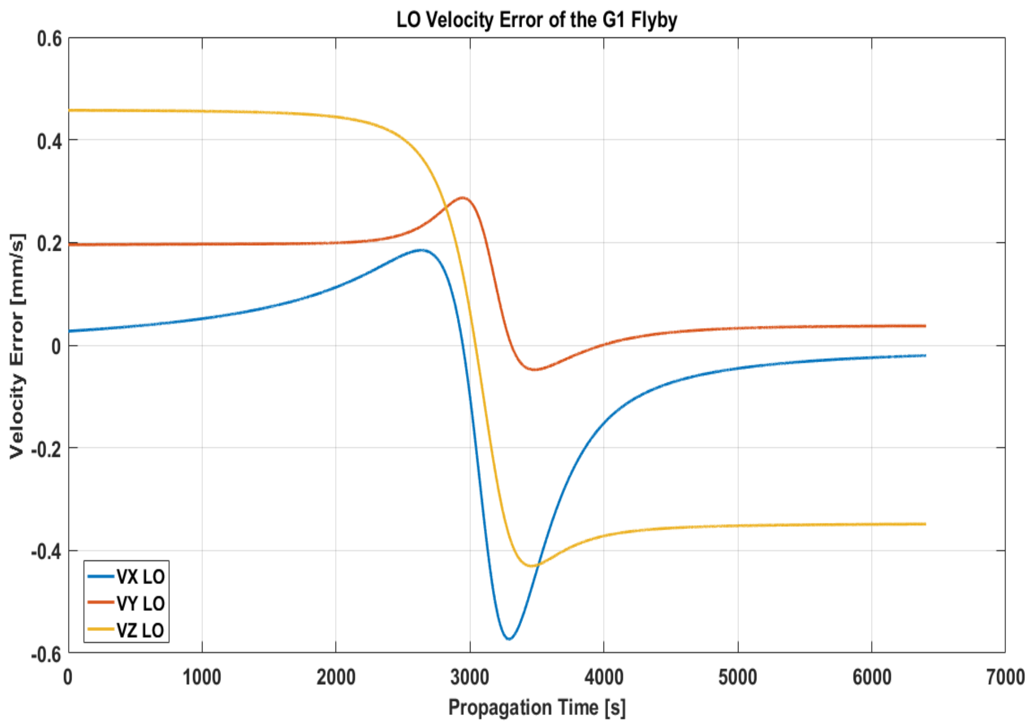

Figure G.24: Graphical representation of the RMSE on velocity of the G1 flyby as a function of the propagation time.

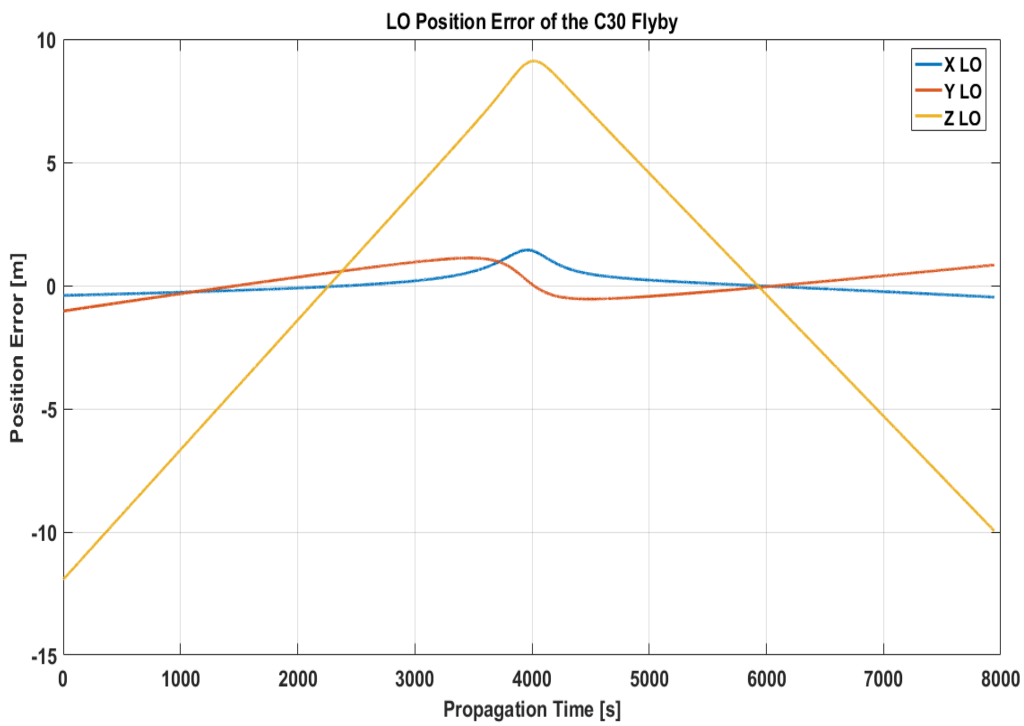

Figure G.25: Graphical representation of the RMSE on position of the C30 flyby as a function of the propagation time.

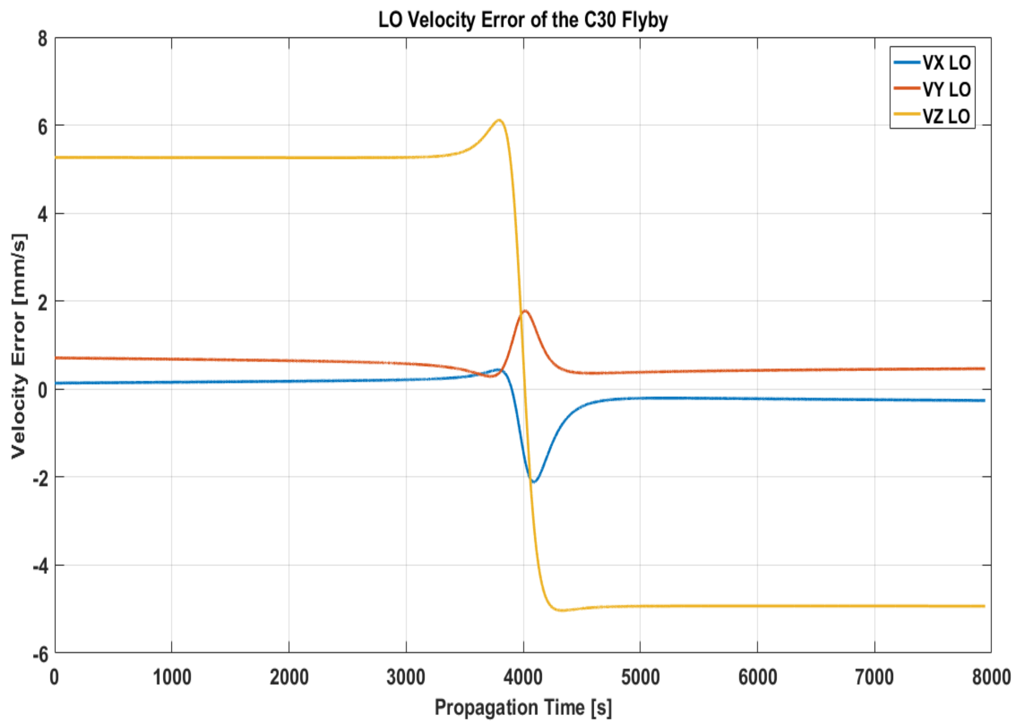

Figure G.26: Graphical representation of the RMSE on velocity of the C30 flyby as a function of the propagation time.

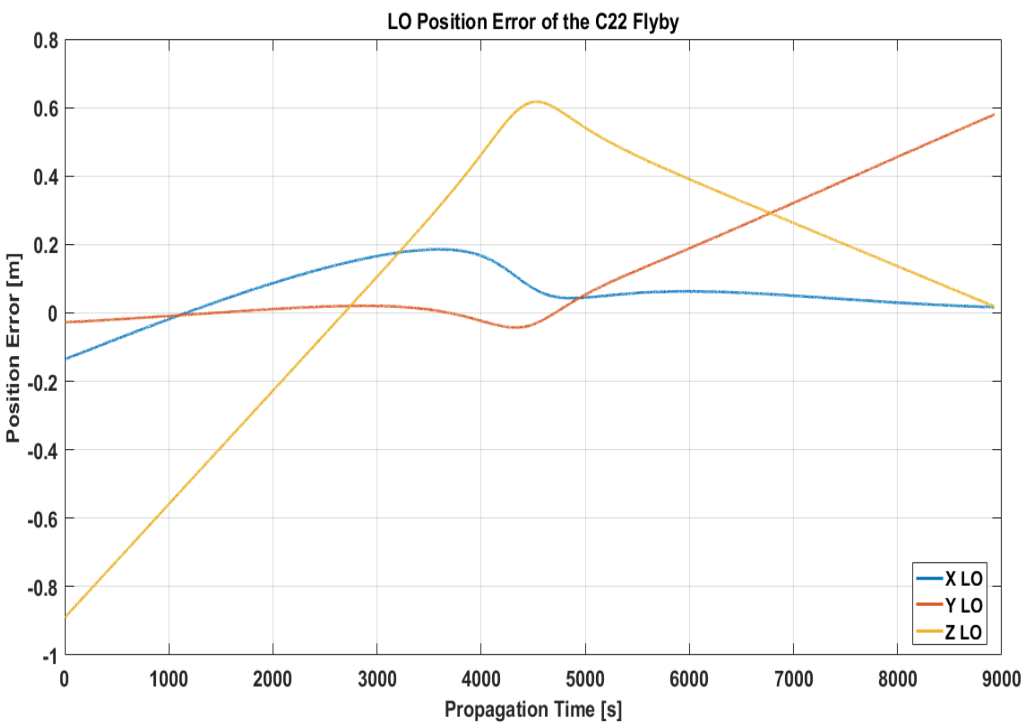

Figure G.27: Graphical representation of the RMSE on position of the C22 flyby as a function of the propagation time.

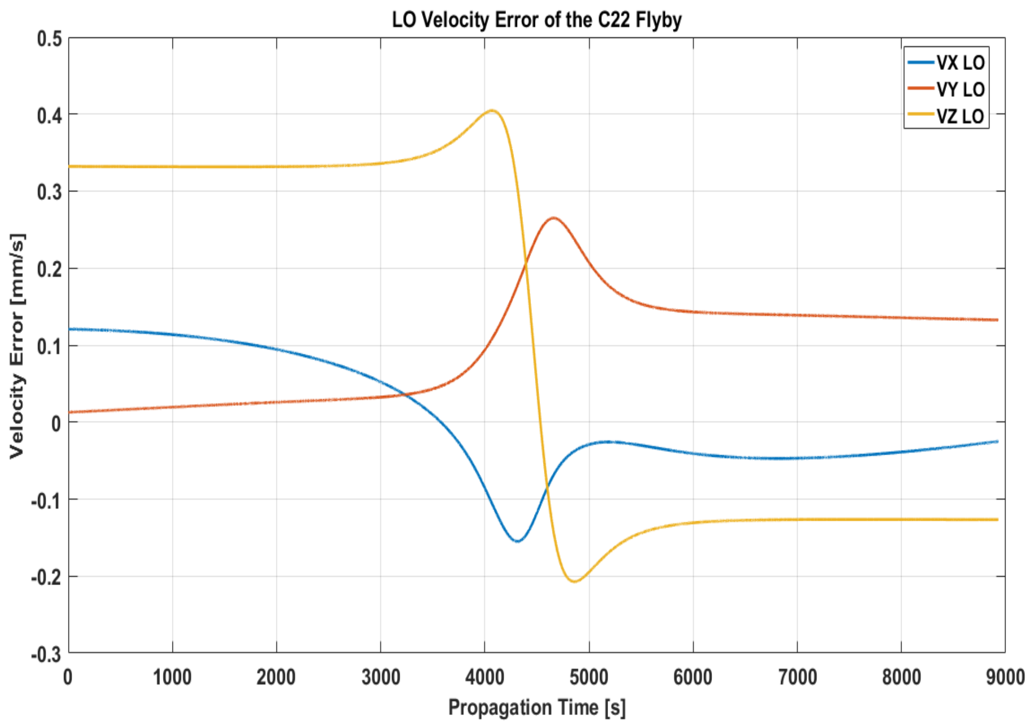

Figure G.28: Graphical representation of the RMSE on velocity of the C22 flyby as a function of the propagation time.

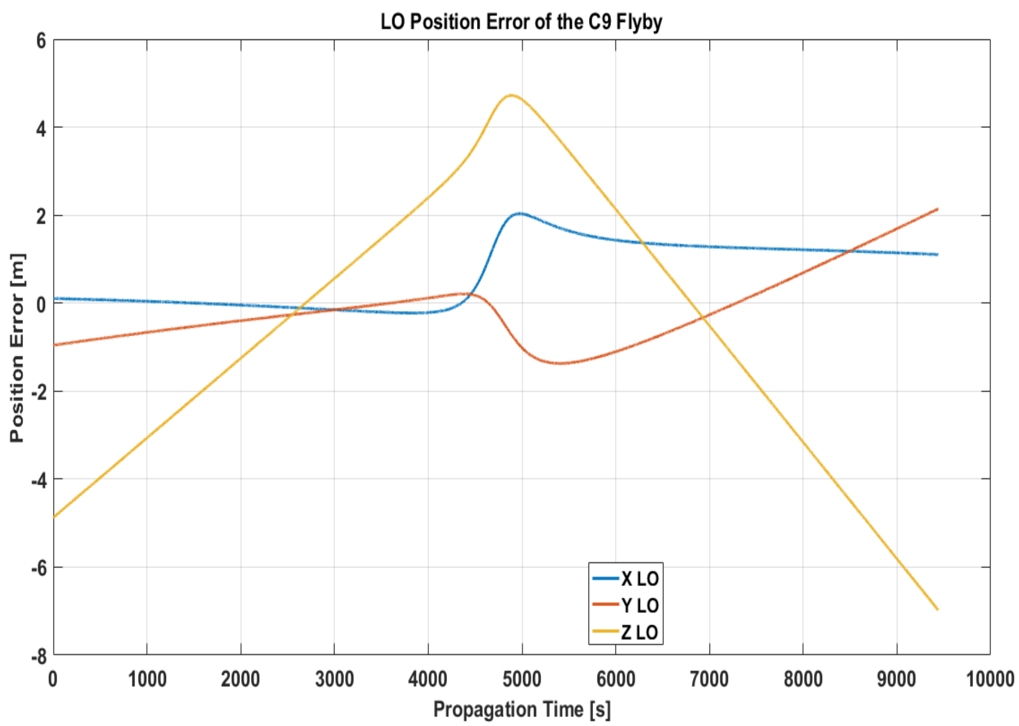

Figure G.29: Graphical representation of the RMSE on position of the C9 flyby as a function of the propagation time.

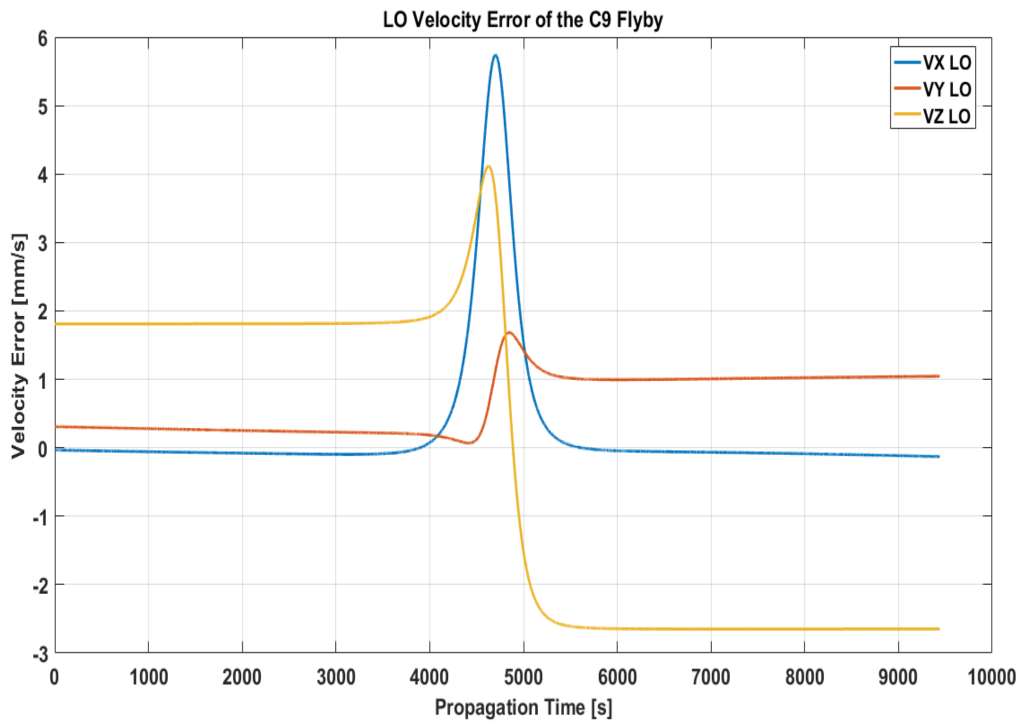

Figure G.30: Graphical representation of the RMSE on velocity of the C9 flyby as a function of the propagation time.

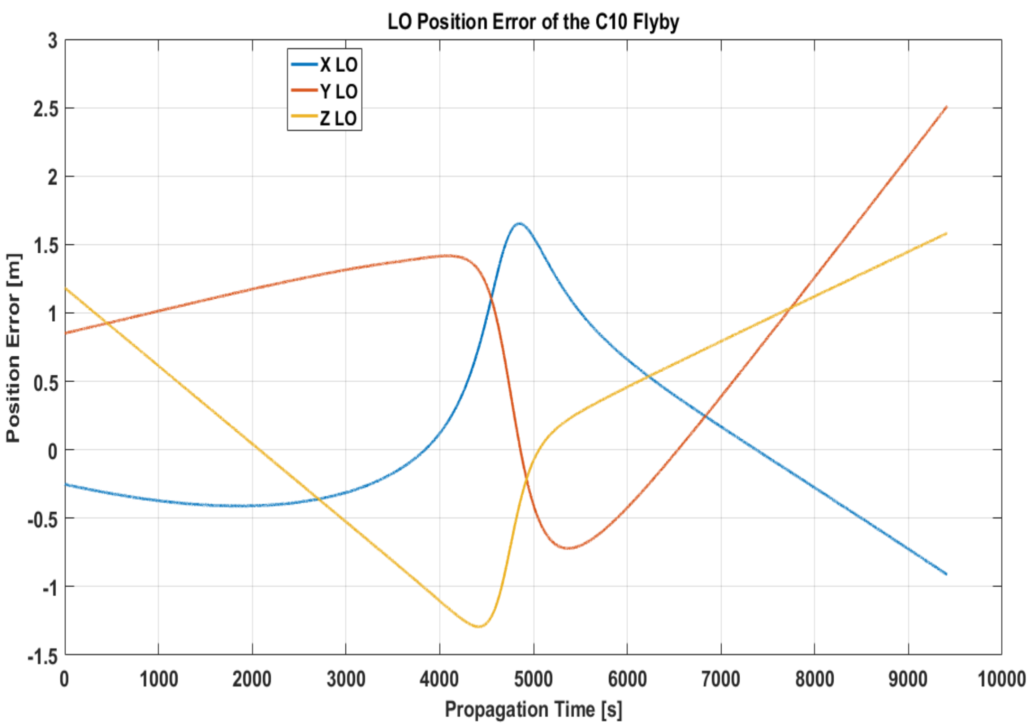

Figure G.31: Graphical representation of the RMSE on position of the C10 flyby as a function of the propagation time.

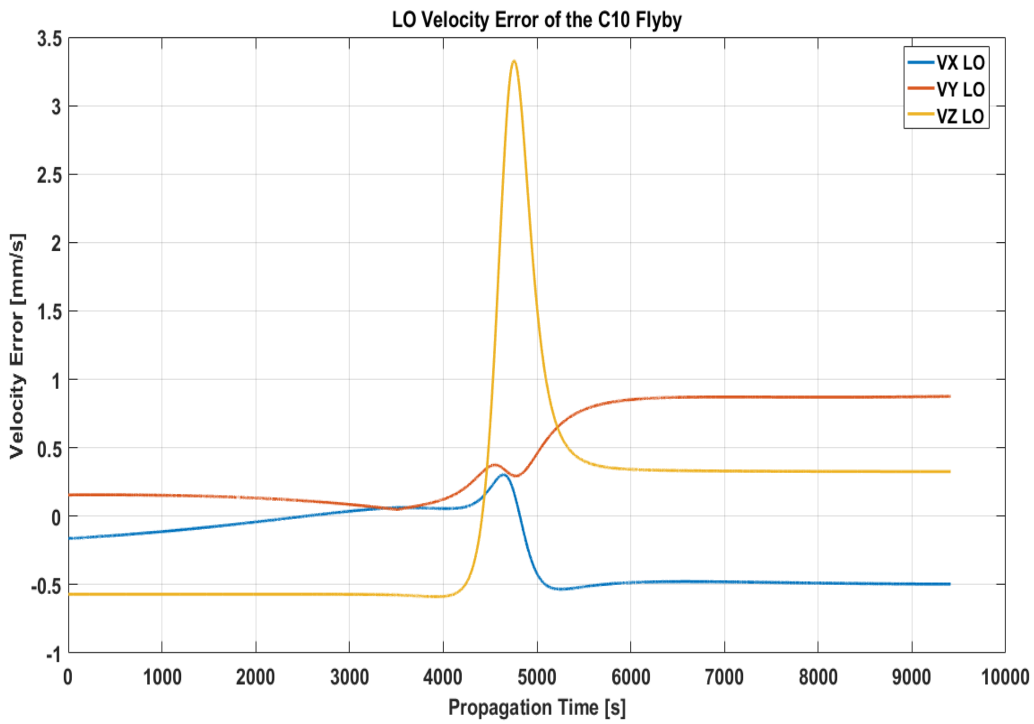

Figure G.32: Graphical representation of the RMSE on velocity of the C10 flyby as a function of the propagation time.

BIBLIOGRAPHY

Anderson, J. D., Schubert, G., Jacobson, R. A., Lau, E. L., Moore, W. B., and Sjogren, W. L, *Europa's Differentiated Internal Structure: Inferences From Four Galileo Encounters.* Science 281(5385), 1998. PMID: 9748159.

Anderson, J. D., Jacobson, R. A., McElrath, T. P., Moore, W. B., Schubert, G., and Thomas, P. C, *Shape, mean radius, gravity field, and interior structure of Callisto.* Icarus 153, 2001. ISSN: 00191035.

Ashino, R., Nagase, M., and Vaillancourt, R., *Behind and Beyond the MATLAB ODE Suite.* Computers & Mathematics with Applications, 40(4), pp. 498-499, 2000.

Bagenal, F., Dowling, T. E., and McKinnon, W. B. , *Jupiter: the planet, satellites and magnetosphere (Vol. 1).* Cambridge University Press, 2006. ISBN: 978-0521035453.

Bao, J. and Tsui, Y. , *Fundamentals of Global Positioning System receivers: a software approach.* J. Wiley & Sons Inc., 2000. ISBN: 0-471-20054-9.

Born, G. H. , *ASEN3200 Orbital Mechanics/Attitude Dynamics and Control, Lecture Notes.* University of Colorado Boulder, 2002.

Campbell, J. K. and Synnott, S. P, *Gravity field of the Jovian system from Pioneer and Voyager tracking data.* Astronomical Journal, Vol. 90, 1985. ISSN: 0004-6256.

Dallas, S. S., *Equations of motion for rotating finite bodies in the extended PPN formalism.* Celestial Mechanics and Dynamical Astronomy, 15(1), 1977.

Demanet, L., *Introduction to Numerical Analysis, Lecture Notes.* Massachusetts Institute of Technology, 2014. `http://math.mit.edu/icg/resources/notes330.pdf`. Date of access: 01/02/2017.

ESA, *JUICE definition study report*, 2014. `http://sci.esa.int/juice/54994-juice-definition-study-report/`. Date of access: 31/07/2016.

Galilei, G., *Sidereus Nuncius.* Baglioni, Venezia, 1st edition, 1610. ISBN: 9788887328530.

Gao, P. and Stevenson, D. J. , *Nonhydrostatic effects and the determination of icy satellites' moment of inertia.* Icarus 226(2013), 2013.

Jo, J. H., Park, I. K., Choe, N., and Choi, M., *The Comparison of the Classical Keplerian Orbit Elements, NonSingular Orbital Elements (Equinoctial Elements), and the Cartesian State Variables in Lagrange Planetary Equations with J2 Perturbation: Part I.* Journal of Astronomy and Space Science (JASS), Vol. 28, Issue-1, 2011a. DOI: 10.5140/JASS.2011.28.1.037.

Jo, J. H., Park, I. K., Choe, N. M., and Choi, M. S., *The Comparison of the Classical Keplerian Orbit Elements, Non-Singular Orbital Elements (Equinoctial Elements), and the Cartesian State Variables in Lagrange Planetary Equations with J2 Perturbation: Part I.* Journal of Astronomy and Space Sciences, 28(1), 2011b.

Jouannic, B., Noomen, R., and van den IJssel, J. A. A., *The flyby anomaly: An investigation into potential causes.* 2015.

Konopliv, A. S., Park, R. S., Yuan, D., Asmar, S. W., Watkins, M. M., Williams, J. G., Fahnestock, E., Kruizinga, G., Paik, M., Strekalov, D., Harvey, N., Smith, D. E., and Zuber, M. T. *The JPL lunar gravity field to spherical harmonic degree 660 from the GRAIL Primary Mission.* Journal of Geophysical research: Planets, Vol. 118, 2013.

Larson, W. J. and Wertz, J. R., *Space mission analysis and design.* Microcosm, Inc., Torrance, CA (US), 1992. No. DOE/NE/32145–T1.

Lissauer, J. J. and de Pater, I., *Fundamental Planetary Science - Physics, Chemistry and Habitability.* Cambridge University Press, 1st edition, 2013. ISBN: 9780521618557.

Liu, X., Baoyin, H., and Ma, X. , *Periodic orbits around areostationary points in the Martian gravity field.* School of Aerospace, Tsinghua University, 100084 Beijing, China , 2012.

Michigan State University, *Error Propagation*, 2003. http://lectureonline.cl.msu.edu/~mmp/labs/error/e2.htm. Date of access: 27/04/2017.

Muller, D., *Galileo Full Mission Timeline*, 2006. http://www.dmuller.net/spaceflight/mission.php?mission=galileo. Date of access: 22/01/2017.

NASA, *jup230.bsp log file* , 2004. https://naif.jpl.nasa.gov/pub/naif/JUNO/kernels/spk/jup230.bsp.lbl. Date of access: 27/02/2017.

NASA, *Europa Jupiter System Mission*, 2009. http://solarsystem.nasa.gov/missions/ejsm. Date of access: 31/07/2016.

NASA, *Galileo Legacy Site*, 2010. http://solarsystem.nasa.gov/galileo/index.cfm. Date of access: 31/07/2016.

NASA, *jup310.bsp log file* , 2013. https://naif.jpl.nasa.gov/pub/naif/JUNO/kernels/spk/jup310.bsp.lbl. Date of access: 05/04/2017.

NASA, *Galileo Orbiter*, 2016a. http://nssdc.gsfc.nasa.gov/nmc/spacecraftDisplay.do?id=1989-084B. Date of access: 14/02/2017.

NASA, *Juno overview*, 2016b. http://www.nasa.gov/mission_pages/juno/overview/index.html. Date of access: 05/01/2016.

NASA, *Juno overview*, 2016c. https://www.nasa.gov/mission_pages/juno/main/index.html. Date of access: 05/01/2016.

NASA, *FY 2018 Budget Estimates*, 2017. https://www.nasa.gov/sites/default/files/atoms/files/fy_2018_budget_estimates.pdf. Date of access: 26/05/2017.

NASA, *Navigation and Ancillary Information Facility - An Overview of Reference Frames and Coordinate Systems in the SPICE Context*, 2017. https://naif.jpl.nasa.gov/pub/naif/toolkit_docs/Tutorials/pdf/individual_docs/17_frames_and_coordinate_systems.pdf. Date of access: 06/02/2017.

Noomen, R. , *AE4-878 Mission Geometry and Orbit Design, Lecture Notes.* Delft University of Technology, 2015.

Parisi, M., Finocchiaro, S., and Iess, L., *Multi-arc and batch-sequential filters for the orbit determination of ESA's JUICE mission.* 23rd International Symposium on Space Flight Dynamics, Pasadena, CA, 2012.

Russell, R. P. and Brinckerhoff, A. T., *Circulating Eccentric Orbits Around Planetary Moons.* Journal of Guidance, Control, and Dynamics 32(2), 2009. ISSN: 0731-5090.

Seidelmann, P. K., Archinal, B. A., A'hearn, M. F., Conrad, A., Consolmagno, G. J., Hestroffer, D., Hilton, J. L., Krasinsky, G. A., Neumann, G., Oberst, J., Stooke, P., Tedesco, E. F., Tholen, D. J., Thomas, P. C., and Williams, I. P. , *Report of the IAU/IAG Working Group on cartographic coordinates and rotational elements: 2006.* Celestial Mechanics and Dynamical Astronomy, 98(3), pp. 155-180, 2007.

Showman, A. P. and Malhotra, R., *The Galilean satellites.* Science, 286(5437), 1999.

Spencer, J. R., *Ganymede in the thermal infrared: preliminary analysis of Voyager IRIS data.* In Lunar and Planetary Science Conference, 14, 1983.

Stam, D. , *AE4890-11 Planetary Sciences I, Lecture Notes.* Delft University of Technology, 2016.

Szondy, D., *ESA selects instruments for JUICE mission to explore Jupiter and its moons*, 2013a. http://newatlas.com/juice-instruments/26377/. Date of access: 31/07/2016.

Szondy, D., *ESA selects instruments for JUICE mission to explore Jupiter and its moons*, 2013b. http://newatlas.com/juice-instruments/26377/pictures?thumb=true#picture9. Date of access: 31/06/2016.

University of Colorado Boulder, *Galileo spacecraft to Jupiter*, 2004. http://lasp.colorado.edu/home/galileo/. Date of access: 03/09/2016.

Vallado, D. A. and McClain, W. D. , Fundamentals of Astrodynamics and Applications, 3rd Ed., 2007. ISBN: 978-0-387-71831-6.

Wakker, K. F. , *Fundamentals of Astrodynamics.* Delft University of Technology, Delft, 2015. ISBN: 9789461864192.

Wertz, J. R. , *Spacecraft Attitude Determination and Control.* Springer, Dordrecht, 1st edition, 1978. ISBN: 978-90-277-1204-2.

White, F. M., Pressure Distribution in a Fluid, 2008. ISBN: 978-0-07-128645-9.

Wikipedia, *Exploration of Jupiter*, 2017a. https://en.wikipedia.org/wiki/Exploration_of_Jupiter. Date of access: 24/01/2017.

Wikipedia, *Associated Legendre polynomials*, 2017b. https://en.wikipedia.org/wiki/Associated_Legendre_polynomials. Date of access: 27/02/2017.

Xu, Z. , *Numerical Analysis, Lecture Notes.* University of Notre Dame, 2015. http://www3.nd.edu/~zxu2/acms40390F15/Lec-5.6.pdf. Date of access: 01/02/2017.

Zharkov, V. N. and Gudkova, T. V. , *Models, figures and gravitational moments of Jupiter's satellite Io: Effects of the second order approximation.* Planetary and Space Science 58(10), 2010. ISSN: 00320633.